

POLITECNICO DI TORINO

Collegio di Ingegneria Chimica e dei Materiali

**Master of Science Course
in Materials Engineering**

Master of Science Thesis

**Process parameters optimization of Ti6242 produced by
Electron Beam Melting**



Supervisors

Prof. Luca Iuliano
Prof. Abdollah Saboori
Prof. Manuela Galati

Candidate

Erika Lannunziata
266758

March 2021

*To my family
my heart, my sunshine*

Abstract

Titanium and its alloys are used in a wide range of applications such as aerospace, marine, biomedical implants and consumer goods, thanks to their superior specific strength, excellent corrosion resistance, and biocompatibility.

However, from manufacturing point of view, the titanium alloys suffer of several problems, mainly due to the reactivity to oxygen. The introduction of oxygen results in the simultaneous formation of an oxygen layer (α -case), it forms during casting, processing, and elevated temperature exposure in service. This oxide layer formed during service often limits the maximum service temperature of titanium alloys.

Thanks to the controlled environment, Additive manufacturing processes have already demonstrated the capacity to produce Titanium alloys with superior quality respect to the conventional manufacturing processes. In this contest, Electron Beam Melting (EBM) which works in a vacuum build environment and high build temperature is extremely attractive to minimize residual stress, oxide formation and material contamination. However, EBM research is mainly focus on Ti6Al4V, while alloys, such as Ti6242, that are wider applicability at higher temperature applications and excellent fatigue and creep resistance are rarely explored.

The presented work aimed to explore the process window of Ti6242 by EBM process. The focus was to understand the influence of process parameters (in particular beam speed, current, focus offset and line offset) on the final microstructure and the material density. The surface finishing measured as surface roughness and dimensional accuracy as function of process parameters has been analysed using descriptive and inferential statistical analyses in light of producing a representative industrial component.

Contents

1	Introduction	1
2	Literature Review	2
2.1	General overview of titanium alloys	2
2.2	Ti-6242	5
2.3	Additive Manufacturing technology	8
2.3.1	EBM	9
2.4	Ti-6242 for AM	13
2.4.1	Ti-6242 built by EBM	13
2.4.2	Ti-6242 built by SLM	14
2.5	Previous studies on roughness	16
3	Experimental set up	18
3.1	Powder characterization	20
3.2	Density	20
3.2.1	Archimede density	20
3.2.2	Optical microscope	22
3.3	Roughness	22
4	Roughness analysis	23
4.1	Statistic elements	25
4.2	Elimination fundamentals	25
4.3	Comparison with normal distribution	26
4.4	The null hypothesis	28
4.5	ANOVA	28
4.6	Linear regression	30
5	Parameters effects analysis	32
5.1	Beam speed influence	32
5.2	Diameter influence	39
5.3	Beam current influence	44
5.4	Focus offset influence	49
5.5	Line offset influence	55
5.6	Contour parameters	60

6 Results	63
6.1 Powder characterization	63
6.2 Density and porosity	65
6.3 Parameters effects	67
7 Conclusion	70
8 List of symbols, tables and figures	71
A Appendix	80
A.1 Density results	80
A.2 Top surface roughness	81

0.1 Riassunto

Introduzione Le leghe di titanio trovano ampio utilizzo nel campo aerospaziale, navale e biomedicale grazie alle proprietà quali l'elevata resistenza specifica, resistenza a corrosione e biocompatibilità.

Le leghe di titanio si differenziano per il quantitativo e la tipologia di elementi leganti. In particolare le leghe alfa sono caratterizzate dall'uso degli alfa stabilizzanti, che aumentano la temperatura di *beta-transus*, ovvero la temperatura alla quale si ha la trasformazione allotropica dalla forma α (esagonale compatta) alla forma β (cubica corpo centrato), e da un quantitativo di beta-stabilizzanti minore del 5%.

La lega Ti-6242 è una lega *near-alpha*, ovvero si trova al limite tra le leghe alfa e le leghe alfa-beta, utilizzata per componenti strutturali che lavorano ad elevata temperatura.

La composizione chimica nominale di questa lega, in percentuale peso wt% è 6.20 Al, 1.95 Sn, 3.80 Zr, 2 Mo, 0.08 Si, 0.021 C, 0.008 N, 0.06 O, 0.0016 H, mentre la restante parte è costituita da titanio. La temperatura di *beta-transus* è intorno ai 993°C.

L'alluminio e gli elementi interstiziali, quali O, N e C stabilizzano la fase α , ovvero tendono ad aumentare la temperatura di *beta-transus*, mentre il Mo è un beta-stabilizzante (tende a ridurre la temperatura di trasformazione). Infine gli elementi Zr e Sn hanno un lieve effetto sulla temperatura di trasformazione ma la loro presenza comporta un aumento di resistenza, grazie al meccanismo di rinforzo per soluzione solida.

Processi convenzionali e problematiche Il processo convenzionale più usato, in termini di tonnello, è quello termo-meccanico che prevede un primo step di colata in lingotto, seguito da varie operazioni di deformazione a caldo e trattamenti termici. Tali passaggi portano a possibili microstrutture quali la microstruttura lamellare, bimodale o equiassica, riportate in figura 2.8.

Il problema principale nell'applicazione di tale materiale risiede nell'elevata reattività con gli agenti contaminanti, in particolare con l'ossigeno, per cui è essenziale che la colata iniziale sia in vuoto, ciò aumenta i costi e riduce la flessibilità del processo. Tuttavia durante l'esposizione ad alta temperatura in aria il componente tende ad ossidarsi superficialmente formando un layer fragile, chiamato *α -case*, che ne riduce considerevolmente la vita in esercizio.

Inoltre, poiché a temperatura ambiente predomina la fase α , esagonale compatta, la bassa duttilità del materiale rende difficoltoso costruire manufatti di geometria complessa.

I vantaggi del Additive Manufacturing Per la produzione di componenti ad elevato valore aggiunto, l'Additive Manufacturing costituisce una valida alternativa ai processi convenzionali, che necessitano di controlli e accorgimenti di produzione dispendiosi. In particolare il processo di Electron Beam Melting (EBM) consente di produrre un componente, in vuoto ed ad alta temperatura di costruzione, riducendo al minimo i problemi legati alla contaminazione e alle tensioni residue.

Un fascio di elettroni, emessi riscaldando un filamento di tungsteno a temperatura maggiore di 2500°C, viene accelerato da una lente elettromagnetica mentre una seconda lente deflette il fascio nel punto in cui è richiesta la fusione, che avviene grazie alla conversione dell'energia cinetica degli elettroni in energia termica per le polveri.

La polvere interagendo con gli elettroni acquista carica negativa che può avere due effetti deleteri: la formazione di una nuvola di polvere, se la forza di repulsione elettrostatica tra polvere e

fascio supera la forza peso e la forza resistente che tiene insieme le polveri, mentre il secondo effetto è la diffusione del fascio di elettroni. Con opportune strategie di scansione e l'uso di polvere conduttiva è possibile evitare tali problematiche e produrre con successo componenti tramite EBM.

Um'altra tecnica largamente utilizzata per la costruzione di manufatti metallici è l'SLM, una tecnica in cui il laser fonde selettivamente il layer di polvere, le principali differenze tra i processi EBM e SLM sono riportate in figura 1.

	SLM	EBM
Source of energy	Laser >1kW	Electron beam >3.5kW
Beam size	0.3-0.5 mm	0.2-1 mm
Materials	Carbon steels, stainless steel, aluminum alloys, titanium and alloys, nickel-based alloys, cobalt-chromium alloys	Titanium and alloys, nickel-based alloys, cobalt-chromium alloys
Athmosphere	N, Ar	Vacuum
Sensivite to residual stresses	High	Low
Heat treatment required	Yes	No
Complexity of the sample	High	Medium
Particle size	10-45 micron	45-105 micron
Surface roughness	30-104 micron	50-100 micron
Dimensional accuracy	0.1 mm	0.5 mm
Layer thickness	30-50 micron	50-100 micron
Speed of the process	Lower than EBM	Very High

Figura 1: Principali differenze tra EBM e SLM

Risulta evidente che entrambi i processi abbiano vantaggi e svantaggi, ad esempio l'SLM permette un'accuratezza dimensionale maggiore e una migliore finitura superficiale rispetto all'EBM ma è un processo più lento ed è "a freddo", ovvero non prevede preriscaldamento, per cui i componenti sono soggetti a tensioni residue.

Studi progressi Nel campo di ricerca del EBM sono stati fatti numerosi studi volti all'ottimizzazione della produzione di prodotti in Ti6Al4V, mentre lo studio del processo per il Ti-6242 è solo agli esordi.

H.Fan e S.Yang sono stati i primi condurre uno studio per l'ottimizzazione di parametri per il Ti-6242 costruito con l'SLM, in particolare osservando gli effetti dei parametri di processo (riportati nella tabella in Fig.2.15) sulla microstruttura, durezza e resistenza a trazione dei provini tal quali (definiti *as-built*) e dopo trattamento di invecchiamento condotto a 595°C per 8 h. Riportando la rugosità superficiale rispetto alle diverse velocità di scanning utilizzate (Fig.2.16) emerge che per velocità troppo basse (850 mm/s) o troppo alte (1050 mm/s) si ottengono elevati

valori di R_a , che assume il valore minimo per un valore di velocità intermedio di 950 mm/s. Tale effetto è legato alla densità di energia che cresce al diminuire della velocità di scansione del laser, causando l'evaporazione e lo spatter del metallo fuso, che si traduce in un deterioramento della finitura superficiale; al contrario una bassa velocità di scansione si traduce in una fusione parziale della polvere che influenza la qualità della superficie (si ha solo una sinterizzazione della polvere, per cui le particelle che rimangono adese incrementano la rugosità superficiale).

I risultati dell'analisi di densità confermano tale trend, mettendo in evidenza come per basse velocità si ottenga una microstruttura caratterizzata da pori sferici, legati all'evaporazione del metallo, mentre per alte velocità si ottengono pori irregolari sintomo non solo di una parziale fusione ma anche di un'insufficiente sovrapposizione delle zone fuse consecutivamente. I risultati di tale ricerca consentono di concludere che la velocità ottimale di scansione del laser, che comporta la costruzione di provini con $R_a=9\mu\text{m}$ e densità di 99.5%, è di 950 mm/s.

Fujeda e Cui sono stati tra i primi ad impiegare la polvere di Ti-6242 nella tecnologia EBM, con l'aggiunta di boro per migliorare la resistenza in temperatura della lega. I risultati ottenuti in termini di densità hanno messo in evidenza come tale aggiunta consenta di ottenere massima densità (che supera il 100% poiché il fascio laser permette di chiudere le porosità presenti inizialmente nelle polveri), una riduzione della taglia dei grani ed una microstruttura per lo più equiassica con una fase dispersa di TiB aciculare.

Sono stati condotti numerosi studi per mettere in luce gli effetti dei parametri di processo EBM sulla rugosità. Il valore di R_a per componenti prodotti con EBM si aggira tra i 20 e i 50 μm , il valore ottimale richiesto cambia a seconda del campo di applicazione di tale componente.

Da studi pregressi emerge che i principali parametri che influenzano la rugosità sono:

- lo spessore del layer e la corrente del fascio: layer sottili ed elevate correnti incrementano la rugosità superficiale;
- il focus offset e velocità di scansione: bassi focus offset e velocità migliorano la qualità della superficie;
- la distanza tra componenti creati nello stesso letto di polvere: all'aumentare del numero, i componenti sono più vicini, questo comporta un maggiore accumulo di calore che promuove l'adesione di polvere sinterizzata che aumenta la rugosità superficiale;
- la strategia di contour: permette un maggiore controllo della finitura superficiale;
- la granulometria della polvere: una taglia media maggiore aumenta la rugosità superficiale media, ma polvere sottile sinterizzata rimane più facilmente adesa al componente riducendone la qualità superficiale;
- la line offset (che dipende a sua volta dall'energia di input e focus offset): la rugosità del top diminuisce al diminuire della line offset;
- il calore fornito in ingresso: influisce sulle superfici laterali delle parti costruite.

Il presente lavoro di tesi ha come obiettivo l'individuazione e l'ottimizzazione dei parametri di processo che hanno maggiore effetto sul profilo di rugosità e sulla densità dei componenti in lega di Ti-6242.

Materiale e metodi La polvere di Ti-6242 impiegata ha una granulometria nel range compreso tra i 45-106 μm , tale range è ottimale per produrre componenti *layer by layer* con uno spessore dello strato di 50 μm . Attraverso un'analisi al SEM (Phenomen X) è stato possibile caratterizzare le polveri, in particolare calcolando la composizione chimica, effettuando un'analisi in modalità BSD in sei punti diversi e facendo una media dei risultati ottenuti e studiando la morfologia delle polveri.

Sono stati prodotti 36 provini (20x20x20mm) con la macchina Arcam 2X, le cui specifiche sono riportate in tabella 3.3, ad alcuni provini è stata applicata la strategia di contour Multi-Beam™. I provini sono stati costruiti modificando diversi parametri di hatch (descritti nello specifico in Tab.1), come la velocità di scansione (S), il diametro e la corrente del fascio (BC), la line (LO) e focus offset (FO) e diversi parametri di contour (riportati in Tab.2) come lo spot time (ST) e il multispot overlap (MO). I parametri sono stati definiti attraverso dei livelli, in cui con il prefisso "L" si identifica il valore minimo, con "M" il medio e con "H" il valore più alto del parametro usato corrispondente. Per la corrente del fascio sono stati impiegati quattro diversi valori rappresentati attraverso i prefissi "L" "I" "H" "M", che identificano rispettivamente il livello *low*, *intermediate*, *high* e *maximum*. Soltanto 28 campioni (contrassegnati) su 36 inizialmente pianificati nel DOE sono stati prodotti. a causa di problemi rilevati durante il job con i campioni con corrente massima (MBC).

Tabella 1: Parametri di processo impiegati per la produzione di provini senza l'impiego della strategia di contour: Focus offset(FO), Beam Speed (S), Line Offset (LO), Beam Current (BC).

Sample		FO [mA]	Speed [mm/s] (S)	LO [mm]	Beam current [mA]
1 and 19	✓	MFO	MS	MLO	IBC
2	✓	MFO	MS	HLO	IBC
3	✓	MFO	MS	LLO	IBC
4	✓	LFO	MS	MLO	IBC
5	✓	HFO	MS	MLO	IBC
6	✓	MFO	MS	MLO	LBC
7 and 21	✓	MFO	MS	MLO	HBC
8 and 26	✓	MFO	HS	MLO	IBC
9	✓	MFO	LS	MLO	IBC
10 and 22	✓	LFO	MS	MLO	LBC
11 and 23	✓	HFO	MS	MLO	IBC
12	✓	MFO	MS	HLO	IBC
13 and 36	✓	HFO	HS	HLO	HBC
14 and 20	✓	HFO	LS	HLO	HBC
15 and 35		MFO	LS	HLO	MBC
16 and 33		MFO	HS	HLO	MBC
17 and 28		MFO	HS	LLO	MBC
18 and 34		MFO	HS	MLO	MBC

Tabella 2: *Principali parametri impiegati nella modalità contour, i parametri di hatch applicati per questi provini sono quelli utilizzati per la produzione del provino 1. Le sigle SP, ST, MO, MC e CFO corrispondono rispettivamente a Spots, Spot time, Multispot Overlap, Max Current e Contour Focus Offset (CFO).*

Sample	Spots	Spot time [ms]	Multispot overlap	Max current [mA]	FO [mA]	
24	✓	HSP	LST	LMO	LMC	CFO
25	✓	HSP	MST	LMO	LMC	CFO
27	✓	LSP	LST	HMO	HMC	CFO
29	✓	HSP	LST	MMO	LMC	CFO
30	✓	HSP	HST	LMO	LMC	CFO
31	✓	LSP	HST	HMO	HMC	CFO
32	✓	LSP	HST	MMO	HMC	CFO

I profili di rugosità superficiale sono stati misurati da un profilometro RTP-80 prodotto dall'azienda Metrology Systems, fornito dell'unità di azionamento TL90. È stata seguita la normativa ISO 4288, che prevede una lunghezza di cut-off pari a 2,5 mm, vengono prese 5 lunghezze di cut-off con una velocità di scansione di 1 mm/s e un'ampiezza massima rilevabile di 600 μm . Per ogni superficie sono state raccolte tre misure per ciascun campione, una sulla parte sinistra, una al centro e una sulla destra sia sul top che sulle facce laterali a partire dalla faccia numerata.

Infine è stata analizzata la densità di tutti i provini attraverso l'analisi di Archimede, che permette di calcolare la densità del campione rispetto al volume occupato, utilizzando una bilancia idrostatica con acqua distillata alla temperatura di 25°C. Il primo passo consiste nel pesare il campione in aria, e poi immergerlo in acqua per valutare l'effettivo volume del campione. Il peso del campione bagnato è superiore a quello secco, a causa della presenza di fluido all'interno dei pori superficiali. Tali porosità, dette porosità aperte, potrebbero essere legate alla presenza di crepe esterne o intrappolate dalla rugosità superficiale. Pertanto, la porosità aperta deve essere esclusa dal calcolo della densità.

Per calcolare la densità relativa geometrica, attraverso l'equazione 3.1, si assume la densità dell'acqua a 25°C pari a 997 kg/m^3 e la densità nominale del Ti-6242 uguale a 4540 kg/m^3 . Mentre la porosità è stata calcolata attraverso l'analisi di immagine di provini al microscopio ottico, precedentemente lucidati. Per verificare i risultati di porosità dell'analisi di Archimede e analizzare la distribuzione dei pori, il provino più promettente e il peggiore sono stati analizzati attraverso una macchina di tomografia computerizzata (GE Phoenix v—tome—x s). Per la scansione è stato impostato un voltaggio di 168 kV, una corrente di 110 μA ed un voxel size di 0.020 mm, mentre i risultati sono stati analizzati con il programma VGStudio Max 3.4.

Strumenti di statistica descrittiva e inferenziale Per analizzare quali parametri abbiano avuto effetto sul profilo di rugosità è stata effettuata un'analisi statistica ed inferenziale sui campioni che differivano per valore di parametro analizzato, a parità degli altri parametri di processo.

Nello specifico come primo step sono stati individuati i dati figli di errori accidentali, prima con l'analisi grafica del *boxplot* e poi come verifica è stato applicato il principio di esclusione di Chauvenet. I dati così individuati sono stati esclusi e sostituiti con il valore medio di R_a corrispondente.

Successivamente si è confrontata la distribuzione dei dati, ipotizzando che essa potesse essere assunta come normale (o Gaussiana). Come prima indicazione sono stati ricavati gli istogrammi su cui si può sovrapporre la distribuzione gaussiana, permettendo così di confrontare visivamente se la distribuzione sperimentale è simmetrica o asimmetrica, tale indicazione può mettere in luce l'effetto del processo sui dati di rugosità.

Per confutare l'ipotesi di distribuzione normale si può utilizzare il metodo rigoroso del χ^2 ed un metodo grafico, meno rigoroso ma di facile lettura, chiamato Grafico di Probabilità Normale (G.P.N).

Successivamente è definita un'ipotesi nulla che implica la presenza di errori sistematici nelle misure rilevate, quindi la possibile presenza di un effetto che influisca sulla rugosità superficiale. Tale ipotesi può essere confutata attraverso il test di ipotesi rispetto alla media o alla varianza delle colonne, ovvero se i valori sperimentali di valore medio e varianza non rientrano in un intervallo fiduciario, con una probabilità di errore prestabilita (α), allora c'è una probabilità $(1-\alpha)$ che ci sia un effetto del parametro analizzato sulle misure di rugosità.

Un'analisi più stringente è l'analisi della varianza per un fattore di controllo (ANOVA), per cui se il rapporto delle varianze dei valori di rugosità delle colonne è maggiore del valore calcolato secondo la distribuzione di Fisher, allora non si può negare che il parametro preso in esame (che cambia da colonna a colonna, in quanto ciascun campione riportato nella colonna differisce dall'altro per la variazione del parametro preso in esame) abbia un effetto sulla rugosità.

L'identificazione di tali effetti è possibile solo effettuando un'analisi globale dei dati sperimentali, dai quali si riesce a desumere, ad esempio, un'eventuale presenza di un fattore sistematico che porta alla deriva di tutti i dati. Tale analisi deve essere effettuata tramite lo strumento della regressione, nel quale si cerca un modello matematico che descriva al meglio i dati sperimentali. Studiando poi l'andamento dei residui se il modello descrive correttamente i dati sperimentali i residui tenderanno a disporsi con andamento casuale; mentre se fosse presente all'interno dei dati sperimentali un eventuale effetto dovuto a errori sistematici di misurazione, allora i residui tenderanno a disporsi con una certa regolarità. Dal segno dei residui è possibile rilevare la presenza di effetti sistematici (come la variazione di un parametro di processo) rappresentato dalla tendenza dei residui ad assumere valori o positivi o negativi, in assenza di tale effetto il segno dei residui è casuale.

Risultati e conclusioni L'analisi SEM in modalità BSD permette di avere informazioni sulla composizione chimica, difatti il numero di elettroni *back scatterati* dipende dal numero atomico del materiale analizzato, ed informazioni sulla morfologia. Per quanto riguarda quest'ultima, a diversi ingrandimenti riportati in Fig.2, è possibile osservare la presenza di aggregati sulle polveri che possono causare una riduzione della fluidità della polvere in macchina.

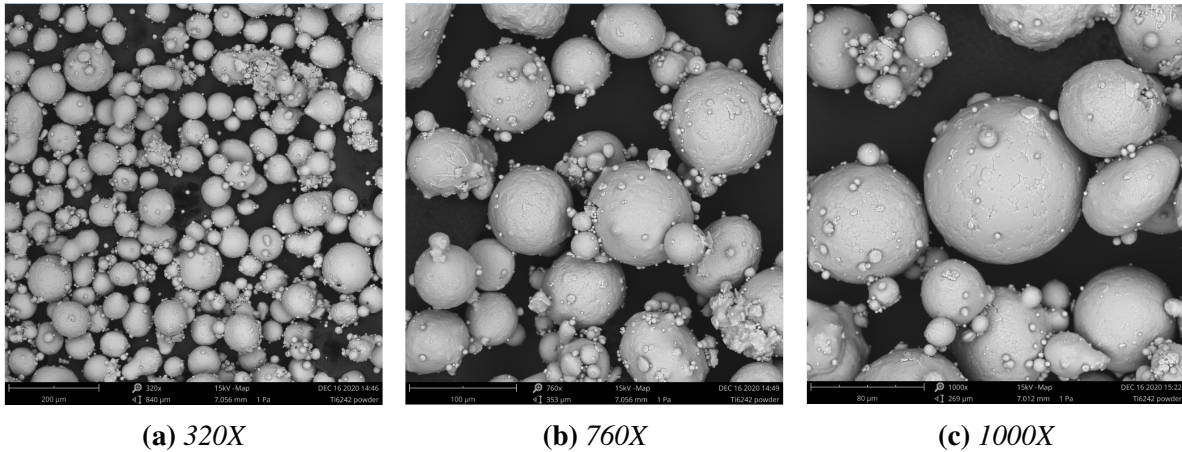


Figura 2: FOV: 838 (a) 353 (b), 269 (c) μm , Mode: 15kV - Map, Detector: BSD Full

Leggendo la tabella dei risultati in figura 3 non vi sono, in quantità rilevanti, atomi di elementi interstiziali.

Tabella 3: Average chemical composition of the Ti-6242 powder.

Element symbol	Atomic concentration [%]	Weight concentration [%]
Ti	85.12	85.53
Al	10.43	5.92
Zr	2.07	3.99
Sn	1.04	2.27
Mo	0.90	2.03
Si	0.44	0.26

Attraverso la modalità line scan è possibile rilevare la composizione lungo una linea desiderata; tale modalità è stata applicata (si faccia riferimento alla figura 3a) in una zona in cui è presente una porosità micrometrica e ciò ha permesso di scoprire che quest'ultima è legata ad una puntuale assenza di Ti, come mostra il grafico in Fig.3b.

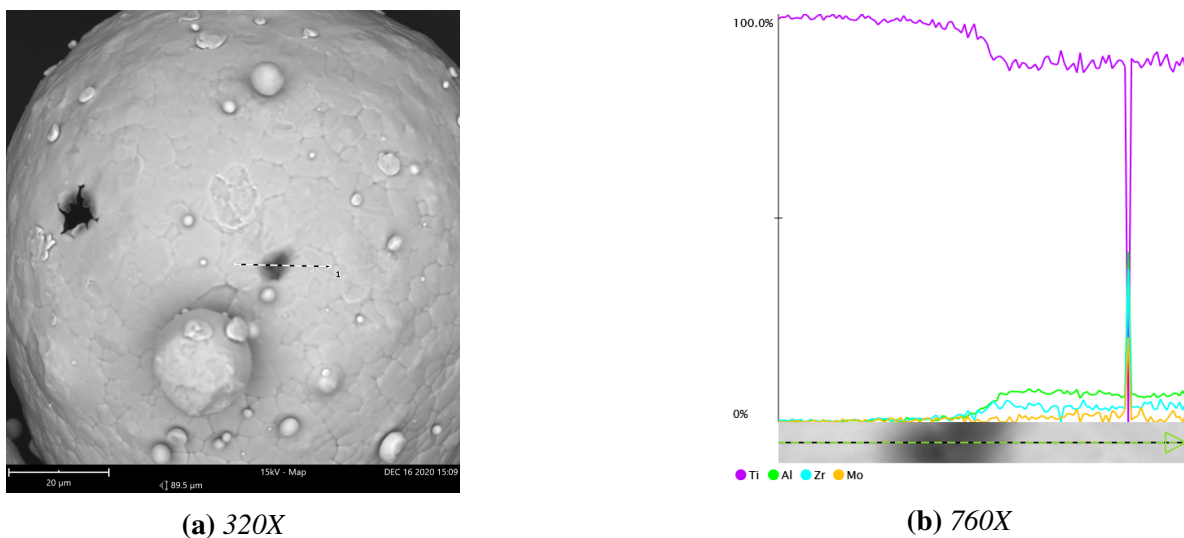


Figura 3: (a) FOV: 89.5 μm , Mode: 15kV - Map, Detector: BSD Full, (b) combined line scan

In tabella 4 sono riportati i risultati dell'analisi di Archimede in ordine crescente di densità relativa rilevata. Il valore minimo di densità rilevato è 93,7 % (per il campione 5) mentre il massimo registrato è 99,5 % (per il campione 10), che coincide con il valore massimo riscontrato per i campioni prodotti da SLM con i parametri ottimizzati ma risulta inferiore al valore raggiunto dai campioni prodotti in EBM con l'aggiunta di boro.

Dall'analisi di Archimede è inoltre possibile osservare che i campioni in cui è stata impiegata la modalità contour di scansione mostrano densità elevata, a parità di parametri di hatch (del campione 1), in quanto un maggiore controllo della superficie del campione più esterna consente la chiusura della porosità aperta.

I risultati dell'analisi di Archimede sono stati confermati da una scansione tomografica computerizzata dei campioni 5 e 10, in particolare dall'immagine 6.4 (a) si possono chiaramente osservare le cricche superficiali del campione 5 responsabili dell'elevato valore di porosità rilevato.

Pertanto, da una prima lettura dell'analisi dei dati i risultati, i parametri di hatch del campione 10 e i parametri di contorno del campione 27 sono ottimali per alta densità e, di conseguenza, bassa porosità. Tuttavia, confrontando la densità tra il campione 10 e la sua replica (rappresentata dal campione 22), si osserva una variazione di 0,9 %.

Il secondo campione, in ordine decrescente di densità relativa, è il ventiseiesimo, che è una replica del campione 8. Questi differiscono in termini di densità relativa del 0,3%, quindi possono effettivamente essere considerati delle repliche, in altre parole tali parametri consentono di produrre provini con caratteristiche ripetibili.

Tra i campioni con contour il provino con la densità maggiore è il trentunesimo, per cui si può concludere che per massimizzare la densità i parametri migliori sono quelli di hatch impiegati per la costruzione del campione 8 e del contorno del campione 31.

Tabella 4: Risultati dell'analisi di Archimede.

#	Open porosity (%)	Closed Porosity (%)	Relative Archimedes density (%)	Relative Geometrical density (%)
5	3,7	6,3	96,2	93,7
6	3,5	4,6	96,4	95,4
14	2,2	3,0	97,8	97,0
36	2,0	3,1	98,0	96,9
13	1,7	3,0	98,3	97,0
23	1,6	2,5	98,4	97,5
9	1,6	2,3	98,4	97,7
2	1,6	2,4	98,4	97,6
12	1,5	2,4	98,5	97,6
11	1,2	2,2	98,8	97,8
1	1,0	1,3	99,0	98,7
22	0,9	1,4	99,1	98,6
3	0,9	1,7	99,1	98,3
20	0,8	1,4	99,2	98,6
19	0,8	1,5	99,2	98,5
4	0,7	1,4	99,3	98,6
8	0,6	1,1	99,4	98,9
24	0,4	0,6	99,6	99,4
26	0,5	0,8	99,5	99,2
7	0,5	1,1	99,5	98,9
25	0,6	1,1	99,4	98,9
27	0,4	0,7	99,6	99,3
21	0,4	1,2	99,6	98,8
29	0,5	0,7	99,5	99,3
30	0,4	0,7	99,6	99,3
31	0,4	0,6	99,6	99,4
32	0,4	0,9	99,6	99,1
10	0,3	0,5	99,7	99,5

La tabella 6.3 riassume i risultati dell'analisi statistica descrittiva e inferenziale. A causa della dispersione dei dati la distribuzione non segue quella normale, quindi in futuro, per verificare che i parametri trovati siano ottimali per Ti-6242 sarà necessario produrre più repliche, cioè più campioni con lo stesso set di parametri. Un maggiore numero di dati rivelati consente una distribuzione normale e una migliore efficienza nell'utilizzo della regressione lineare. Il test di ipotesi più rigoroso è l'ANOVA, quindi i suoi risultati consentono di definire quali parametri possono avere un effetto sui valori di rugosità, dalla tabella 5 emerge che la velocità del raggio, il diametro del raggio, l'offset del fuoco e il tempo spot sembrano influire sulla rugosità. Per quanto concerne l'effetto del diametro, poiché non è possibile impostare direttamente questo parametro nella macchina EBM in quanto dipende dai parametri di focus offset e di corrente del fascio, non è possibile applicare il modello di regressione lineare non essendoci una relazione lineare tra il diametro al R_a . Inoltre non è stato possibile ottenere un modello che collegasse i parametri di velocità e spot time alla rugosità in modo efficace a causa dell'elevata

dispersione dei dati. Il coefficiente R^2 rappresenta l'efficienza del modello lineare nel rappresentare l'andamento dei dati rispetto ad un parametro di processo, per cui un valore di R^2 può essere un sintomo della presenza di più effetti simultanei di più parametri sulla rugosità oppure può essere legato ad un'alta dispersione dei dati. Ricerche future più approfondite saranno volte a chiarire il collegamento tra la velocità del fascio e lo spot time rispetto alla rugosità superficiale. Tuttavia l'unico parametro efficacemente descritto dal modello lineare è il focus offset, dove il coefficiente R^2 riscontrato risulta maggiore di 50% (i risultati del modello sono mostrati in figura 4).

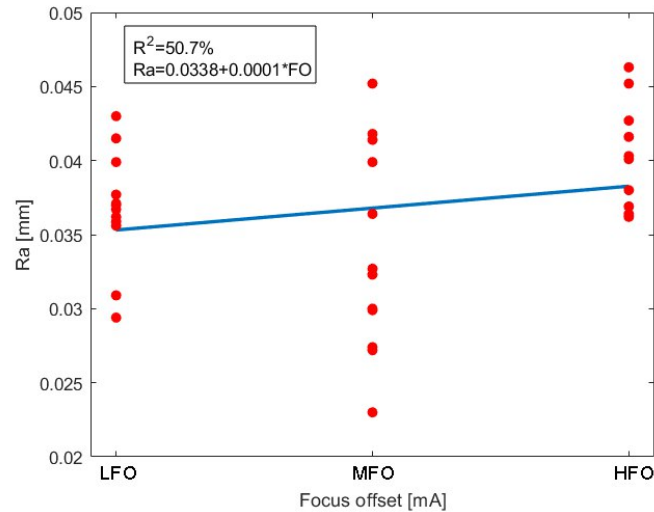


Figura 4: Modello lineare per il Focus Offset (FO)

Dall'equazione ricavata sembra che la rugosità diminuisca all'aumentare del valore di offset del fuoco, per confermare questa ipotesi è necessario produrre campioni con valori intermedi di FO per riscontrare se nuovi valori di rugosità seguono l'andamento risultante dal modello di regressione.

Tabella 5: Tabella riassuntiva dei risultati dell'analisi statistica descrittiva e inferenziale, condotta sui parametri di processo che possono avere un effetto sulla rugosità delle superfici laterali dei provini.

Parameter	Experimental χ^2	Test average hypothesis	Test variance hypothesis	ANOVA
Beam speed	Outside	Outside	Outside	$F_{calc} > F_U$
Beam diameter	Outside	Outside	Inside	$F_{calc} > F_U$
Beam current	Outside	Inside	Outside	$F_{calc} < F_U$
Focus offset	Inner	Outside	Inside	$F_{calc} > F_U$
Line offset	Outside	Inside	Outside	$F_{calc} < F_U$
Multispot overlap	Inside	Outside	Inside	$F_{calc} < F_U$
Spot time	Inside	Outside	Inside	$F_{calc} > F_U$

Lo scopo del grafico in figura 5 è identificare la finestra dei parametri ottimali per ottenere campioni ad alta densità, ad esempio maggiore di 97%, con la migliore finitura del piano.

Non è stato possibile effettuare un'analisi statistica sull'effetto dei parametri sulla rugosità superficiale del top, a causa del basso numero di dati rilevati e di repliche disponibili per ogni set di parametri. Per il set di parametri scelto, è possibile suddividere le superfici superiori in tre categorie, rappresentate sulla destra: superficie a pori singoli, con rigonfiamenti sui bordi e piana.

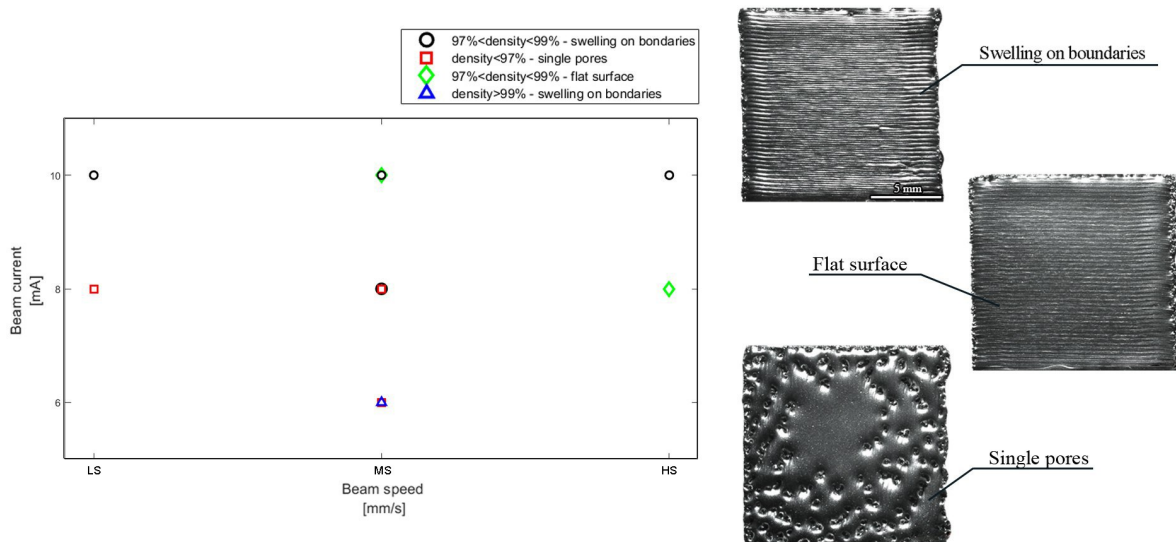


Figura 5: Divisione dei campioni in base ai parametri di FO e BS assunti, alla densità e all'aspetto della superficie del top.

Come si denota nel grafico sulla sinistra all'aumentare della velocità del fascio l'aspetto della superficie cambia, passando dalla tipologia "a pori singoli" (con densità inferiore a 97%) ad una superficie piatta (caratterizzata da una maggiore densità). Per testare i parametri scelti è stato prodotto un secondo job, in cui oltre i provini sono stati costruiti due componenti finali, in particolare delle giranti. L'analisi di Archimede eseguita sugli elementi del secondo job ha evidenziato come la finestra di parametri, individuata nel job precedente, sia ottimale per la produzione di componenti in Ti-6242, i quali hanno registrato una densità geometrica di 99,93%. L'analisi tomografica avvalorata tale risultato mostrando che non ci sono macroporosità interne, come evidenziato dalla figura 6 (a), in cui è riportata la sezione con la porosità più grande rilevata (denominata come *Defect 1*) che è minore di 1 mm; mentre la distribuzione delle porosità, rappresentata nell'istogramma in Fig.6 (b), mostra che la maggior parte dei pori ha dimensione minore di 0.3 mm. L'ultima immagine dimostra che l'accuratezza dimensionale rilevata è nell'ordine di ± 0.2 mm rispetto al CAD progettato.

In conclusione i parametri di processo trovati in questo lavoro, e riassunti in tabella 6, consentono la produzione di componenti in Ti-6242 densi. Ulteriori studi saranno volti ad ottimizzare i parametri a seconda del design del componente e del suo campo di applicazione.

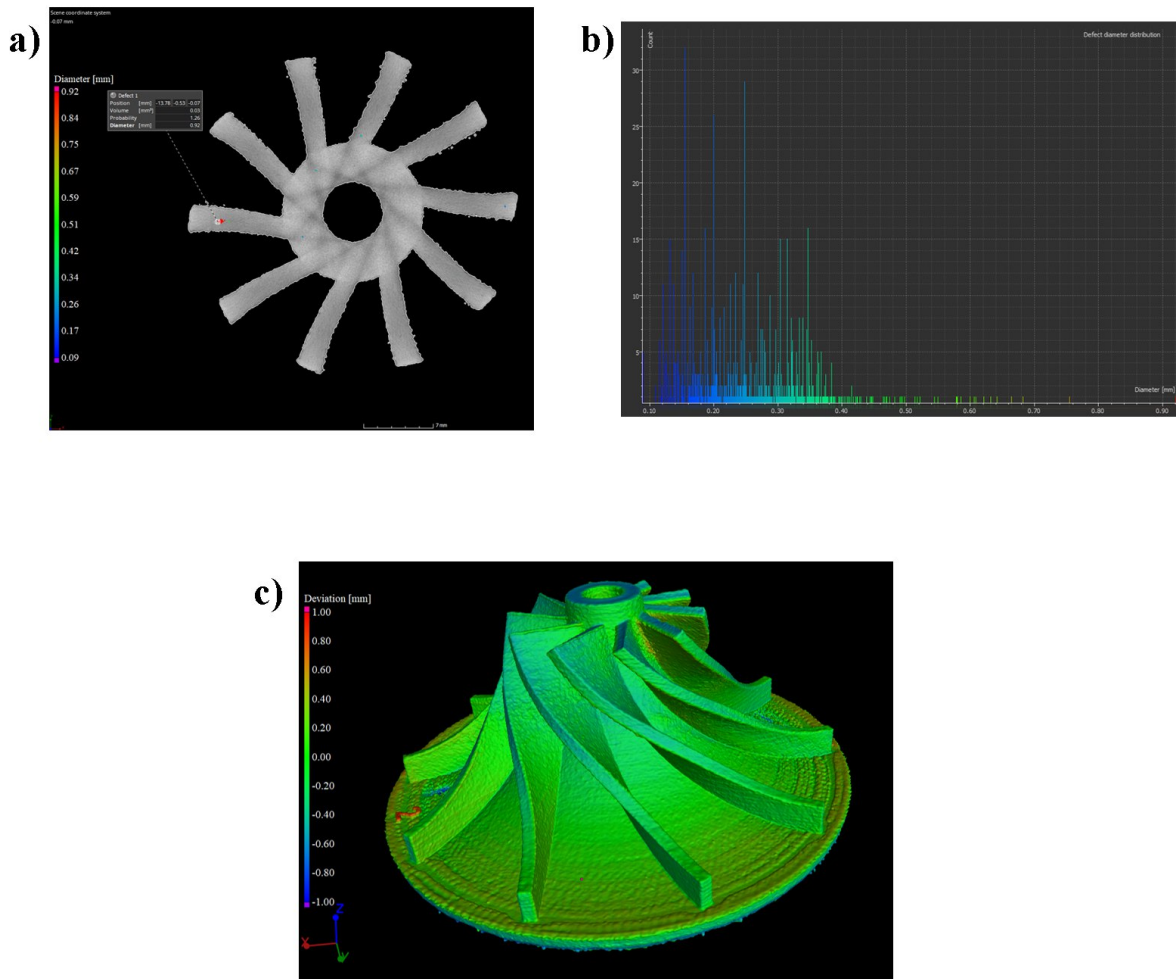


Figura 6: Analisi tomografica della girante, la scala cromatica contraddistingue il diametro delle porosità presenti. I colori caldi rappresentano un surplus di materiale, mentre i freddi un deficit.

Tabella 6: Parametri ottimizzati

	FO [mA]	Beam Speed [mm/s]	LO[mm]	Ref Current [mA]
Hatch	MFO	HS	MLO	IBC
Contour				
Spots	Spot time [ms]	Multispot overlap	Max current [mA]	FO [mA]
LSP	HST	HMO	HMC	CFO

Chapter 1

Introduction

Ti-6Al-2Sn-4Zr-2Mo (Ti-6242) is a near- α titanium alloy designed in the late 1960s for high-temperature service. Ti-6242 is of interest to the aerospace industry for providing superior mechanical performance to Ti-6Al-4V at elevated temperatures [1] i.e. up to 450°C, thanks to its excellent fatigue and creep resistance.

The Ti-6242 main problems with conventional processes are the reactivity to oxygen and the fair fabricability. The entry of oxygen results in the simultaneous formation of an oxygen layer (α -case), formed during casting, processing, as well as high temperature exposure in service. This oxide layer formed during service often limits the titanium alloys maximum service temperature. However, the additive manufacturing technology allows the Ti-6242 use for high value components.

The purpose of this work aims to understand the influence of process parameters, in particular beam speed, current, focus and line offset, multispot overlap and spot time on the final microstructure, density and surface roughness.

The first chapter summarizes literature reviews about titanium alloy, its classification into three classes, as for bonding elements, an introduction of α alloy, especially of Ti-6242, as well as an overview of the conventional and related process and main issues. Also, a window of the EBM process is explored with a focus on the comparison between SLM and EBM for Ti-6242. Finally, it reported an overview about parameters that have an effect on roughness for EBM's samples.

The second chapter describes the experimental set up adopted for the samples production and for the analysis of density, porosity and roughness.

The third chapter is focus on roughness, in particular on its parameters and the statistical tools used for the analysis of the experimental data.

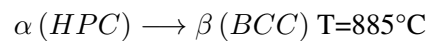
The subsequent chapter shows the statistical analysis results. The first step involves the identification of accidental errors and their exclusion followed by the comparison between experimental data distribution with the normal one. Statistical methods are carried out and observed in order to deny the null hypothesis and demonstrate the presence or absence of a systemic effect on the measured roughness measurements. The results chapter reports the outcomes of the experimental and statistical analysis in order to detect the effects of the process parameters on Ti-6242 samples.

Chapter 2

Literature Review

2.1 General overview of titanium alloys

The titanium is an allotropic metal, whom exists in due different crystalline phases 2.1:



this temperature is called "beta transus".

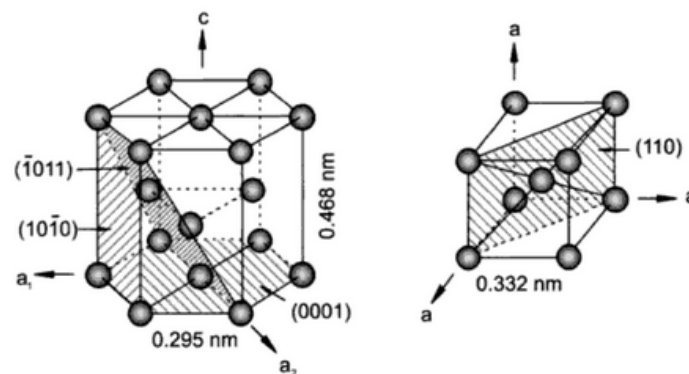


Figure 2.1: Crystal structure of hcp α and bcc β [2]

This transformation leads to a volume expansion because the atoms in the BCC crystal structure are not closely packed as HCP ones. It results in a decrease in density [3].

Pure titanium is characterized by high ductility but low strength, reason why it is enriched by alloying elements to increase strength. This leads to an alteration of alpha and beta phases stability, in particular beta transus temperature changes with the addition of alloying elements. Classification and effects are summarized in 2.4:

- *Alpha stabilizers* increase the temperature of β -transus.

Al has a very high solubility both in the α and β field, as indicated in Fig.2.2, it provides high performance in high temperature. The titanium-aluminum phase diagram is shown in fig2.3.

Depending on the aluminium content exists an intermediate, ordered phase called Ti_3Al (α_2) or ordered TiAl (γ) at higher aluminium content.

Additional alpha stabilizers are Ga, Ge, rare earths as solid-solution binding elements, while O,N,C, are interstitial alloying elements. Given small concentrations and properly controlled, interstitials improve strength.

- *Beta stabilizers* lower the temperature of β -transus. β -stabilizing elements can lead to the formation of eutectoid compounds (e.g in the case of Iron, Chromium, Silicon and Nickel), or be isomorphous with the β phase, in the case of Vanadium, Molybdenum and Niobium if they can form solid solution with Ti.
- *Inerts*, because they do not affect the temperature are Zr and Sn. Although not involved in the balance of the phases, these items increase the resistance of the alloys [4]-[3].

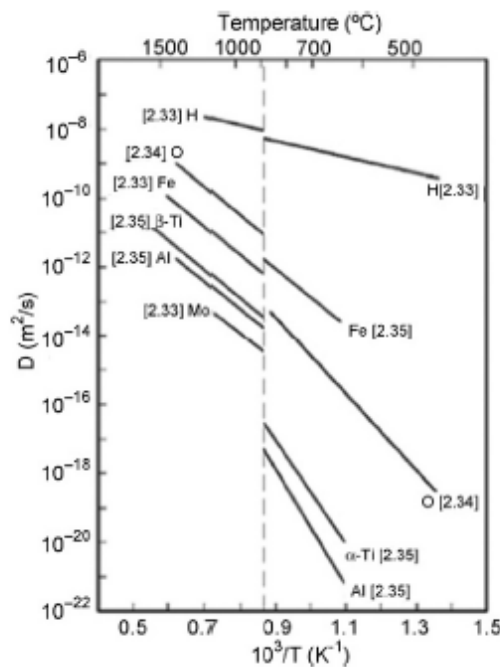


Figure 2.2: Diffusivity of elements in Ti. Note that some elements such as Mo and Sn, Zr and Nb (not shown here) are slow diffusers in Ti. [4]

Alloys can be classified into three groups depending on the amount of β phase content at room temperature [5]:

- *alpha alloys* if β phase percentage < 5%;
- *beta or near beta alloys* for β phase percentages higher than 20%;
- *alpha+beta or near alpha alloys* if β phase is between 10% and 20%;

Alpha alloy These alloys do not respond to heat treatments, because they consist predominantly of the α regardless of cooling rate from high temperature. It involves high weldability [3]. It is observed in figure 2.3 that α_2 transforms at 1342°C, it constitutes an interesting intermetallic compound for the improvement of the creep resistance of the alloy [4]. Moreover Ti-Al alloys are characterized by excellent high-temperature strength and by good fracture toughness and fatigue crack growth rate (slow), particularly at low temperatures [3]. A noteworthy feature of these alloys is that they do not change from ductile

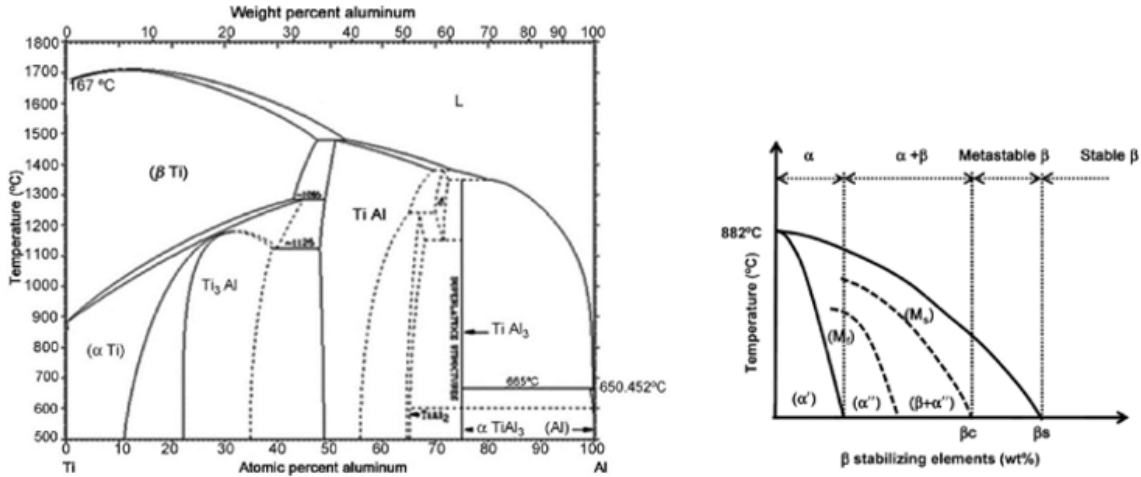


Figure 2.3: On the left there is the thermodynamic Ti-Al diagram, on the right a schematic graph to show the compositional difference between αI and αII . Note that αI forms when the β stabilizers are in low concentration. β_c in the figure stands for the critical concentration of β stabilizers to fully retain β phase at the condition of quenching. β_s stands for the concentration that is required to fully stabilize the β phase at room temperature. M_s and M_f mean the start and finish of the martensite phase transformation.[5]

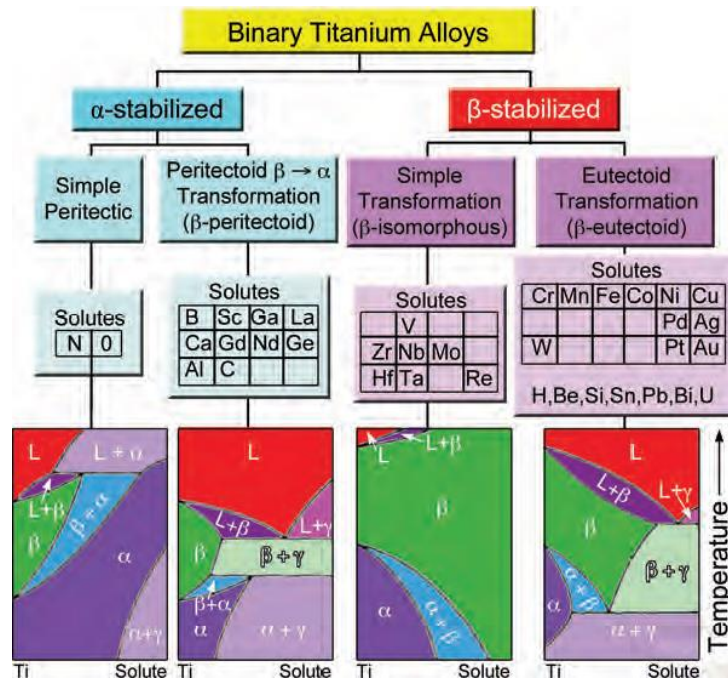


Figure 2.4: Classification of terminal titanium alloys.[3]

to brittle fracture at cryogenic temperatures (e.g. Ti-5Al-2.5Sn).[6] The main limitation is that they cannot improve mechanical properties by heat treatments and have difficult workability due to the high resistance to deformation. These characteristics compromise its wide use in structural applications.

Beta alloy This is the smallest alloy class and consists of alloys that contain nearly 100%beta phase after air cooling from an annealing temperature [3].These alloys heat treatable to achieve high strength levels but cannot undergo martensitic transformations [5].

β -alloys have excellent mechanical characteristics (the highest among titanium alloys), they are not characterized by a particular hardness but they stand out for their ductility and plastic deformability. They are also difficult to weld (they have to be in annealed condition). Therefore, they are used in applications requiring dimensional accuracy and good surface finish (e.g bolts, springs) rather than machining.

Alpha + beta alloy This class has a bi-modal microstructure, resulting in greater plastic deformability, as β is BCC, and high strength and toughness, as α . In order to create biphasic alloys of this type it is sufficient to add a few quantities of beta stabilizer as a binder. The weldability of an α - β alloy is satisfactory if the total beta-stabilizer content is low or the beta-stabilizing elements are weak (e.g Ti-6Al-4V is weldable) [3]. Biphasic alloys are obtained from this mixture of alpha and beta stabilizing elements, which have various uses, the main one being aeronautical due to their high cost. For example, in the aeronautical field, an alloy with 6%Al and 4%V is used, which has a mechanical strength of 1300 MPa. In this alloy the strengthening is achieved through the hardening by plastic deformation of the β phase (BCC) and by an appropriate heat treatment.

The table 2.5 summarize the most common applications of $\alpha + \beta$ alloys.

Ti Alloy composition	Applications	Condition
6% Al, 4%V	Rocket motor case; blades and disks for aircraft turbine and compressors; structural forgings and fasteners; pressure vessels; gas and chemical pumps; cryogenic parts; ordnance equipment; marine components; steam-turbine blades.	Annealing; Solution + aging
6% Al, 4%V (low O ₂)	High-pressure cryogenic vessels operating down to -320°F	Annealing
6% Al, 6%V, 2% Sn	Rocket motor cases; ordnance components; structural aircraft parts and landing gears; responds well to heat treatments; good hardenability	Annealing; Solution + aging
7% Al, 4%V	Airframes and jet engine parts for operation at up to 800°F; missile forgings; ordnance equipment.	Solution + aging
6% Al, 2% Sn, 4%Zr, 6% Mo	Component for advance jet engines.	Solution + aging
6% Al, 2% Sn, 2%Zr, 2% Mo, 2%Cr, 0,25% Si	Strength, fracture toughness in heavy sections; landing-gear wheels.	Solution + aging
10% V, 2% Fe, 3%Al	Heavy airframe structural components requiring toughness at high strengths.	Solution + aging
8% Mn	Aircraft sheet components, structural sections, and skins; good formability, moderate strength	Annealing
3% Al, 2,5 V	Aircraft hydraulic tubing, foil; combines strength, weldability, and formability.	Annealing

Figure 2.5: Titanium alloys application. [7]

2.2 Ti-6242

This work analyzes a particular titanium alloy, the Ti-6242. It can be classified as *near alpha* alloy used as the key structural component in the hot section of power generation and aircraft gas turbines as disks, impellers, and sheet metal components such as after burner cans and hot airframes with a service temperature of up to 540°C. These applications require an excellent combination of high strength-to-weight ratio and adequate corrosion/oxidation resistance at room and high temperatures. The nominal chemical composition of the Ti6242 alloy by weight percent (wt.%) is: 6.20Al, 1.95Sn, 3.80Zr, 2Mo, 0.08Si, 0.021C, 0.008N, 0.06O, 0.0016H, and balance Ti. The α to β transformation temperature or β -transus in Ti6242 is about 993°C[8]. Aluminium and interstitial elements (O, N, and C) are α stabilizer, i.e., they raise the β -transus while Mo is β stabilizer. In contrast, Zr and Sn have slight effect on β -transus but they strengthen the α phase by solid-solution strengthening mechanism. The oxidation and corrosion

resistance of the alloy in different oxidizing/corrosive environments is supplied primarily by Ti, through formation of a protective TiO_2 oxide film [8].

Microstructure

In order to describe titanium alloys structure it would be useful the previous history of the material, the alloy content, the working temperatures, method of fabrication, and heat treatment after fabrication.

There are four basic microstructures formed in the titanium alloy conventional process: widmanstätten, equiaxed, bimodal and martensitic structures [6]. If pure titanium (Fig.2.6) is cooled below the melting temperature the solid β phase nucleates in the form of dendrites and grows to form β grains. For temperature lower than beta transus, β transforms to α , at grain boundaries and grows in the form of individual lamellas (α_{lath}) within the prior grains β . During cooling α is characterized by close packed planes (slip planes) of HCP structure and close packed direction (slip direction) typical of BCC. If α_{lath} grow with the same orientation they form colonies of α (α_{colony}). The microstructure is called *Widmanstätten* if these colonies are distributed randomly within a prior β grains. Depending on the cooling rate finer α laths and smaller α colonies are obtained by rapid cooling, whereas slow cooling leads in thick α laths and coarse α colonies. This occurs also in Ti-6242, with the addition of formation of α phase along the prior β grain boundaries (called α_{gb}), whose thickness increases and becomes more continuous with lower cooling rates. Also, in these alloys β is retained along the interfaces of α_{colony} and at the interface of α_{gb} [6]-[3]. The figure shows 2.7 a Widmanstätten microstructure of Ti-64.

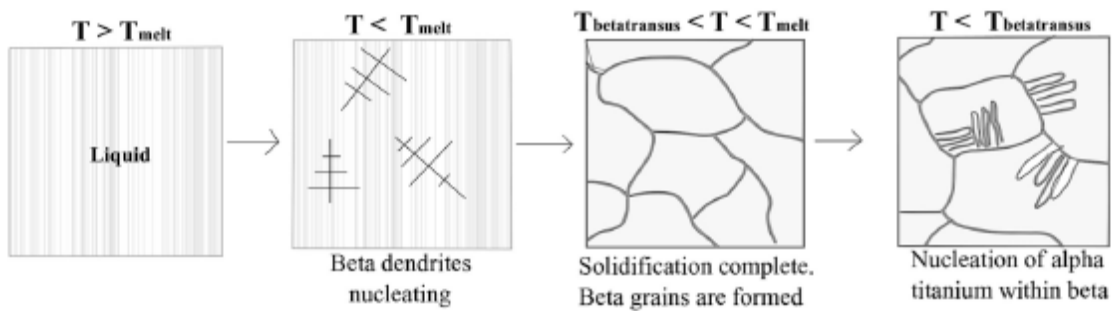


Figure 2.6: Microstructural evolution of pure titanium from $T_{melting}$ to below $T_{\beta\text{-transus}}$ [6].

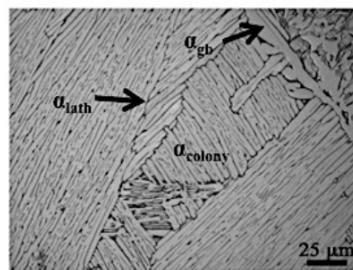


Figure 2.7: Widmanstätten microstructure of Ti-64 [6].

After a casting process the microstructure appears coarse due to the slower cooling rates, so it need to be modified by thermomechanical process.

Thermomechanical process (TMP)

From a tonnage perspective, ingot casting processing methods followed by various hot deformation and heat treatment operations, collectively referred to as thermomechanical processing (TMP), are the most common. In addition to producing a desired final shape in the form of a milling blank or a machined workpiece, the work introduced by deformation serves to accelerate the desirable changes in the microstructure either during the hot working itself (i.e., “dynamically”) or “statically” during subsequent heat treatment. Typical mill products made using these methods include billets, plates and sheets [9]. Typical thermo–mechanical processing steps for Ti–6242 alloy involve homogenisation (solution heat treatment), deformation, recrystallisation, ageing and stress relief annealing [6]. These processes lead to lamellar, bimodal and equiaxed microstructures.

- *Lamellar microstructure*, it is similar to that obtain from casting process (as in fig.2.7), but with a control of the prior beta grain size. It arises from an annealing treatment above $T_{\beta\text{-transus}}$ after plastic deformation in the $\alpha+\beta$ and β region.
- *Bimodal microstructure* (fig 2.8(a)) is obtained from extensive deformation in the $\alpha+\beta$ and after a solution heat treatment below $T_{\beta\text{-transus}}$. The globular primary α phase (α_p) is obtained from recrystallisation along prior β grains boundaries (of β and α_{gb}) and the β transformation consists of widmanstätten structure with a fine α_{lath} in α_{colony} with retained β at the interface.
- *Equiaxed microstructure* (fig 2.8(b)) is obtained by extensive mechanical working in the $\alpha+\beta$ phase region and subsequent solution heat treatment at temperatures in the two phase fields, in which α_{lath} is decomposed into equiaxed α .

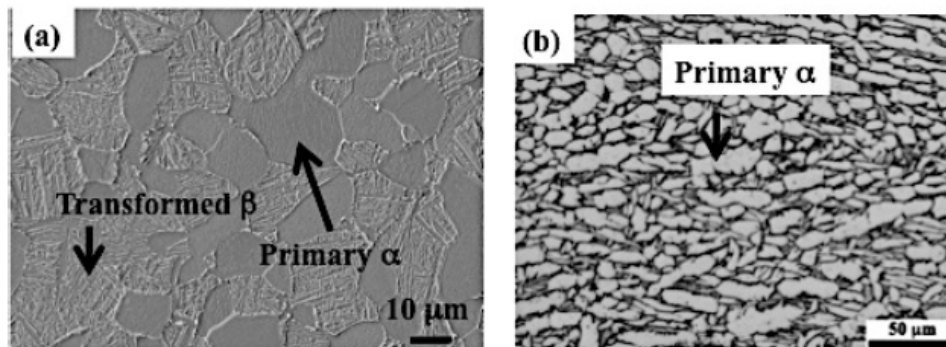


Figure 2.8: (a) Bimodal microstructure and (b) equiaxed microstructure of Ti-64 after TMP process [6].

For this purpose, the ingots are first synthesized via processes such as vacuum arc and cold hearth melting (electron beam or plasma). This step is crucial to maintain low residuals or interstitial elements in the liquid melt, as titanium can form with them hard, brittle and refractory titanium oxides, that decrease in mechanical properties to the final product.

The TMP of titanium alloys can lead to a variety of unwanted defects, such as cavities, regions of retained microstructures and anomalies in the grain structure, whose dimensions span a nanometer to multi-millimeter length scale and which can be deleterious to service properties, especially the initiation and growth of fatigue cracks [9].

Issues and challenge The main issues of this alloy with conventional process are the reactivity to oxygen and the fair fabricability. The high chemical affinity of titanium to oxygen (indicated by Ti-O bond energy of 2.12 eV, comparable to the Ti-Ti bond energy of 2.56 eV) and the high interstitial solid solubility of oxygen in α -titanium cause significant oxygen insertion during air exposure at high temperatures, resulting in the simultaneous formation of an oxide (TiO_2) scale on the surface and an oxygen-rich a layer underneath the scale.

This layer is commonly referred to as a α -case, as it is a continuous, hard, and brittle zone of oxygen-stabilized a phase. It forms during casting, processing, and elevated temperature exposure in service. This oxide layer is completely removed via machining or chemical milling whether formed during casting or processing. However if it is formed during service often limits the maximum service temperature of titanium alloys, since a significant amount of less ductile a case results in the formation of surface cracks under tensile loading [10].

Therefore for component with high value it is possible to produce Ti-6242 component for additive manufacturing technology.

For example, in the field of prostheses, $\alpha+\beta$ alloys are widely used, in particular Ti-64 and β -alloys for their greater formability. However, Ti-6242 compared to Ti-64 does not contain vanadium which is cytotoxic. This effect does not involve the accumulation of the substance but the direct interaction with the cells, indeed in a cell culture, total cell destruction is observed, after 7 days. Beta alloys also show a lower modulus than the others, closer to the modulus of human bones (classifiable as a composite material). it is therefore possible to replace the Ti-64 alloy with a near alpha alloy, building the prosthesis by AM technique and creating a porous or trabecular structure to reduce the elastic modulus.

2.3 Additive Manufacturing technology

Additive Manufacturing (AM) is a branch of production technology that allows the creation of very complex geometry components (undercut included) by using a single machine and without the use of tools. This process allows a reduction in time and costs compared to traditional technologies. Initially, the 3D Computer-Aided Design (CAD) model is created, allowing a wide freedom of design and therefore high customization. The additive machines work layer by layer, making the component section by section: this process can take place either by direct deposition of the material or with a process defined as "powder bed" (Powder Bed Fusion, PBF).

At the moment AM is an industrial system with limited work volumes and construction speeds, especially in metalworking field. It requires support structures for the development of the component in the machine, as well as the number of materials that can be processed is limited and the components obtained have a poor surface finish. On the other hand the AM ensure adequate performance in terms of dimensional tolerances, surface roughness and mechanical characteristics with minimal operator intervention. Therefore it is therefore efficient when the complexity of components justifies the high costs of the material and the process. The AM's main strength is the high geometric complexity with no increase in price, indeed process times and costs are directly linked to the size of the piece.

2.3.1 EBM

The EBM process The EBM process is a PBF additive technology, used to work metals. An electron beam is emitted by heating a filament of material, usually tungsten, to temperatures above 2500°C. The electrons are then directed and accelerated thanks to the presence of two electromagnetic lenses, as shown in figure 2.9: the first focuses the beam at the required diameter, the second deflects it to the point of merging with the platform. The beam current is controlled in the 1-50 mA range while the diameter can be concentrated up to a size of about 0.1 mm. Electron beam generation is typically much more efficient process than laser beam generation. When a voltage difference is applied to the heated filament in an electron beam system, most of the electrical energy is converted into the electron beam, and higher beam energies (above 1 kW) are available at a moderate cost.[11]

The EBM process takes place under high vacuum so as not to deflect the electron beam; the pressure of the residual gases is 10^{-3} Pa in the working chamber, 10^{-5} Pa in the electron gun. These conditions also make possible to process materials that would otherwise interact immediately with oxygen, (i.e by producing unwanted compounds), and this usually occurs when titanium alloys are used. In vacuum condition, it is also possible to recycle unused powders since they retain their chemical characteristics, preventing the material from oxidizing. However, it important to highlight that the morphology would change, due to the high temperatures reached. Therefore, the percentage of recycled unused powder out of the total must be kept low.

During the melting, inert gas, usually helium, is injected at a pressure of 10^{-1} Pa. On the other hand, the vacuum use causes a reduction in production capacity. For these reasons, the fields of application of greatest interest for EBM technology are biomedical and aerospace.

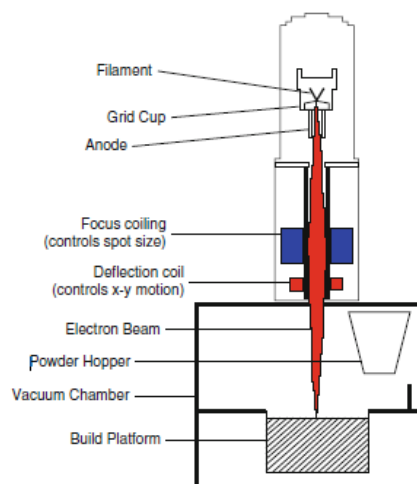


Figure 2.9: Schematic of an EBM apparatus. [11]

Electron beam-powder interaction The depth of penetration observed in the interaction between electron beam and powder is higher than one occurred in the laser beam. Electron beams, however, heat powder by transfer of kinetic energy from incoming electrons into powder particles. As powder particles absorb electrons they gain an increasingly negative charge. This has two potentially detrimental effects: if the repulsive force of neighboring negatively charged particles overcomes the gravitational and frictional forces holding them in place, there will be a rapid expulsion of powder particles from the powder

bed, creating a powder cloud. The second effect is related to the development of negative charges in the powder particles will tend to repel the incoming negatively charged electrons, thus creating a more diffuse beam. For this reason, the conductivity of the powder bed in EBM must be high enough that powder particles do not become highly negatively charged as well as and scan strategies must be used to avoid build-up of regions of negatively charged particles. In practice, electron beam energy is more diffuse; as a result, the effective melt pool size increases, creating a larger heat-affected zone. Consequently, the minimum feature size, resolution and surface finish of an EBM process is typically larger than an SLM process.

Features and path of powder The powders used for EBM are obtained by gas-atomization, so they are characterized by: spherical morphology, high flowability (about 25s/50 g), good packing density and particle size within a limited range below of $100\mu\text{m}$.

Another useful parameter is the minimum ignition energy value of the particles, i.e. the ease of ignition of the powders by an electric and electrostatic discharge. It is advisable to know this aspect in order to be able to handle the material with total safety. For an EBM system it is recommended to use particles with dimensions within the range of $45\text{-}105\mu\text{m}$ with a minimum ignition energy of $\geq 0.5\text{ J}$ [12]. As mentioned above, in EBM the powder bed must be conductive to ensure optimal interaction between beam and particles. The powders are loaded into the machine inside the hoppers placed on the sides of the bundle. The powder particles falls from the containers (arranged at the top); once deposited, a system spreads the powder homogeneously on the building platform (work platform). The thickness of the powder layer is optimized according to the nature of the material. The powder particles are scattered and compacted only by the raking system; as a result the thickness of the layer turns out to be 2-3 times bigger than it should be. Once the powder bed is preheated in a line-by-line sequence, the electron beam will begin to melt the material. When the powder is melted, the layer reaches the correct thickness. Once the fusion of the layer is completed, the platform is lowered by a distance equivalent to the thickness of the layer (0.05-0.2 mm). A new layer can be ready to be deposited and merged. Once the entire job is completed, the chamber is cooled by a flow of helium.

The EBM process is a process called "hot" as the powders are kept at a high and constant temperature for the entire duration of the fusion differently from the laser process called "cold", due to the fact that the metal powders are melted at a temperature close to ambient. EBM is characterized by the presence of a preheating that allows a partial sintering of the powder layer (for this reason low-melting alloys cannot be used); preheating is obtained by defocusing the beam: low power and high scanning speed. Preheating has a positive impact on the final component: whilst the compaction of the powders allows a reduction of supports, whose removal can lead to complications, the thermal gradient between the molten pool and solidified layers is reduced. A lower thermal gradient helps to reduce residual stresses so heat treatments at the end of the process cannot be necessary. The slow solidification of the material, unlike the cold SLM process, allows the grains to grow more, obtaining a coarser microstructure that enjoys greater elongation at break. Some disadvantages of pre-sintering are the difficult elimination of unfused powders and inability to create complex intern channels.[11]

The table in the figure 2.10 shows a comparison between EBM and SLM processes. EBM allows higher productivity (given the higher speed of the process and the possibility of depositing a thicker layer), with a higher energy efficiency while taking into account having to compromise with roughness and dimensional accuracy.

	SLM	EBM
Source of energy	Laser >1kW	Electron beam >3.5kW
Beam size	0.3-0.5 mm	0.2-1 mm
Materials	Carbon steels, stainless steel, aluminum alloys, titanium and alloys, nickel-based alloys, cobalt-chromium alloys	Titanium and alloys, nickel-based alloys, cobalt-chromium alloys
Athmosphere	N, Ar	Vacuum
Sensivite to residual stresses	High	Low
Heat treatment required	Yes	No
Complexity of the sample	High	Medium
Particle size	10-45 micron	45-105 micron
Surface roughness	30-104 micron	50-100 micron
Dimensional accuracy	0.1 mm	0.5 mm
Layer thickness	30-50 micron	50-100 micron
Speed of the process	Lower than EBM	Very High

Figure 2.10: Differences between EBM and SLM.[13]

The main factors that influence the quality of job are summarized as follows:

- **beam acceleration voltage;**
- **intensity of the beam current;**
- **focus offset**, i.e the additional current that is used by the electromagnetic lens to focus the beam.
- **line offset**, i.e space between hatch lines.

It was found, studying the effect of heat input and line offset in the EBM process for a Ti64 alloy [14], that a coarser microstructure is generated for high heat input and low line offset. By increasing the heat input or decreasing the phase shift of the line, a greater thickness of the alpha strip is obtained (phase which gives resistance to the alloy) with consequent lower hardness.

- **thickness of the layer;**
- **scan speed**, which can be set up by a function. The speed function index (SF) is a parameter used to dynamically control the movement of the beam during the process and consequently also monitor the amplitude of the melt pool.

During a job, the EBM machine can work in manual or automatic mode, and automatic mode is the only option offered to Level 1 users. When a part is built in automatic mode, the beam current is changed as a function of the geometry component, based on a thermal model in the machine control software and the beam speed is controlled by the speed function variable. While the beam current data are stored in the build log files, beam speed is not recorded. As beam current is

altered, the speed function changes beam travel rate to maintain the melt pool geometry constant throughout the process. [15]

- **scan strategy**, it includes scan process, scan mode and scan method.

The scanning process involves the different phases that take place in the machine:

- *phase of stabilization or preheating (preheating)*: it is used a defocused beam, or rather, low current and high speed. This phase allows to minimize the thermal gradient by minimizing residual stresses, the partial sintered powders support the protruding parts and reduce the diffusion effect;
- *melting phase*: melting of the powder with a high intensity current and low scanning speed;
- *latching phase*: scanning of the layer with high current and speed in order to improve dimensional accuracy and make the temperature of the layer more uniform.

The scanning methods that can be adopted during the EBM process affect the anisotropy of the component and can determine the main defects of unmelted powders on the layer. Therefore it is important to analyze the geometry of the component in order to apply the most proper mode. The scanning strategy are schematized in figure 2.11.

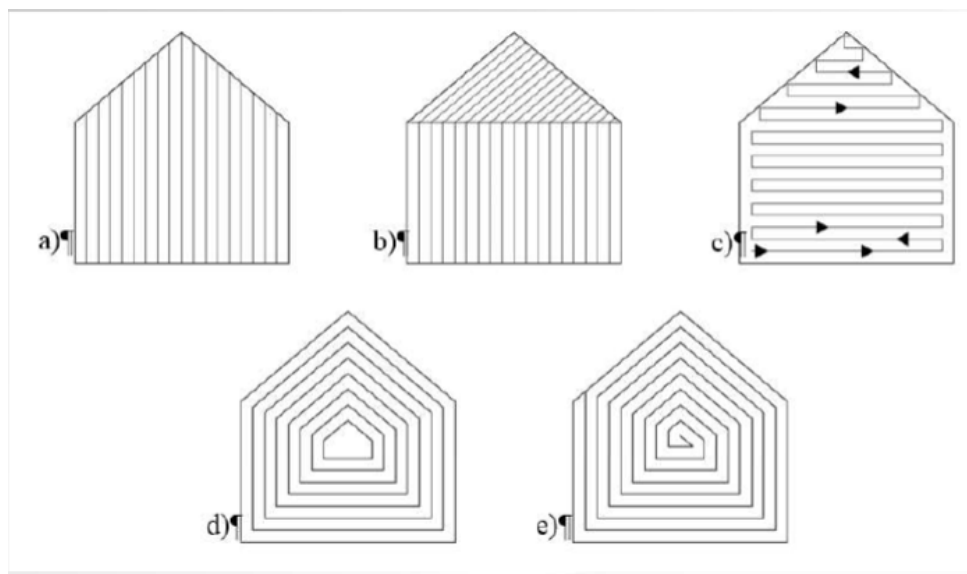


Figure 2.11: Scanning strategy in EBM process: unidirectional raster (a), multi-directional raster (b), zigzag (with offset of the contour (d) and spiral scanning (e)).

Scanning methods define how the beam moves across the layer should it move between fused and unfused zones. The modes used are schematized in figure 2.12.

There are several independent parameters that affect thermal transients (beam heating and rapid cooling), which are around $\sim 5 \times 10^6$ K/m, 10^3 - 10^5 K/s [16] that occur during the process. The first one is controlled by optimizing the primary beam parameters (e.g beam current, beam speed, speed function, focus offset, energy density, beam scan strategy), whereas the second one is influenced by the build geometry (e.g size, shape, thickness and contact area), build temperature, thermal mass of the build and orientation of the build.

In the EBM, the space-time variations in energy density affect the thermal gradient (G) and solidification

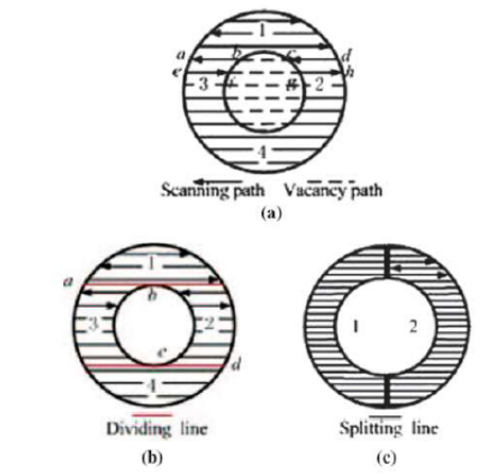


Figure 2.12: *Jump mode (a), sub-division mode (b), split mode (c).*

cooling rate (R) of the melt pool, which subsequently results in the typical column structure commonly found in AM builds. However, the full range of microstructure variations, which can be achieved by varying thermal transients by controlling process parameters, is still not fully understood. A previous study [17] revealed that, using different EBM scanning strategies, the G and R value can be tuned to the desired values, thus opening a space for process parameters to design site-specific microstructures for a given geometry.

2.4 Ti-6242 for AM

2.4.1 Ti-6242 built by EBM

Electron Beam Melting (EBM) is attractive thanks to its advantageous operating conditions, e.g., elevated build temperature and a vacuum build environment, which minimize residual stress and contamination, respectively. In addition, high beam power transfer of power into the part affords high deposition rates and facilitates building of components from materials with high melting points, as Ti-alloys.

Fujeda et al. [18] [19] were among the first to deal with the use of the Ti-6242 in EBM technology, in spite of the literature claims an extensive study of the effects of the process parameters on the Ti-6Al-4V microstructure. In these two articles boron is added to improve high temperature resistance by uniformly dispersing fine reinforcement particles to a heat-resistant Ti based matrix (like Ti-6Al-2Sn-4Zr-2Mo-0.1Si). Titanium-boron (TiB) is the most promising reinforcement particle with high strength and stability and has a similar expansion coefficient to Ti. The process parameters reported by these two articles are shown in the following table 2.13.

The relative density of the EBM specimens was more than 99 regardless of the preheating temperature. The relative density of the specimen fabricated at preheat temperature of 1203 K as compared to the apparent density of the raw powders was 100.4. It seems that the pores in the raw powders disappeared during EBM process and the relative density exceeded 100%. The boron addition led to a reduction of the grain size, furthermore grain morphologies were almost equiaxed, the acicular phase shown in the figure 2.14 consists of TiB.

Average diameter of spherical raw powders	70 μm
Machine	Arcam A2X
Energy density	2.4 J/mm ²
Scanning Speed	a range of 1000-2000 mm/s.
Preheating temperature	830 °C under vacuum, in which the TiB phase and $\alpha + \beta$ phase will coexist in the phase equilibrium diagram of this alloy system.
Layer thickness	100 μm
Spot size	200–300 μm

Figure 2.13: Table of EBM parameters.

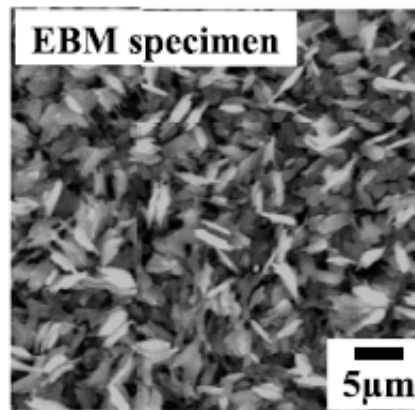


Figure 2.14: SEM image of EBM specimen.[18]

2.4.2 Ti-6242 built by SLM

Selective laser melting (SLM) is an additive manufacturing process in which a laser beam selectively melts consecutive layers of powder in order to fabricate intricate or functional parts from predefined three-dimensional (3D) models.

H.Fan et al. [1] reported a study about Ti-6242 built by SLM, for the first time, especially density, microstructure, hardness and tensile strength are investigated on as-built and on after aged (595°C/8 h) sample. The main process parameters are summarized in the following table 2.15.

Particle size distribution	10–45 μm
Machine	Concept Laser SLM machine (MLab) equipped with a maximum 100 W fibre laser
Power	Fixed at 95 W
Scanning speed	a range of 600–1200 mm/s
Scanning strategy	90° bidirectional
Hatching space	77 μm
Layer thickness	33 μm

Figure 2.15: Table of SLM parameters [1].

The Ti-6242 optimal processing parameter of Ti-6242 was determined by assessing the surface roughness and relative density of the as-built cubes.

The below Fig.2.16 illustrates the evolution of arithmetic mean roughness (Ra) with an increase in laser speed. The relatively low Ra values ($\sim 9\mu\text{m}$) were achieved at a speed window of 850–1050 mm/s, in which the 950 mm/s yielded the lowest Ra deviation of $\pm 0.15\mu\text{m}$. Otherwise, both low and high speeds out of the window lead to surface deterioration. The energy density increases as the decrease of laser speed, thus causing material evaporation and liquid spatters that degrades the surface quality. On the contrary, insufficient input energy and higher speeds lead to partial melting of powders, which can adversely influence the surface quality.

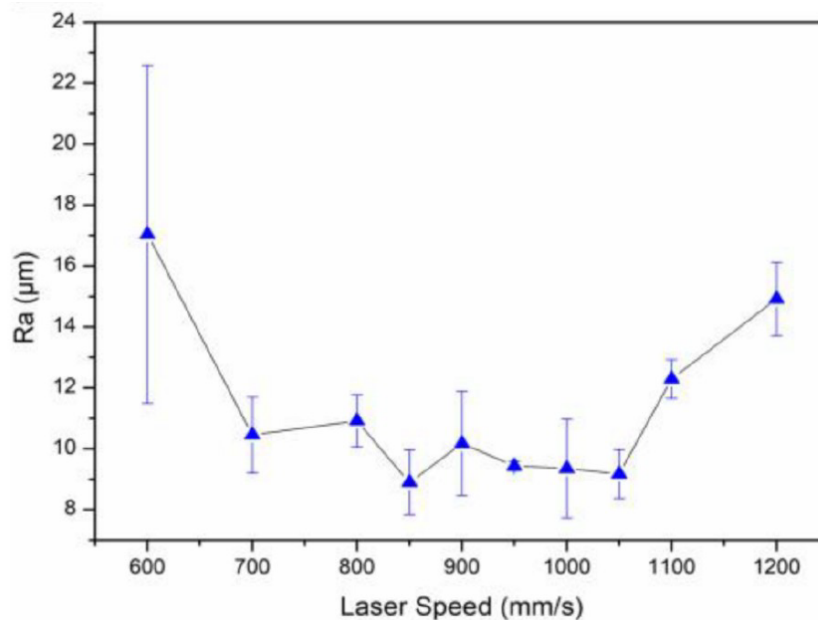


Figure 2.16: Profile showing the evolution of surface roughness with scanning speeds [1].

Relative densities with corresponding optical micrographs were plotted as a function of laser speeds in Fig. 3. All as-built samples are crack-free but show different porosity depending on the used laser speeds: indeed, lower speed introduced relatively large and spherical pores, which are keyholes as a result of trapped metallic vapor; high speed introduced irregular-shape pores, indicating not only a lack of particle fusion but also an insufficient overlap between neighboring tracks. The relative density increases

from 98% (600 mm/s-low speed) to 99.5% (950 mm/s) and then declines sharply to 95 (1200 mm/s-over-high speed). This study assesses that 950 mm/s is optimal to achieve an acceptable quality of SLMed Ti-6242.

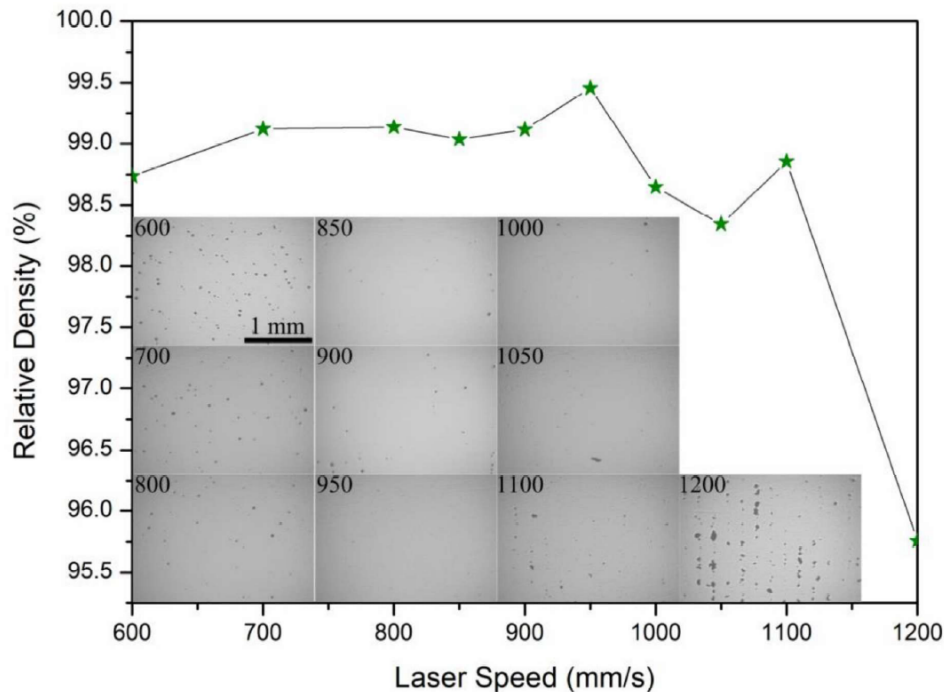


Figure 2.17: Polished cross-section micrographs of SLMed-Ti-6242 at various scanning speeds of 600–1200 mm/s [1].

2.5 Previous studies on roughness

Ra values for EBM components usually range between 20 and 50 μm . This value lead to using EBM technology for the mass production of patient-customized orthopedic structures with properties of high biocompatibility and osseointegration. However, this values are not adequate for other applications, such as aeronautical ones because sintered and unmelted powder on the surface of the part could promote the crack initiation with a detrimental effect of fatigue life of the component [20]. Several researchers have been conducted on the parameters effects on specimen product by EBM in Ti-6Al4V and the results are describes in the next paragraph based on the article written by Galati et al. [20].

Safdar et al. found that thicker parts and higher beam current values cause rougher surfaces, whereas lower focus offsets and slower scan speeds improve the surface quality. Jamshidinia et al. indicated that the surface roughness also depends on the distance between massive parts. Closer parts create heat accumulation zones which promote the adhesion of powder particles to the surface and increase roughness. Neira Arce et al. reported that the use of particles with a bigger average size increases the average surface roughness. However, owing to the sintering effect, finer powder particles stick more easily to the surface and reduce its quality. The adoption of contour strategies allowed a better control of the surface roughness. Klingvall Ek et al. showed that the offset between two adjacent contours and the scan speed strongly influence the surface roughness. Wang et al. found contours melted with MultiBeam™ strategy

are less rough but less accurate than the ones melted with continuous strategy. In general, as-built surface texture and its morphology differ between horizontal and vertical surfaces. Horizontal surfaces show melted ridges due to the scanning lines, while vertical surfaces are characterized by the presence of satellite sintered particles. Typical values for the roughness of vertical surfaces go from 24 μm to 30 μm , while horizontal upskin (upward) surfaces present show values of about 6 μm . The variability of the surface roughness is mainly attributed to the particles attached to the component surfaces. The downskin (downward) surfaces are rougher than a corresponding upskin surface even though they may require support structures to improve heat transfer from the bulk material and to avoid surface distortion and adhesion of the unmelted particles.

In addition Prisco et al.[14] found that the roughness of the top surface decreases by increasing the heat input rate and the focus offset or, alternatively, by decreasing the line offset. While the roughness of the side surface depends only on the heat input and increases with the increase of this parameter.

Chapter 3

Experimental set up

This chapter describes the experimental methods used to analyze the density, roughness and microstructure of the samples product by EBM.

During the process the melting step, after the preheating one, the beam melts firstly the contour of the parts using a discontinuous pattern called MultiBeam strategy, and then the inner part using a hatching strategy with parallel lines [20].

The following table summarizes the main process parameters of each specimen, where the reference current defines the current with which the reference length is melted. That means that the beam current is adapted to the scan length to be melted. Then the speed function algorithm calculates the corresponding beam speed. This involves variable process parameters over the area to be melted. This control allows for a better control of the temperature distribution and the melt quality.

In the first table 3.1 there are the samples that do not undergo contour. In the second one (Tab3.2) all specimens have the same hatch parameters like the sample 1, only external parameters change.

The DOE included:

- three levels for the focus offset identified as low levels (LFO), medium level (MFO) high level (HFO);
- three levels for the scan speed (S) identified as low level (LS), medium level (MS) and high level (HS);
- three levels for the line offset (LO) identified as low level (LLO), medium level (MLO) and high level (HLO);
- four levels for the beam current (BC) identified as low level (LBC), intermediate level (IBC) and high level (HBC) and maximum beam current (MBC).

As said for hatch parameters the spot time (ST) and multispot overlap (MO) can be divided into three levels where the prefix L identifies the "Low level", M the "medium level" and H the "High level".

The parameters Spots (SP) and Max current (MC) are identified by two levels with the prefix L for the lower level and H for highest one, while for contour mode only one value of Focus offset, called Contour Focus Offset (CFO), is used.

The total number of the samples is 36 (20x20x20mm) but the construction of the samples with MBC

failed and therefore will not be included in the analysis (they are not marked with a tick).

Table 3.1: Main process parameters for samples without contour: Focus offset(FO), beam speed, speed function index (SF), line offset, beam current.

Sample		FO [mA]	Speed [mm/s]	LO [mm]	Beam current [mA]
1 and 19	✓	MFO	MS	MLO	IBC
2	✓	MFO	MS	HLO	IBC
3	✓	MFO	MS	LLO	IBC
4	✓	LFO	MS	MLO	IBC
5	✓	HFO	MS	MLO	IBC
6	✓	MFO	MS	MLO	LBC
7 and 21	✓	MFO	MS	MLO	HBC
8 and 26	✓	MFO	HS	MLO	IBC
9	✓	MFO	LS	MLO	IBC
10 and 22	✓	LFO	MS	MLO	LBC
11 and 23	✓	HFO	MS	MLO	IBC
12	✓	MFO	MS	HLO	IBC
13 and 36	✓	HFO	HS	HLO	HBC
14 and 20	✓	HFO	LS	HLO	HBC
15 and 35		MFO	LS	HLO	MBC
16 and 33		MFO	HS	HLO	MBC
17 and 28		MFO	HS	LLO	MBC
18 and 34		MFO	HS	MLO	MBC

Table 3.2: Main process parameters for samples with contour

Sample	Spots	Spot time [ms]	Multispot overlap	Max current [mA]	Focus Offset [mA]
24	✓	HSP	LST	LMC	CFO
25	✓	HSP	MST	LMC	CFO
27	✓	LSP	LST	HMC	CFO
29	✓	HSP	LST	LMC	CFO
30	✓	HSP	HST	LMC	CFO
31	✓	LSP	HST	HMC	CFO
32	✓	LSP	HST	HMC	CFO

EBM machine

The machine used in this thesis activity is Arcam A2X, it is suitable for over 40 materials, its build chamber is specifically designed to withstand extremely high process temperatures over 1100° C, so it opens the door to manufacture material with high melt temperature and crack prone as Titanium Aluminide.

The technical data are reported in the follow table ¹.

¹https://www.ge.com/additive/sites/default/files/2020-01/EBM_A2X_DS_EN_US_1_v1.pdf

Table 3.3: *Technical data Arcam EBM A2X.*

Max build size	200 x 200 x 380 mm (W x D x H)
Max beam power	3kW
Cathode type	Tungsten filament
Min beam diameter	250 μm
Max EB traslation speed	8000 m/s
Active cooling	No
Minimum chamber pressure	5×10^{-4} mbar
Typical build atmosphere	2×10^{-3} mbar (partial pressure of He)
He consumption, build process	1 L/h
He consumption, ventilation	50-75 L/build cycle
Power supply	3 x 400 V, 32 A, 7 Kw
Size approx.	1850 x 900 x 2200 (W x D x H)
Typical process temperature range	600-1100 $^{\circ}\text{C}$
Weight	1700 kg
CAD interface	Standard:STL
Materials	Arcam EBM: Ti6Al4V Grade 5, Grade 23, Nickel alloy 718, TiAl

3.1 Powder characterization

The production of high-quality parts by EBM requires the use of a powder with a particle size between 45 and 106 μm . In EBM process, the theoretical thickness of the applied powder layer is 50 μm . Heating consolidates the material as the grains are progressively linked. After the melting step, the material is solid with virtually no porosity. Reduction in porosity results in reduced layer thickness of the melted zones, i.e., volume shrinkage and an increase of the overall layer thickness up to 80 μm . This means that a powder with particle size of 45-106 μm is suitable for applying a layer with a theoretical thickness of 50 μm [22].

In order to characterized the powder the SEM (Phenom X) analysis is carried out with a focus on chemical composition and the powder morphology.

3.2 Density

3.2.1 Archimede density

The density of samples was measured by means of a hydrostatic balance using distilled water at 25 $^{\circ}\text{C}$. The first step was to weight the sample in air, then it was immersed in the water to evaluate the actual volume of the sample. It includes the enclosed porosities into the specimen. The weight of the wet sample is higher than the dry one, due to the superficial pores that bring the fluid inside the sample from the external surface. The superficial porosities, called open porosities, could be linked to the presence of external cracks or trapped by surface roughness. Therefore, the open porosity has to be excluded from the density calculation.

The following procedure has been adopted [19]:

1. Weighing of the cube (dry weight). One measure is taken without beker, where the water was subsequently poured, and two measures for the dry sample with beaker (dry weight with beaker).

2. Positioning of the sample on the hydrostatic suspension, by the building platform, immersion in distilled water at 25°C and reading of the weight (weight in water).
3. The sample is removed from the water and then it is dried externally and weighed again (wet weight).
4. Previous steps 2 and 3 are repeated three times to get measurement replicas.

For the sake of simplicity, in the following table 3.4 contains the average values, for each class of weight.

Table 3.4: Average weight from Archimede density analysis.

#	Dry weight [g]	Average Dry weight with beaker[g]	Average weight in water [g]	Wet weight [g]
1	41.99	41.99	32.68	42.02
2	41.13	41.13	31.95	41.20
3	41.55	41.56	32.36	41.64
4	41.22	41.22	32.10	41.28
5	40.13	40.13	30.97	40.37
6	40.38	40.40	31.20	40.50
7	42.82	42.82	33.37	42.88
8	40.41	40.41	31.48	40.45
9	41.69	41.69	32.38	41.74
10	42.39	42.38	33.05	42.40
11	42.74	42.74	33.24	42.84
12	41.26	41.26	32.06	41.34
13	42.88	42.88	33.30	43.01
14	43.04	43.04	33.38	43.12
19	42.75	42.75	33.29	42.81
20	43.18	43.17	33.61	43.23
21	42.72	42.72	33.30	42.80
22	42.66	42.66	33.20	42.70
23	43.14	43.15	33.51	43.23
24	40.37	40.37	31.47	40.39
25	40.37	40.37	31.45	40.41
26	40.31	40.31	31.41	40.34
27	40.24	40.24	31.37	40.27
29	40.44	40.44	31.51	40.45
30	40.56	40.56	31.61	40.59
31	40.46	40.46	31.54	40.48
32	40.45	40.45	31.53	40.50
36	42.17	42.17	32.72	42.28

The relative geometrical density (or bulk density) is calculated as 3.1

$$\text{Bulk density} = \frac{\text{water density} - \text{dry weight}}{\text{wet weight} - \text{wet in water}} \quad (3.1)$$

where the water density at 25°C is 997 kg/m³. The relative density is the ratio between the bulk density and the nominal density of Ti-6242, equal to 4540 kg/m³.

The porosity and distribution of pores of specimens was analyzed by a computed tomography machine (CT-scan) (GE Phoenix v—tome—x s). The scans were performed using a voltage of 168 kV, a current of 110 μ A with a voxel size of 0.020 mm. The projection images and the porosity analyses are performed using VGStudio Max 3.4.

3.2.2 Optical microscope

Image analysis is a non-destructive technique that allows the analysis of the porosity of metal samples. The specimens were polished and observed under an optical microscope, images were captured and reported on the ImageJ software.

In particular, for each specimen were acquired 12 pictures, drawing three imaginary lines, an upper one, a central one and a lower one, four images were acquired on each of them. The images were reported in 8-bit format, in order to obtain the selected gray-scale figure. An appropriate command selected the black pixels to calculate the porosity as a percentage of black pixels on the total pixels of the investigated area. The results are collected in a table in the results section.

3.3 Roughness

The surface roughness profiles were measured by a RTP-80 profilometer by the Metrology Systems, provided with TL90 drive unit. The ISO 4288 regulation was followed, it involves a length of cut-off $\lambda=2.5$ mm, 5 number of cut-off, a speed of 1 mm/s and a maximum amplitude of 600 μ m. For each surface sample three measure were collected, one profile on the left, one on the center and one on the right, on the top and on the lateral faces starting from the numbered face.

Chapter 4

Roughness analysis

The present chapter aims at characterizing the surface profile. The most relevant parameters and analytic tools are introduced, the latter are described by the use of book "*Misurare per decidere*" [23]

The solid surfaces are not perfectly smooth: the shape, size and distribution of the roughness features are due to manufacturing or wear. The surface finishing may be characterized by two parameters: roughness and waviness, the former one occurs in any industrial process, whereas the latter one derives from processes such as chip removal with insufficiently rigid tools that can create make jumps during the advancement. This effect can result in a bad joint with another surface. As a result, the real shape is different from the nominal shape of CAD model, as shown in fig 4.1.

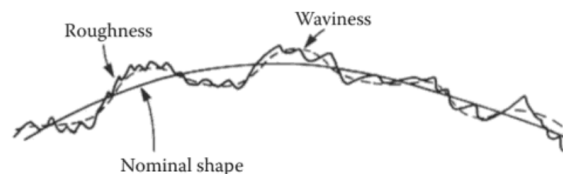


Figure 4.1: *Difference between real and nominal shape [24]*

Sectioning a surface with an orthogonal plane creates a profile made of peaks and valleys: the height and the distance between two consecutive peaks, as well as the depth of the valleys, have the same order of magnitude around a few tens of micron. Conversely the waviness has a size in the order of magnitude of millimeters. The profile can be mathematically described as $z=f(x)$ (fig.4.2).

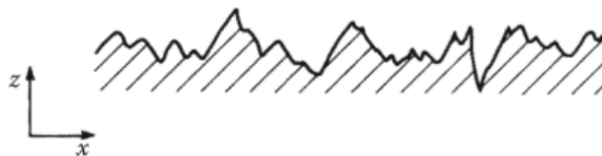


Figure 4.2: *Typical profile graph [24]*

In order to analyse the surface profile, the sampling length must be identified by the sampling length (or cut-off length). It is defined as the test length by which the roughness measurement can be considered as representative of the entire surface. It is common practice to choose a cut-off length of 0.8 mm (metti una reference).

The parameters can be divided into three classes: amplitude (based on height), spacing and hybrid parameters. The amplitude parameters measure the vertical surface deviations from the mean line, which is the zero level of the measurement. This line is drawn following the least squares method, it is identified as the mean line through a profile such that the sum of the squares of the profile deviations from that line are minimized. The local height of the surface profile is the distance of a point of the profile from its average reference line. It is considered positive (peak) above the average line and negative (valley) below it. While the space parameters measure the horizontal characteristics of the surface deviations, the hybrid parameters are a combination of the step and amplitude parameters. In the below section, the amplitude parameters relevant for this master's thesis work, in particular R_a , R_q , R_z , R_{sm} and R_{max} will be defined.

If $z=f(x)$ is the profile measured from the reference mean line and L is the length of the profile being assessed, R_a is defined by

$$R_a = \frac{1}{L} \int_0^L |z| dx \quad (4.1)$$

R_q is a deviation to RMS (Mean Square Root) defined as

$$R_q = \sqrt{\frac{1}{L} \int_0^L z^2 dx}. \quad (4.2)$$

These parameters are shown in fig 4.3.

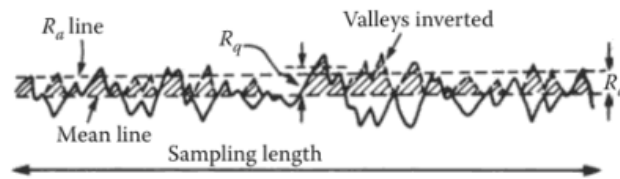


Figure 4.3: Average parameters R_a and R_q [24]

R_z is the average of the height difference between the five highest peaks and the five lowest valleys, reported in fig 4.4. The reason for taking an average value of peaks is to minimize the effect of unrepresentative peaks or valleys which casually occur and can give an erroneous value if singly considered [24].

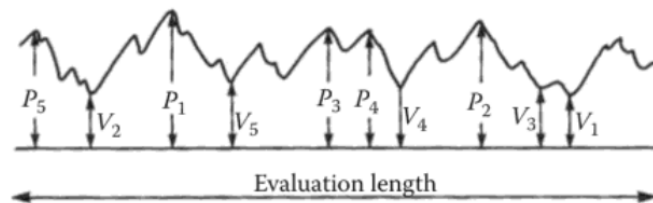


Figure 4.4: Peak parameters R_z [24].

The last parameters are R_{max} or the maximum difference between peaks and valleys, while R_{sm} is the average width of the grooves, which describes the average value of the elements width.

The roughness values for components produced by EBM fall within the R_a ranging from 20 to 50 μm .

4.1 Statistic elements

The first step for data manipulation consists in representing them by graphic diagrams (histograms). The x-axis is divided into a number of classes n_c , if n is the total data number.

$$n_c = \sqrt{n} \quad (4.3)$$

Each class should contain 4 or 5 members at least. The number of data included in a class is defined by the absolute frequency f_{a_j} of the j-th class. The probability that a measurement falls into the j-th class is estimated by the relative frequency $f_{r_j} = f_{a_j}/n$.

In histogram columns, their bases represent the class amplitude, while their areas the relative frequency. The latter one involves that the height is the density frequency ρ_f , obtained from the ratio between relative frequency and the amplitude of the class.

It is common to overlap the histogram diagram with the normal distribution (or Gaussian distribution) that represents the ideal data trend. This curve shows a peak corresponding to the mean value, while the variance is the width of distribution curve: it is the distance from mean value of roughness. The real distribution of experimental measurements is significantly different from the ideal one.

Eliminating the data related to systematic errors, i.e. excluding both too high and too low roughness values, is crucial.

4.2 Elimination fundamentals

It is possible use a graphic presentation called "boxplot" (as shown in fig.4.5), the lower base of the box corresponds to the first quartile (25th percentile) while the upper one to the third quartile (75th percentile). From the bases, two lines cross the minimum and maximum, calculated as follow

$$\text{Minimum} = \text{min value of the class} - 1.5 * IQR \quad (4.4)$$

$$\text{Maximum} = \text{max value of the class} + 1.5 * IQR \quad (4.5)$$

The median falls between the value of the first and third quartile. The distance from the two bases (the height of the box) is *IQR*, *interquartile range*.

The measurements that fall out are "outliers". The elimination of outliers values defined is restricted. As a result, IQR may be replaced as follow in the equation 4.4 and 4.5

$$1.5 * IQR * [1 + 0.1 * \log(n/10)] \quad (4.6)$$

The outliers can be divided into two categories: possible or suspected outside values, if they fall within the 3*IQR zone below the first or above the third quartile, or highly suspect outliers, if they fall out of this limit.

In addition the Chauvenet's criterion is another way to identify outliers, this method works by creating an acceptable band of data around the mean, specifying any values that fall outside that band should be

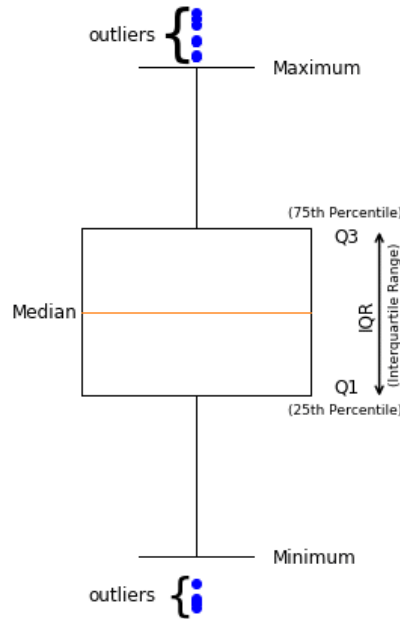


Figure 4.5: Vertical box

eliminated. In the Chauvenet criterion the probability of having an error in the measurement is related to the number of tests done (n). Indeed, the higher the number of tests, the greater probability of having values that differ from the expected average value. Therefore for each test it is fixed the 50% of probability to the event of having a measurement that differs from the mean value.

The principle is based on defining that in a single test a measurement value lower than the lower limit (x_{li}) or higher than the upper limit (x_{ls}) is given by

$$P(x < x_{li}) = P(x_{ls}) = \frac{50\%}{2n} \quad (4.7)$$

In conclusion, the cumulative probability for upper limit is calculated, from which the standardized values z_{ls} and z_{li} are obtained; those allow to define the limit values x_{ls} and x_{li} beyond which measurements are discarded.

Once the values to be excluded are identified, they can be removed from the data table and replaced with the average values of each class.

4.3 Comparison with normal distribution

If the results of the roughness tests differ negligibly from the mean value, the experimental distribution is consistently compliant with the trend of the normal distribution. If otherwise, the inconsistency may be imputed to systematic measurement errors, modifying a parameter results in a systemic effect on surface roughness. Rigorous mathematical methods are necessary to assess whether the experimental distribution deviates from the normal one.

There are two different methods to check that: " χ^2 method" and "Normal Probability Plot" (NPP). The first one is a rigorous numerical method, that allows to reject the hypothesis of normality distribution at a well-defined level of confidence. The second, graphical method does not allow for the rejection of the hypothesis of the normal distribution of data with the same rigor as the method of χ^2 . However, since is

consists in a graphical method, it provides information on causes of non-normality

The discrepancy between the experimental and normal distribution can be assessed based on the differences that emerged from the various classes into which the interval of the examined variable x was divided.

To make the comparison, the random variable is defined

$$\chi^2 = \sum_{j=1}^N \frac{(f_{a_j} - f_{a_t})^2}{f_{a_t}} \quad (4.8)$$

constructed by comparing the absolute experimental f_{a_j} and theoretical f_{a_t} frequency.

As previously stated in section 3.1 the absolute frequency is the number of data in a class, whereas the theoretical absolute frequency f_t is calculated with the product of the probability that in the normal distribution a datum falls within a well-defined data class for the total number of data.

At this point it is possible to calculate the experimental χ^2 and the obtained value must be compared with the theoretical limits, derived from the theoretical distribution of χ^2 for the required level of confidence.

In order to calculate the ideal χ^2 , it is also necessary to take into account the number of degrees of freedom, given by $n_c - n_v$, where n_v is the number of constraints used. With regard to the comparison between the normal distribution and experimental one, there are three constraints: equality of the mean value of R_a , equality of the standard deviation and equality of the total area, unitary for both.

The experimental value of χ^2 can fall within or outside the confidence limits identified for the established level of confidence. In case it fell within the limits of confidence, the test would not provide any information. Thus, there would be no reason to reject the false hypothesis that the experimental distribution of data is comparable to a normal one. If the experimental χ^2 fell out of the identified limits, the false hypothesis should be rejected, i.e. the experimental data are not arranged according to a normal distribution. In other words, the variation of a parameter, under the same process conditions, has an effect on the surface roughness.

The graphical method NPP consists in identifying a graphic presentation that allows to recognize immediately if the experimental data can be arranged according to a normal distribution (which has the typical bell shape). Since the bell shape does not allow immediate recognition, the normal probability graph allows for modify the ordinate axis, so that the cumulative normal frequency can be represented on a straight line. In this way it is possible to assess at a glance whether the trend of the experimental cumulated relative frequencies is straight or deviates significantly from it. In the latter case the normal hypothesis must be discarded.

A useful procedure for the realization of the NPP requires to the data representation to be arranged in a column, in ascending order. Based on the relative position, the cumulative relative frequency is calculated, according to the equation

$$f_{rc} = \frac{(i - 0.5)}{n} \quad (4.9)$$

where i indicates a data position.

Once the y-axis of the NPP is constructed, the abscissa of the graph is the inverse of the cumulative standard probability.

The limit of this method consists in the attribution of the straightness of the experimental data distribution is purely subjective.

4.4 The null hypothesis

At this point it must be ascertained whether the differences between the experimental data are related to accidental errors or if there are systematic factors. Hypothesis testing is used to carry out this investigation.

Statistical tools do not allow to demonstrate that a parameter is significant for roughness but it allows to demonstrate that the hypothesis that a certain parameter has no effect on roughness can be rejected, with a chosen risk factor.

This test involves a series of steps:

- identify the data representative of the influence factor;
- choose a statistical distribution that could be representative of the phenomenon analyzed;
- establish the risk of error;
- evaluate the boundaries of the area of acceptance or rejection of the hypothesis, once the statistical distribution and the level of confidence are known, as determination of a simple confidence interval.

4.5 ANOVA

Another analysis aimed at refuting the null hypothesis (the influence of a parameter on the surface roughness) is the analysis of variance.

The analysis of variance can focus on a single factor (related to column), or take into consideration several factors (related to column and rows).

In the case under consideration, the columns represent the different specimens, which have different values of the parameter whose effect is analyzed, apart from the other construction parameters. The rows are replicas, there is no reason to apply the two factor control method.

Table 4.1: Data organization [23]

#	Sample 1	...	Sample j	...	Sample k	Global average
1	x_{11}	...	x_{1j}	...	x_{1k}	
...	
i	x_{i1}	...	x_{ij}	...	x_{ik}	
...	
v	x_{v1}	...	x_{vj}	...	x_{vk}	
Column average	$\bar{x}_{\bullet 1}$...	$\bar{x}_{\bullet j}$...	$\bar{x}_{\bullet k}$	$\bar{x}_{\bullet \bullet}$

where:

- x_{ij} is the data i-th of j-th sample;
- $\bar{x}_{\bullet j}$ is the data average of the j-th sample;
- $\bar{x}_{\bullet\bullet}$ is the average between all data.

The difference between the data groups in 4.2, organized in this way, emerges in the average values obtained for each group; therefore the estimated factor s_m^2 , calculated as the variance of the mean values, strongly contain this difference. This variance is given the name of variance "between groups" because the variance calculated between the means of the groups and the calculation of this variance is carried out according to the relation 4.10

$$s_B^2 = v * s_m^2$$

$$v * \frac{\sum_{j=1}^k (\bar{x}_{\bullet j} - \bar{x}_{\bullet\bullet})^2}{k - 1} = \frac{SS_B}{k - 1} \quad (4.10)$$

it involves the Sum of Squares between groups "SS_B".

Moreover it is necessary to estimate a variance that does not contain the effect of the difference between the groups. If it is calculate the variance for only one group (variance within the group or "within the group"), the results obtained is a value that is independent of the difference between the groups. This operation is also repeated for the other groups and then an evaluation for each group is carried out, as reported in the equation 4.11

$$s_W^2 = \frac{1}{k} \sum_{j=1}^k \frac{\sum_{i=1}^v (\bar{x}_{ij} - \bar{x}_{\bullet j})^2}{v - 1}$$

$$= \frac{SS_W}{k(v - 1)} \quad (4.11)$$

where the term

$$\sum_{i=1}^v \frac{(\bar{x}_{ij} - \bar{x}_{\bullet j})^2}{v - 1} = SS_W \quad (4.12)$$

is the variance of the data within the j-th group while the Sum of Squares within groups, SS_W, is the sum of the squares of the differences to the average values of each group.

The presence of a systematic factor between the groups can be detected by the ratio between the estimate of the variance that contains the factor examined and the one that does not, then comparing the value obtained with the upper limit corresponding to the confidence interval considered of the distribution of Fisher. For this operation the total degrees of freedom are given by the total number of data minus one, i.e $kv-1$.

Based on the relations provided above it is possible to calculate the ANOVA table (ANalysis Of Variance),as shown in table 4.2

Table 4.2: ANOVA scheme for one factor

Origin of data variation	Total freedom degrees	Sum of the least squares [23]	Variance	Variance ratio	F
Related to the factor examined	k-1	SS_B	s_B^2	$F_{calc} = \frac{s_B^2}{s_w^2}$	F_U
Related to random errors	k(v-1)	SS_W	s_w^2		
Total	kv-1	$SS_{TC} = \sum_{j=1}^k \sum_{i=1}^v (\bar{x}_{ij} - \bar{x}_{\bullet\bullet})^2$			

After determining the elements making up the table, the factor F_{calc} is compared, obtained from the ratio between the calculated variances, and the factor F_U , obtained from the Fischer distribution taking into account the desired level of confidence and the degrees of freedom available for numerator and denominator.

If the value F_{calc} is higher than the theoretical value estimated with the Fisher distribution, the null hypothesis originally set cannot be denied, in other words, it is not possible to deny the influence of the parameter under consideration on the surface roughness; if not, the presence of systematic errors between the columns cannot be denied or affirmed.

4.6 Linear regression

The method of χ^2 , NPP and analysis of variance allow to detect a possible presence of systematic effects in the data collection, but do not allow the identification of these. The identification of these effects can be carried out using the regression tool, this allows you to find a relation between a dependent variable, often indicated with the letter Y and an independent variable, often indicated with the letter X. The steps to follow in a regression analysis are:

- Graphic presentation of the experimental data to identify the regression model that best describes the experimental data;
- Calculation of the parameters of the mathematical model chosen with the least squares method;

- Evaluation of residues, or the difference between the experimental data and the values calculated with the mathematical model, in order to decide whether the mathematical model adopted is adequate for the description of the experimental data;

In other words, the experimental data are analyzed globally, to identify a mathematical model that allows data trend description. If this mathematical is the linear one, it is represent as the equation of a straight line 4.13

$$x = a_0 + a_1t \quad (4.13)$$

The next step is to identify the dependent variable x and the independent variable represented by the t and the two model parameters a_0 and a_1 .

However if the best match is with a parabolic model the independent variables are more than one and that the model parameters could be more than two. Once the mathematical model has been identified, the actual calculation of the model parameters is carried out using the method of least squares, for the implementation of this model it is necessary to use the book [23]. To verify that the chosen model describes the experimental data, the residue analysis is taken into account: if the model correctly describes the experimental data, the residues will tend to arrange themselves with a random pattern; while if a possible effect due to systematic measurement errors were present within the experimental data, then the residues will tend to arrange themselves with a certain regularity. One method to verify the possible regular arrangement of residues is to study the sign of these residues. In fact, if there are no systematic effects, having positive or negative residues is accidental, otherwise the signs of the residues will assume only positive or negative values.

Chapter 5

Parameters effects analysis

5.1 Beam speed influence

The first parameter taken into account, whose influence on roughness it is observed, is the beam speed (BS).

This analysis requires the steps seen in the previous paragraphs, i.e. the identification and exclusion of data characterized by random errors (through the methods of the bloxplot and the Chauvenet exclusion principle), the comparison with the normal distribution (χ^2 and NDD) to find systematic errors, the refutation of null hypothesis (the null hypothesis and ANOVA methods) and the linear regression. The data are reported in a table 5.1, converted from μm to mm, where rows represent surfaces and columns the samples.

Table 5.1: *Experimental roughness data in millimeters for BS parameter analysis.*

Surface	Samples				
	1	3	8	9	13
1.sx	0.0418	0.0275	0.0231	0.0345	0.0351
1.c	0.0310	0.0308	0.0349	0.0318	0.0361
1.dx	0.0409	0.0322	0.0200	0.0295	0.0373
2.sx	0.0382	0.0343	0.0149	0.0276	0.0558
2.c	0.0274	0.0420	0.0294	0.0351	0.0565
2.dx	0.0328	0.0381	0.0310	0.0285	0.0575
3.sx	0.0198	0.0340	0.0261	0.0271	0.0518
3.c	0.0269	0.0363	0.0232	0.0357	0.0591
3.dx	0.0260	0.0318	0.0232	0.0264	0.0605
4.sx	0.0459	0.0426	0.0272	0.0349	0.0443
4.c	0.0661	0.0345	0.0263	0.0371	0.0408
4.dx	0.0647	0.0379	0.0254	0.0423	0.0432

The suspected errors are highlighted in red. To define which data are really measurement errors, it is necessary to calculate the mean value and the standard deviation, as shown in the table 5.2

Then the first and third quartile are calculated, and the interquartile distance and applying the relations (4.4) (4.5) the upper and lower acceptability limits of the measures are calculated, successively. The table 5.3 and the boxplot 5.1 display the results.

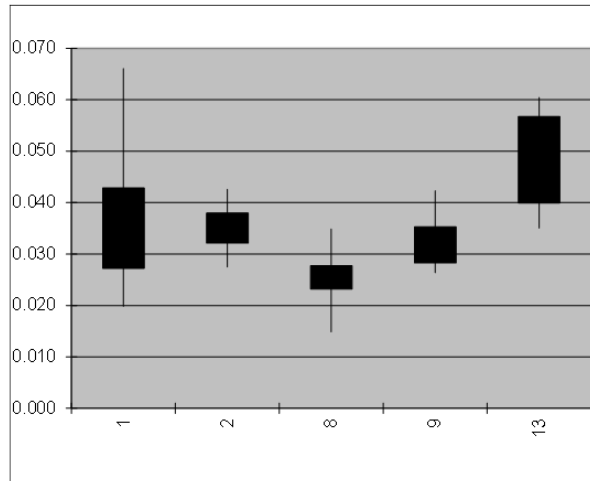
The analysis of the relative boxplot of each specimen, taking into consideration all the surfaces of the

Table 5.2: Comparison with mean value and standard deviation for BS data.

Data Number	60
Mean value	0.0360 mm
Standard deviation	0.0113 mm

Table 5.3: BS data for the detection of possible measurement errors and limits of acceptability experimental values.

	Sample 1	Sample 2	Sample 8	Sample 9	Sample 13
Quart 3	0.0429	0.0380	0.0277	0.0353	0.0568
Max	0.0661	0.0426	0.0349	0.0423	0.0605
Min	0.0198	0.0275	0.0149	0.0264	0.0351
Quart 1	0.0272	0.0321	0.0232	0.0283	0.0399
Median	0.0355	0.0344	0.0257	0.0332	0.0481
IQR	0.0156	0.0058	0.0046	0.0070	0.0168
Max IQR	0.0665	0.0468	0.0347	0.0459	0.0823
Min IQR	0.0036	0.0233	0.0163	0.0176	0.0144

**Figure 5.1:** Boxplot

specimen simultaneously, does not show an alignment between the rectangles. So the samples are not replicas. This effect may be due to measurement errors or to an effect of the beam speed on the roughness. The Chauvenet exclusion principle does not detect the presence of measurement errors, so it is not necessary to exclude any experimental data.

Once established that the experimental data are not effects of accidental errors, the next step is the analysis of any systematic errors.

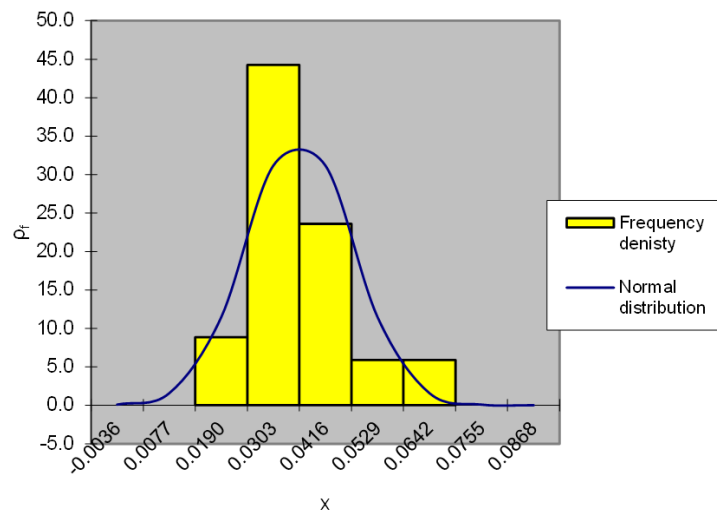
The χ^2 test, as mentioned in the previous paragraph, requires the reorganization of the experimental data as shown in the table 5.4.

The number of classes recommended are 8. With the data in the table 5.4 it is therefore possible to create the histogram of the relative frequency, shown in the figure 5.2. The distribution of the relative frequency does not show a symmetrical trend, the production process can affect experimental roughness data.

The theoretical relative frequency, the theoretical absolute frequency are determined as explained in

Table 5.4: BS data for the detection of possible measurement errors and limits of acceptability experimental values.

Class	From	To	Mean value	f_a	f_r	Frequency Density	Normal Distribution
	[mm]	[mm]	[mm]			$[mm^{-1}]$	$[mm^{-1}]$
1	-0.00924	0.00205	-0.00359	0	0.000	0.0	0.08
2	0.00205	0.01335	0.00770	0	0.000	0.0	1.55
3	0.01335	0.02465	0.01900	6	0.100	8.9	11.46
4	0.02465	0.03595	0.03030	30	0.500	44.3	31.16
5	0.03595	0.04725	0.04160	16	0.267	23.6	31.16
6	0.04725	0.05855	0.05290	4	0.067	5.9	11.46
7	0.05855	0.06985	0.06420	4	0.067	5.9	1.55
8	0.06985	0.08114	0.07550	0	0.000	0.0	0.08

**Figure 5.2:** Histogram of relative frequency for BS parameter.

the statistical elements paragraph 3.1 , while the random variable W is obtained according to relation 3.8. This operation was carried out for each class and the results of this calculation are shown in Table 5.5. The χ^2 obtained must be compared with the theoretical limits of χ^2 , obtained from the distribution of χ^2 for a level of confidence equal to 95% and with a number of degrees of freedom equal to 5. The limits of χ^2 ideal are given by:

- Lower boundary of $\chi^2 = 0.83$
- Upper boundary of $\chi^2 = 12.83$

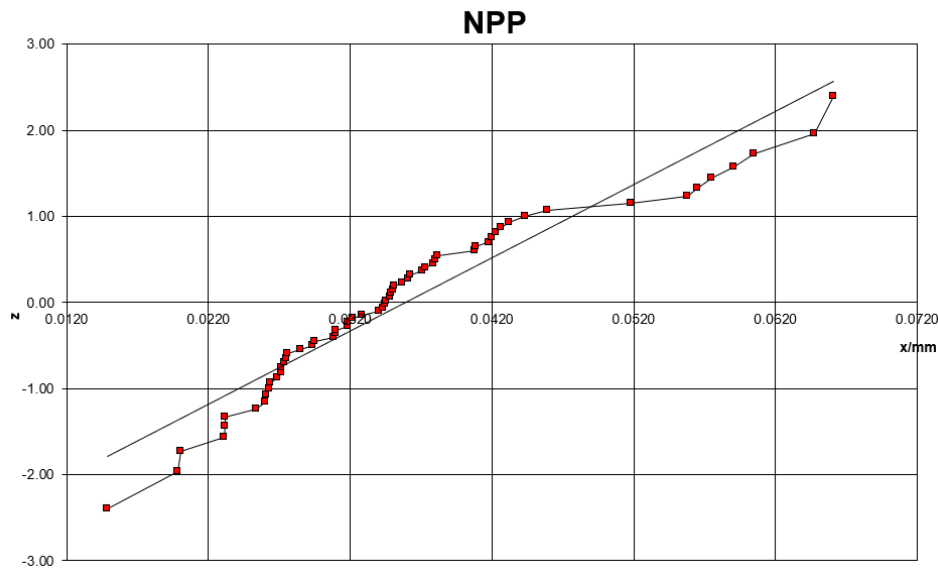
From the comparison of the experimental χ^2 , the value of which is reported at the bottom of Table 5.5, with the theoretical limits determined, it can be seen that this exceeds the limits identified, so the null hypothesis of normal distribution of the experimental data can be refused. The result of this test confirms what is anticipated by the histogram, i.e. that the data do not follow a normal distribution.

An asymmetric distribution in statistics is called "skewness" and is due to the production process. The NPP test confirms this assertion, indeed the data are not distributed on the straight line, as shown in fig 5.3, so the hypothesis of the normal distribution can be denied.

The next step is the test hypothesis, in this case the aim is to decline the statement:

Table 5.5: BS data for Evaluation of Experimental χ^2

From	To	f_{rt}	f_{at}	f_a	$\frac{(f_a - f_{at})^2}{f_{at}}$
[mm]	[mm]				
-0.00924	0.00205	0.0013	0.1	0	0.08
0.00205	0.01335	0.0214	1.3	0	1.28
0.01335	0.02465	0.1359	8.2	6	0.57
0.02465	0.03595	0.3413	20.5	30	4.42
0.03595	0.04725	0.3413	20.5	16	0.98
0.04725	0.05855	0.1359	8.2	4	2.12
0.05855	0.06985	0.0214	1.3	4	5.74
0.06985	0.08114	0.0013	0.1	0	0.08
0.08114	0.09244	0.0000	0.0	0	0.00
				Experimental χ^2	15.28

**Figure 5.3:** NPP for the BS parameter.

”The beam speed has no influence on the superficial roughness”.

The mean value of R_a is calculated for each column, which corresponds to a specific sample. These mean values, shown in the table 5.6, must be compared with the theoretical limits (tab 5.7) obtained from the cumulative normal distribution, for a confidence level in this case equal to 95%.

Table 5.6: BS data for Test hypothesis on columns.

Sample 1	Sample 2	Sample 8	Sample 9	Sample 13
0.0385	0.0352	0.0254	0.0325	0.0482

Since the values of the samples 8 and 13 exceed the limit values, then it is not possible to decline the hypothesis that the beam velocity has no effect on the roughness of the samples, in other words beam speed has an effect on roughness data.

A more significant hypothesis test is the one carried out taking into account the variance, in which the values of the variance of each sample (each column) in tab.5.8 is compared with the data relating to the

Table 5.7: Boundaries for test hypothesis on columns of BS data.

Number of samples	12
Average	0.0360
Average Standard deviation	0.0033
Confidence level	95%
Lower boundary	0.0296
Upper boundary	0.0423

cumulative distribution in tab.5.9, calculated for a confidence level equal to 95%.

Table 5.8: Variance of columns for BS samples.

Sample 1	Sample 2	Sample 8	Sample 9	Sample 13
$2.2 * 10^{-4}$	$2.0 * 10^{-5}$	$2.7 * 10^{-5}$	$2.4 * 10^{-5}$	$9.3 * 10^{-5}$

Table 5.9: Boundaries for test hypothesis on columns variance for BS samples.

Number of samples	12
Expected variance	$7.6 * 10^{-5}$
Expected v	11
Confidence level	95%
Lower boundary of s^2	$2.6 * 10^{-5}$
Upper boundary s^2	$1.5 * 10^{-4}$

Also in this case the variance values of the samples (in this case 1,2 and 9) exceed the defined limits, so it is possible to deny the initial hypothesis with a risk of 5%.

A further test to verify the effect of variation of beam speed on the data is the ANOVA test. Since this parameter varies from one specimen to another, and each column represents a different sample, the analysis of variance for a control factor is able to evaluate the effect of velocity on roughness. In this test, the average values and variance of each sample (table 5.10) are compared, then the data, shown in the table 5.11, are determined.

Table 5.10: BS data for ANOVA test.

Average	0.0385	0.0352	0.0254	0.0325	0.0482
Variance	$2.1598 * 10^{-4}$	$1.9976 * 10^{-5}$	$2.6915 * 10^{-5}$	$2.3733 * 10^{-5}$	$9.3429 * 10^{-5}$

Table 5.11: ANOVA for column control factor, for BS specimens.

Variation cause	Degrees of freedom	Variance	Variance ratio	F_{MAX}
Examined factor	4	$8.38 * 10^{-4}$	11.02	2.54
Random errors	55	$7.60 * 10^{-5}$		
Total	59			

The F_{calc} value (represents the ratio between the variances) is higher than the F Fisher factor, so it possible state that the differences between the column means are caused by the presence of systematic error, or rather the differences between roughness data are related to the variation of beam speed.

Finally, for a global analysis of the data, a regression analysis is carried out, with the aim of detecting a repeatability in the roughness measurement operation. In order to represent the experimental data globally, the linear model is initially chosen, described by equation 4.13. For this purpose, the parameters a and t are identified, in particular the independent variable t represents the beam speed parameter, while the dependent variable x represents the roughness measurement Ra. Equation 4.13, in this case, can therefore be expressed as 5.1:

$$x = 0.0164 + 1.8 * 10^{-5} * BS \quad (5.1)$$

The determination coefficient R^2 is the distance to the variance of dependent variable (in %), higher is R^2 , the better the experimental data are described by linear regression model obtained. As the image 5.4 shows R^2 is 14.6%, the linear model does not describe the experimental data efficiently.

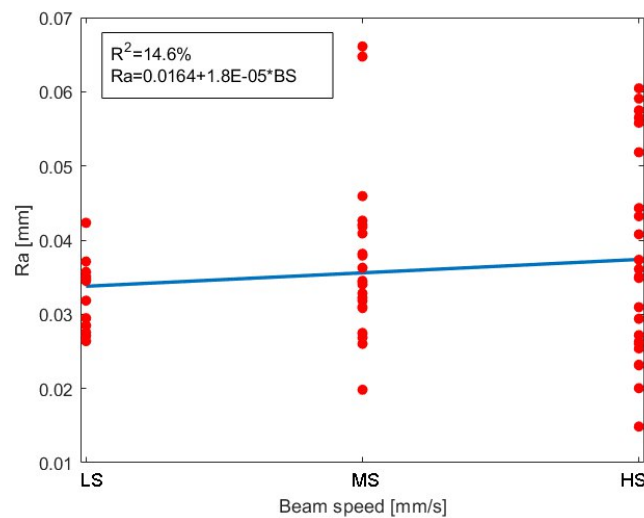


Figure 5.4: Linear regression for BS samples.

The residual plot 5.5 shows a grouping of the data into negative values with positive peaks, that further demonstrates that the linear model is not suitable for describing the distribution of data.

It is not possible to find a model that fits the data better, as the roughness values are dispersed, in particular for the medium beam speed used value (MS). Furthermore, in addition to the BS parameter, there may be another parameter that affects contemporaneously, so it is not possible to find with the linear model a direct relationship between the roughness and the BS.

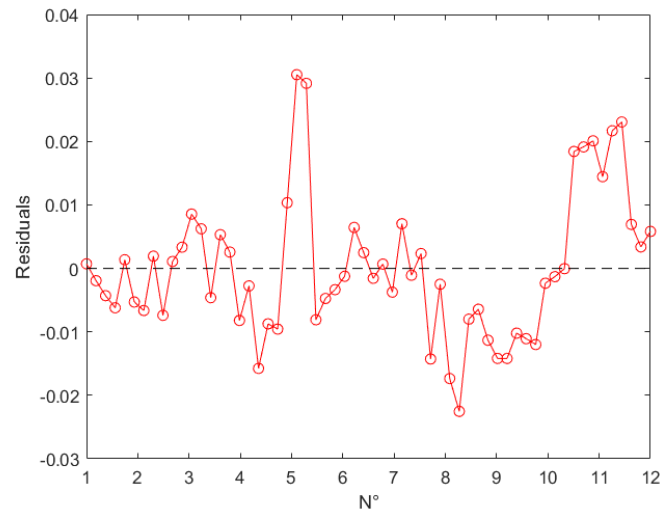


Figure 5.5: Residual from Linear regression (BS) model versus survey

5.2 Diameter influence

In this paragraph it is analyzed the effect of the variation of the beam diameter on the roughness.

The data are reported in a table 5.12, converted from μm to mm, where columns represent the samples these differ from each other for the variation in diameter of the beam.

Also in this case, the first quartile, the third quartile and the interquartile distance are identified, as done in previous paragraph, the maximum and minimum limits for each column are calculated. These values constitute the acceptability limits for the measurements and allow for an analysis of the "outliers". The data suspected accidental errors are highlighted in red. To define which data are really measurement errors, it is necessary to calculate the mean value and the standard deviation, as shown in the table 5.13. The table 5.14 and the boxplot 5.6 display the results.

Table 5.12: *Experimental roughness data in millimeters for diameter parameter analysis.*

Surface	Samples				
	6	7	10	11	14
1.sx	0.356	0.0360	0.0363	0.0360	0.0345
1.c	0.0201	0.0402	0.0343	0.0362	0.0359
1.dx	0.0337	0.0442	0.0420	0.0396	0.0359
2.sx	0.0373	0.0335	0.0397	0.0421	0.0436
2.c	0.0434	0.0321	0.0338	0.0477	0.0386
2.dx	0.0562	0.033	0.0373	0.0432	0.04
3.sx	0.0320	0.0341	0.0258	0.0392	0.0448
3.c	0.0372	0.0345	0.0265	0.0328	0.0444
3.dx	0.0365	0.0366	0.039	0.0361	0.0503
4.sx	0.0431	0.0328	0.0306	0.0428	0.0420
4.c	0.0373	0.0433	0.0359	0.0391	0.0441
4.dx	0.0411	0.0372	0.0374	0.0380	0.0411

Table 5.13: *Comparison with mean value and standard deviation for diameter parameter analysis.*

Data Number	60
Mean value	0.0380 mm
Standard deviation	0.0057 mm

Table 5.14: *Data of diameter analysis for the detection of possible measurement errors and limits of acceptability experimental values*

	Sample 6	Sample 7	Sample 10	Sample 11	Sample 14
Quart 3	0.0416	0.0380	0.0378	0.0423	0.0442
Max	0.0562	0.0442	0.0420	0.0477	0.0503
Min	0.0201	0.0321	0.0258	0.0328	0.0345
Quart 1	0.0351	0.0334	0.0330	0.0362	0.0379
Median	0.0372	0.0352	0.0361	0.0391	0.0415
IQR	0.0065	0.0046	0.0048	0.0061	0.0063
Max IQR	0.0514	0.0449	0.0451	0.0514	0.0535
Min IQR	0.0254	0.0265	0.0257	0.0270	0.0285

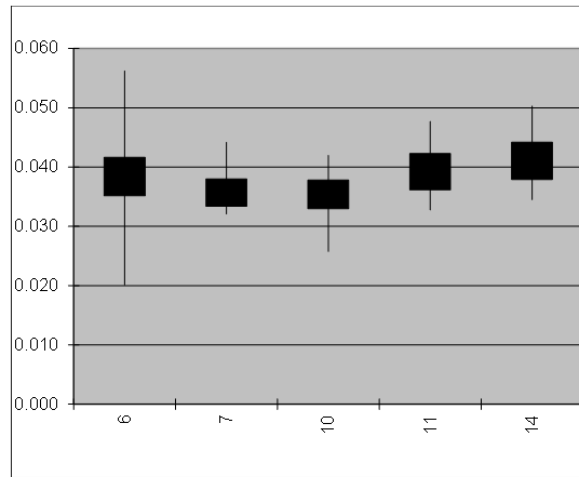


Figure 5.6: Boxplot of diameter's effect analysis.

Also in this case the boxplot does not show an alignment between the rectangles, the box of the sample 14 cannot overlap the box of the 10 one, in other word the first quartile of the sample 14 is higher than the third quartile of the 10's box. So the samples are not replicas. This effect may be due to measurement errors or to an effect beam diameter on the roughness or due to scattered data.

The Chauvenet exclusion principle excludes the highlighted data in 5.12, therefore these data can be replaced with the average roughness value. After doing that, the Chauvenet test does not highlight possible accidental errors, the next step is the analysis of any systematic errors.

The χ^2 test requires the reorganization of the experimental data as shown in the table 5.15. The number of classes recommended are 8. With the data in the table 5.15 it is therefore possible to create the histogram of the relative frequency, shown in the figure 5.7. The distribution of the relative frequency show a asymmetrical trend, related to the EBM process.

The experimental χ^2 , value at the bottom right of the table 5.16 falls within the theoretical range, obtained from the distribution of χ^2 for a level of confidence equal to 95% and with a number of degrees of freedom equal to 6. Therefore nothing can be said about the hypothesis that the experimental data follow a normal distribution.

Table 5.15: Data of diameter effect analysis for the detection of possible measurement errors and limits of acceptability experimental values

Class	From [mm]	To [mm]	Mean value [mm]	f_a	f_r	Frequency Density [mm^{-1}]	Normal Distribution [mm^{-1}]
1	0.01918	0.02388	0.02153	0	0.000	0.0	0.19
2	0.02388	0.02857	0.02622	2	0.033	7.1	3.74
3	0.02857	0.03326	0.03091	6	0.100	21.3	27.60
4	0.03326	0.03795	0.03561	24	0.400	85.2	75.02
5	0.03795	0.04265	0.04030	16	0.267	56.8	75.02
6	0.04265	0.04734	0.04499	10	0.167	35.5	27.60
7	0.04734	0.05203	0.04969	2	0.033	7.1	3.74
8	0.05203	0.05673	0.05438	0	0.000	0.0	0.19

- Lower boundary of $\chi^2 = 0.83$

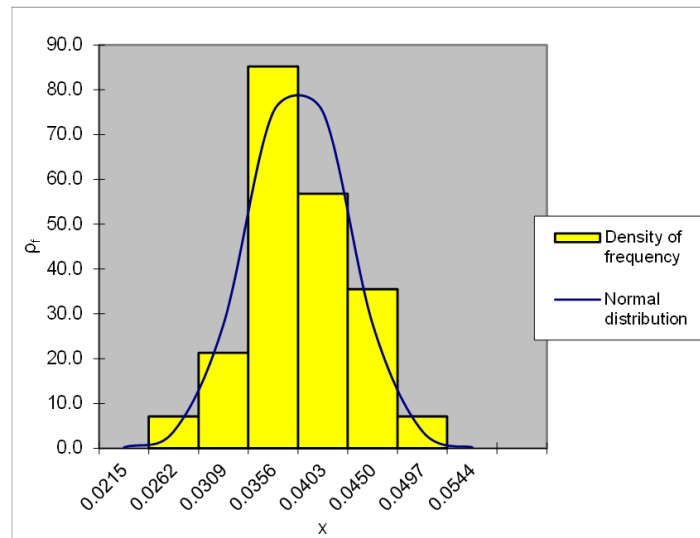


Figure 5.7: Histogram of relative frequency for diameter effect analysis.

- Upper boundary of $\chi^2 = 12.83$

Table 5.16: Data for Evaluation of Experimental χ^2

From	To	f_{rt}	f_{at}	f_a	$\frac{(f_a - f_{at})^2}{f_{at}}$
[mm]	[mm]				
0.01918	0.02388	0.0013	0.1	0	0.08
0.02388	0.02857	0.0214	1.3	2	0.40
0.02857	0.03326	0.1359	8.2	6	0.57
0.03326	0.03795	0.3413	20.5	24	0.60
0.03795	0.04265	0.3413	20.5	16	0.98
0.04265	0.04734	0.1359	8.2	10	0.42
0.04734	0.05203	0.0214	1.3	2	0.40
0.05203	0.05673	0.0013	0.1	0	0.08
				Experimental χ^2	3.53

In the NPP 5.8 points deviate from the straight line, which represents the normal distribution, only at extremes, but it is a graph method, so it is not possible to reject the normal hypothesis.

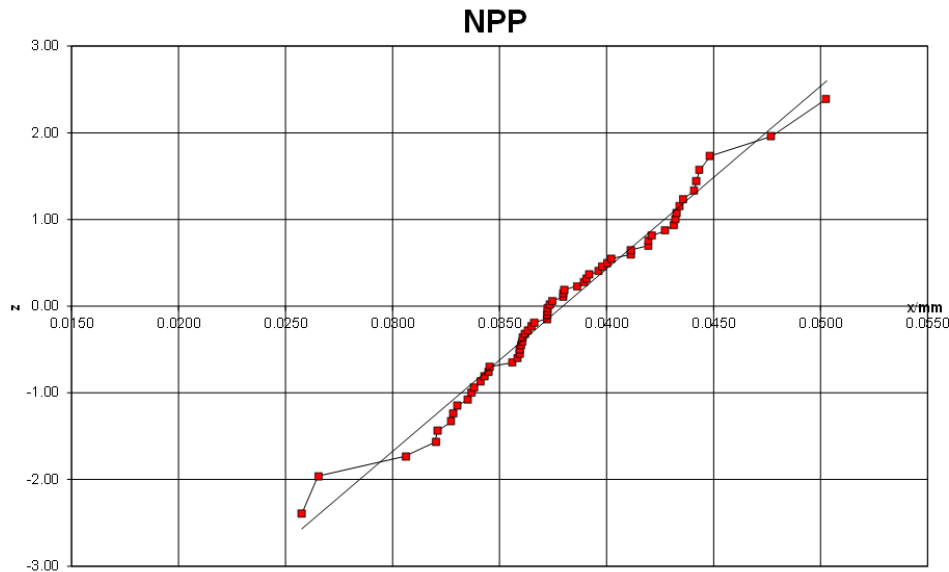


Figure 5.8: *NPP*

The next step is the test hypothesis, in this case the aim is to decline the statement:

”The beam diameter has no influence on the superficial roughness”.

These mean values of R_a for each column, shown in the table 5.17, must be compared with the theoretical limits (tab 5.18) obtained from the cumulative normal distribution, for a confidence level in this case equal to 95%

Table 5.17: *Data for Test hypothesis on columns*

Sample 6	Sample 7	Sample 10	Sample 11	Sample 14
0.0378	0.0365	0.0349	0.0394	0.0413

Table 5.18: *Boundary for test hypothesis on columns*

Number of samples	12
Average	0.0380
Average Standard deviation	0.0014
Confidence level	95%
Lower boundary	0.0353
Upper boundary	0.0406

The column average values of samples 10 and 14 exceed the limit values, then it is not possible to decline the hypothesis that a variation in beam diameter does not involve a systematic effect on the roughness. A more significant test, to confirm that assessment, is the variance hypothesis. It takes into account the variance distribution, in which the values of the variance of each sample (each column) in tab.5.8 is compared with the data relating to the cumulative distribution in tab.5.9, calculated for a confidence level equal to 95%.

Table 5.19: *Variance of columns*

Sample 6	Sample 7	Sample 10	Sample 11	Sample 14
$1.2 * 10^{-5}$	$1.7 * 10^{-5}$	$2.5 * 10^{-5}$	$1.6 * 10^{-4}$	$2.1 * 10^{-5}$

Table 5.20: *Boundary for test hypothesis on columns variance*

Number of samples	12
Expected variance	$3.0 * 10^{-5}$
Expected v	11
Confidence level	95%
Lower boundary of s^2	$1.0 * 10^{-5}$
Upper boundary s^2	$6.0 * 10^{-5}$

In this case the variance values fall in the theoretical range, so it is not possible to confirm or reject the null hypothesis.

Therefore the ANOVA where, the average values and variance of each samples are reported in the table 5.21 and ANOVA scheme in the table 5.22, shows the possibility of a systematic error.

Table 5.21: *Data for ANOVA test*

Average	0.0378	0.0365	0.0349	0.0394	0.0413
Variance	$7.0961 * 10^{-5}$	$1.6621 * 10^{-5}$	$2.5393 * 10^{-5}$	$1.6467 * 10^{-5}$	$2.0810 * 10^{-5}$

Table 5.22: *ANOVA for column control factor*

Variation cause	Degrees of freedom	Variance	Variance ratio	F_{MAX}
Examined factor	4	$7.45 * 10^{-5}$	4.09	2.54
Random errors	55	$1.82 * 10^{-5}$		
Total	59			

In conclusion it is possible to reject that the beam diameter has no effect on the roughness, with a risk of 5%.

For the study of the effect of the diameter, linear regression is not applied to search for a direct relationship between diameter and roughness, as the diameter is not a parameter that can be set in the EBM machine but depends on the focus offset and the referent current.

5.3 Beam current influence

The third parameter, whose influence on roughness it is observed, is the beam current.

The R_a data are reported in a table 5.23, converted from μm to mm, where columns represent the samples and differ in beam current.

To identify accidental error the roughness data are compared with the mean value and standard deviation,

Table 5.23: *Experimental data of samples 1-6-7 in millimeters*

Surface	Samples		
	1	6	7
1.sx	0.0418	0.0356	0.0360
1.c	0.0310	0.0201	0.0402
1.dx	0.0409	0.0337	0.0442
2.sx	0.0382	0.0373	0.0335
2.c	0.0274	0.0434	0.0321
2.dx	0.0328	0.0562	0.0330
3.sx	0.0198	0.0320	0.0341
3.c	0.0269	0.0372	0.0345
3.dx	0.0260	0.0365	0.0366
4.sx	0.0459	0.0431	0.0328
4.c	0.0661	0.0373	0.0433
4.dx	0.0647	0.0411	0.0372

in tab5.24. To sketch the boxplot, the table 5.25 shows the values of the first and third quartiles, the interquartile distance and outlines the extremes of the intervals, beyond which the roughness values are highly likely to error.

Table 5.24: *Comparison with mean value and standard deviation*

Data Number	36
Mean value	0.0376 mm
Standard deviation	0.0098 mm

Table 5.25: *Data for the detection of possible measurement errors and limits of acceptability experimental values*

	Sample 1	Sample 6	Sample 7
Quart 3	0.0429	0.0416	0.0380
Max	0.0661	0.0562	0.0442
Min	0.0198	0.0201	0.0321
Quart 1	0.0272	0.0351	0.0334
Median	0.0355	0.0372	0.0352
IQR	0.0156	0.0065	0.0046
Max IQR	0.0663	0.0514	0.0449
Min IQR	0.0038	0.0254	0.0265

The boxes may overlap this suggests that the samples are replicas, i.e. the variation of the beam current

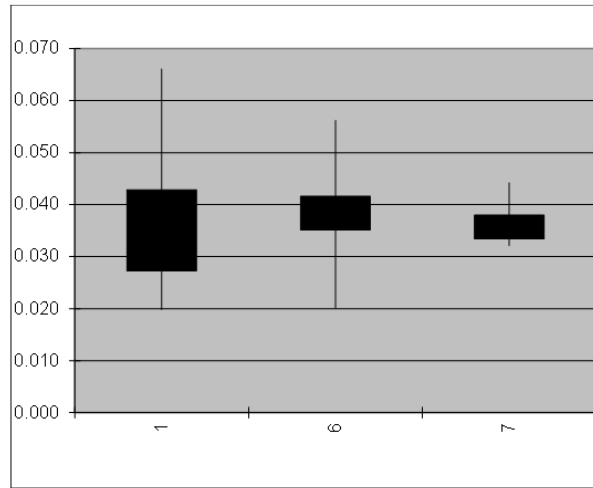


Figure 5.9: Boxplot

does not affect the roughness. The Chauvenet method does not confirm suspected data, so there should be no measurement errors.

As seen in the previous paragraphs, the hypothesis that the data follows a normal distribution can be denied through two methods: the χ^2 method and the NPP one. The data for the first method are reorganized and display in Tab 5.26:

Table 5.26: Data for the detection of possible measurement errors and limits of acceptability experimental values

Class	From [mm]	To [mm]	Mean value [mm]	f_a	f_r	Frequency Density [mm^{-1}]	Normal Distribution [mm^{-1}]
1	-0.00164	0.01143	0.00489	0	0.000	0.0	0.16
2	0.01143	0.02450	0.01797	2	0.056	4.3	5.51
3	0.02450	0.03757	0.03104	21	0.583	44.6	32.58
4	0.03757	0.05064	0.04411	10	0.278	21.3	32.58
5	0.05064	0.06372	0.05718	1	0.028	2.1	5.51
6	0.06372	0.07679	0.07025	2	0.056	4.3	0.16
7	0.07679	0.08986	0.08332	0	0.000	0.0	0.00

The number of classes recommended are 6. With the data in the table 5.26 it is therefore possible to create the histogram of the relative frequency, shown in the figure 5.10. The distribution of the relative frequency does not show a symmetrical trend, as already mentioned in the previous paragraph, the production process can affect experimental roughness data.

To find systematic errors, the experimental χ^2 (in tab 5.27) is compared with the theoretical limits of χ^2 , obtained from the distribution of χ^2 for a level of confidence equal to 95% and with a number of degrees of freedom equal to 5. The limits of χ^2 ideal are given by:

- Lower boundary of $\chi^2 = 0.22$
- Upper boundary of $\chi^2 = 9.35$

Since the experimental value of χ^2 is outside the theoretical range then the hypothesis of normal distribution can be refused. The graph 5.11 shows a strong deviation of the points from the straight line, so

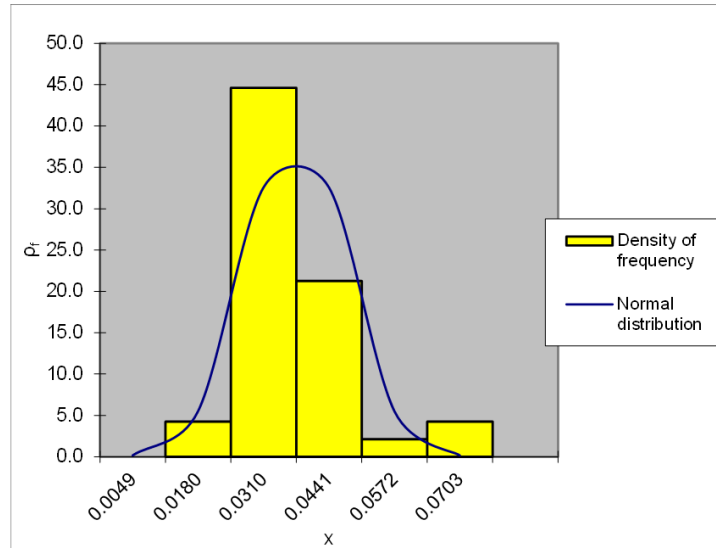


Figure 5.10: Histogram of relative frequency

Table 5.27: Data for Evaluation of Experimental χ^2

From	To	f_{rt}	f_{at}	f_a	$\frac{(f_a - f_{at})^2}{f_{at}}$
[mm]	[mm]				
-0.00164	0.01143	0.0038	0.1	0	0.14
0.01143	0.02450	0.0874	3.1	2	0.42
0.02450	0.03757	0.4088	14.7	21	2.68
0.03757	0.05064	0.4088	14.7	10	1.51
0.05064	0.06372	0.0874	3.1	1	1.46
0.06372	0.07679	0.0038	0.1	2	5.39
0.07679	0.08986	0.0000	0.0	0	0.00
				Experimental χ^2	31.60

this method also confirms the impossibility of representing the data with a linear distribution

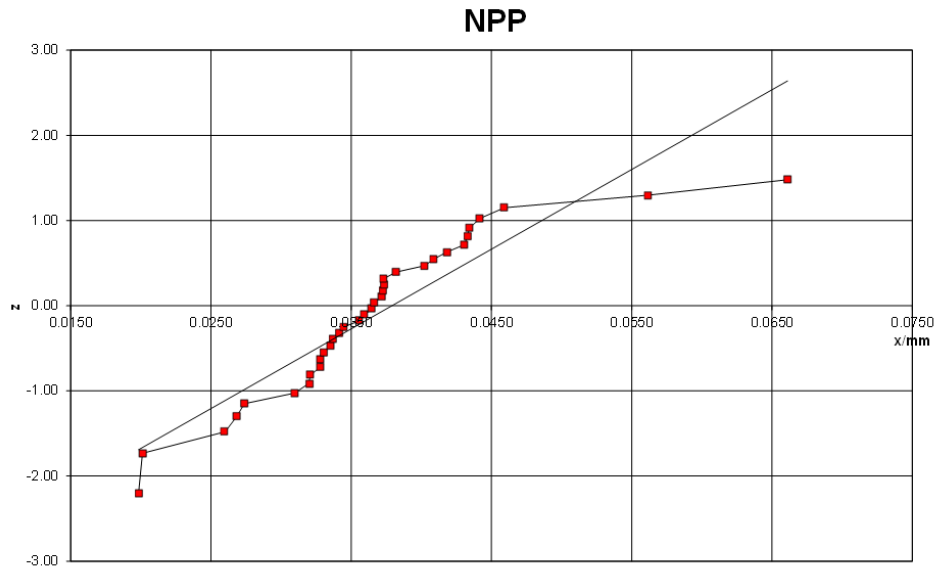


Figure 5.11: NPP

The null hypothesis to decline in this case is the statement:

”The beam current has no influence on the superficial roughness”.

The mean values of R_a are calculated for each column, which corresponds to a specific sample. These mean values, shown in the table 5.28, are contrasted with the theoretical limits (tab 5.29 obtained from the cumulative normal distribution, for a confidence level equal to 95%).

Table 5.28: Data for Test hypothesis on columns

Sample 1	Sample 6	Sample 7
0.0385	0.0378	0.0365

Table 5.29: Boundary for test hypothesis on columns

Number of samples	12
Average	0.0376
Average Standard deviation	0.0028
Confidence level	95%
Lower boundary	0.0320
Upper boundary	0.0431

The column roughness average falls in the theoretical range, so it is not possible to decline or affirm the null hypothesis. This result is in contrast with the test hypothesis for column variances, where the values are reported in table 5.30, and compared with the theoretical limits in the table 5.31.

Table 5.30: Variance of columns

Sample 1	Sample 6	Sample 7
$2.2 * 10^{-4}$	$7.1 * 10^{-5}$	$1.7 * 10^{-5}$

Table 5.31: Boundary for test hypothesis on columns variance

Number of samples	12
Expected variance	$1.0 * 10^{-4}$
Expected v	11
Confidence level	95%
Lower boundary of s^2	$3.5 * 10^{-5}$
Upper boundary s^2	$2.0 * 10^{-4}$

Indeed the result of this test allows to reject the null hypothesis, so it is not possible to deny the effect of the beam current on the roughness. To confirm this statement it is necessary to carry out the ANOVA test, in which also in this case the control factor is represented by the columns, which differ in the parameter taken into consideration. The average and variance data for columns are shown in tab 5.32.

Table 5.32: Data for ANOVA test

Average	0.0385	0.0378	0.0365
Variance	$2.1598 * 10^{-4}$	$7.0961 * 10^{-5}$	$1.6621 * 10^{-5}$

Then it is possible complete the ANOVA scheme as shown in the following table 5.33

Table 5.33: ANOVA for column control factor

Variation cause	Degrees of freedom	Variance	Variance ratio	F_{MAX}
Examined factor	2	$1.24 * 10^{-5}$	0.12	3.28
Random errors	33	$1.01 * 10^{-4}$		
Total	35			

The F_{calc} value (represents the ratio between the variances) is lower than the F Fisher factor, so it is not possible state that the differences between the column means are caused by the presence of systematic error.

5.4 Focus offset influence

In this paragraph the effect of the variation of the focus offset on the roughness is observed.

The data are reported in a table 5.34, converted from μm to mm, where columns represent the samples these differ for the variation in focus offset.

Also in this case, the first quartile, the third quartile and the interquartile distance are identified, as done in previous paragraphs, the maximum and minimum limits for each column are calculated. These values constitute the acceptability limits for the measurements and allow for an analysis of the "outliers". The data suspected accidental errors are highlighted in red. To define which data are really measurement errors, in order to calculate the mean value and the standard deviation, as shown in the table 5.36. The table 5.35 and the boxplot in Fig. 5.17 display the results.

Table 5.34: *Experimental data in millimeters*

Surface	Samples		
	3	4	5
1.sx	0.0377	0.0230	0.0427
1.c	0.0367	0.0272	0.0363
1.dx	0.0430	0.0418	0.0403
2.sx	0.0294	0.0299	0.0401
2.c	0.0309	0.0364	0.0380
2.dx	0.0399	0.0399	0.0416
3.sx	0.0370	0.0327	0.0364
3.c	0.0371	0.0300	0.0369
3.dx	0.0362	0.0274	0.0463
4.sx	0.0359	0.0323	0.0362
4.c	0.0415	0.0414	0.0452
4.dx	0.0356	0.0452	0.0364

Table 5.35: *Comparison with mean value and standard deviation*

Data Number	36
Mean value	0.0368 mm
Standard deviation	0.0090 mm

Table 5.36: *Data for the detection of possible measurement errors and limits of acceptability experimental values*

	Sample 1	Sample 4	Sample 5
Quart 3	0.0382	0.0403	0.0419
Max	0.0430	0.0452	0.0463
Min	0.0294	0.0230	0.0362
Quart 1	0.0358	0.0293	0.0364
Median	0.0369	0.0325	0.0391
IQR	0.0024	0.0110	0.0055
Max IQR	0.0418	0.0568	0.0501
Min IQR	0.0323	0.0128	0.0282

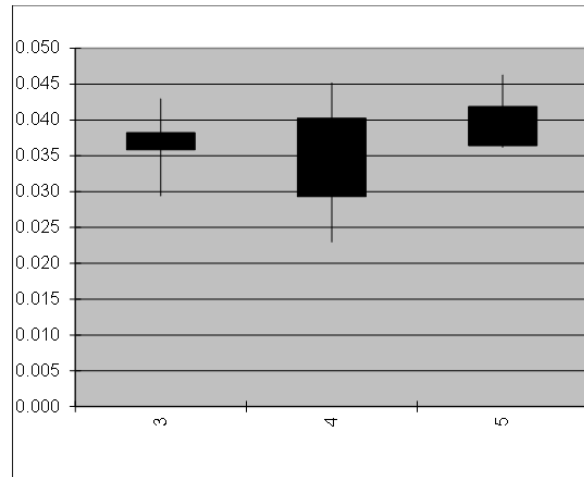


Figure 5.12: *Boxplot*

As shown in the boxplot the first quartile of sample 3 is higher than the third one of sample 5, it is a sign of scattering data. The Chauvenet method does not confirm data suspected to be due to a measurement accident.

The next step, as seen in the previous paragraphs, involves comparing the distribution of the data with the normal distribution. The χ^2 test requires the reorganization of the experimental data as shown in the table 5.37 number of classes recommended are 6. With the data in the table 5.4 it is therefore possible to create the histogram of the relative frequency, shown in the figure 5.13. The distribution of the relative frequency shows a symmetrical trend.

Table 5.37: *Data for the detection of possible measurement errors and limits of acceptability experimental values*

Class	From [mm]	To [mm]	Mean value [mm]	f_a	f_r	Frequency Density [mm^{-1}]	Normal Distribution [mm^{-1}]
1	0.01503	0.02229	0.01866	0	0.000	0.0	0.28
2	0.02229	0.02954	0.02591	4	0.111	15.3	9.93
3	0.02954	0.03679	0.03316	14	0.389	53.6	58.73
4	0.03679	0.04404	0.04042	15	0.417	57.5	58.73
5	0.04404	0.05129	0.04767	3	0.083	11.5	9.93
6	0.05129	0.05855	0.05492	0	0.000	0.0	0.28

The experimental χ^2 obtained is compared with the theoretical limits of χ^2 , obtained from the distribution of χ^2 for a level of confidence equal to 95% and with a number of degrees of freedom equal to 3. The limits of χ^2 ideal are given by:

- Lower boundary of $\chi^2 = 0.22$
- Upper boundary of $\chi^2 = 9.35$

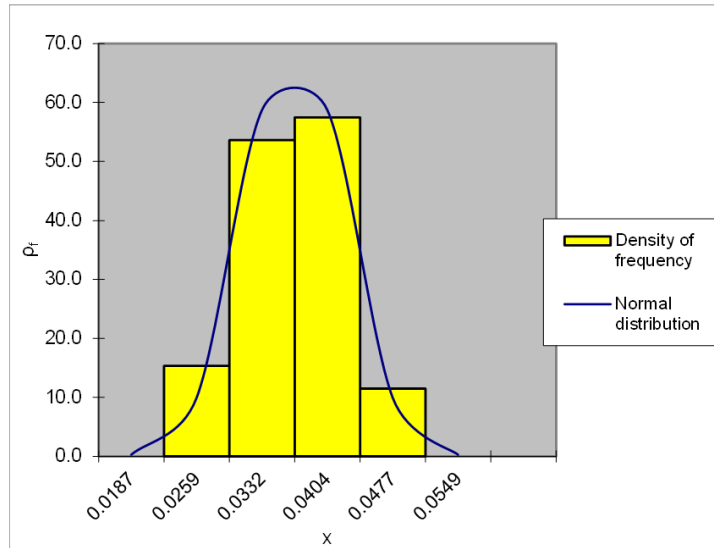


Figure 5.13: Histogram of relative frequency

Table 5.38: Data for Evaluation of Experimental χ^2

From	To	f_{rt}	f_{at}	f_a	$\frac{(f_a - f_{at})^2}{f_{at}}$
[mm]	[mm]				
0.01503	0.02229	0.0038	0.1	0	0.14
0.02229	0.02954	0.0874	3.1	4	0.23
0.02954	0.03679	0.4088	14.7	14	0.03
0.03679	0.04404	0.4088	14.7	15	0.01
0.04404	0.05129	0.0874	3.1	3	0.01
0.05129	0.05855	0.0038	0.1	0	0.14
0.05855	0.06580	0.0000	0.0	0	0.00
				Experimental χ^2	0.55

From the comparison of the experimental χ^2 , whose value is reported at the bottom of Table 5.38, with the theoretical limits, it can be seen that this does not exceed the limits identified, so the null hypothesis of normal distribution cannot be refused or confirmed.

The NPP in figure 5.14 shows a trend in which the points do not differ much from the normal distribution represented by the line.

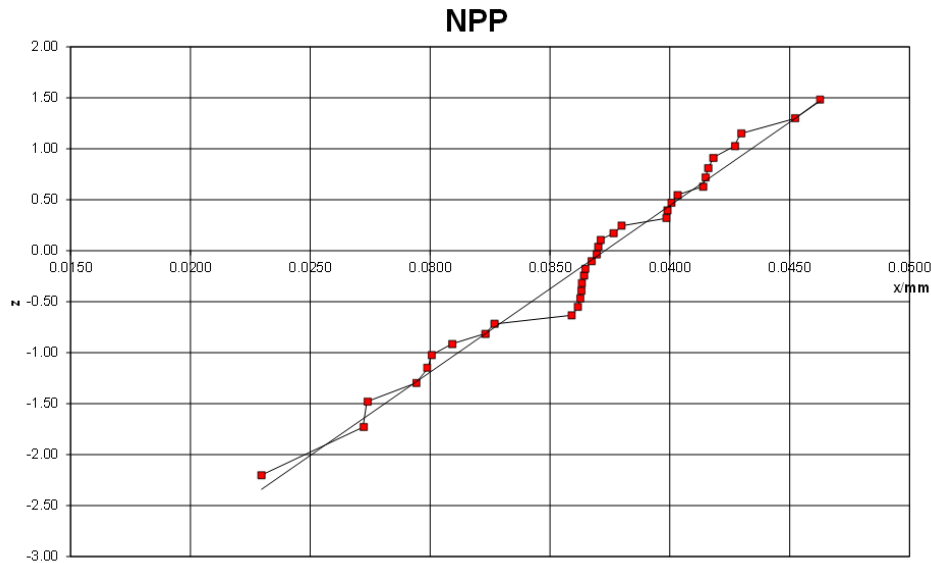


Figure 5.14: NPP

The test hypothesis in this case has the aim is to decline the statement:

”The line offset has no influence on the superficial roughness”.

The mean values of R_a for each column, shown in the table 5.39, are compared with the theoretical limits (tab 5.40) obtained from the cumulative normal distribution, for a confidence level in this case equal to 95%.

Table 5.39: Data for Test hypothesis on columns

Sample 3	Sample 4	Sample 5
0.0367	0.2055	0.0397

Table 5.40: Boundary for test hypothesis on columns

Number of samples	12
Average	0.0368
Average Standard deviation	0.0016
Confidence level	95%
Lower boundary	0.0337
Upper boundary	0.0399

Since the values of the sample 4 exceeds the limit values, it is not possible to reject the hypothesis that the line offset has no effect on the roughness of the samples.

A confirmation of that carries out taking into account the variance, in which the values of the variance of each sample (each column) in tab.5.41 is compared with the data relating to the cumulative distribution in tab.5.42, calculated for a confidence level equal to 95%.

The values of column variance fall in the theoretical limits, so it is not possible to deny or confirm the effect of focus offset on the roughness. To have a confirmation of an effect of this parameter it is necessary to carry out the ANOVA test.

Table 5.41: Variance of columns

Sample 3	Sample 4	Sample 5
$1.5 * 10^{-5}$	$4.8 * 10^{-5}$	$1.3 * 10^{-5}$

Table 5.42: Boundary for test hypothesis on columns variance

Number of samples	12
Expected variance	$2.5 * 10^{-5}$
Expected v	11
Confidence level	95%
Lower boundary of s^2	$8.8 * 10^{-6}$
Upper boundary s^2	$5.0 * 10^{-5}$

The average and variance data for columns are shown in tab5.43. The ANOVA scheme in tab 5.44 shows

Table 5.43: Data for ANOVA test

Average	0.0367	0.0339	0.0397
Variance	$1.4720 * 10^{-5}$	$4.8214 * 10^{-5}$	$1.3040 * 10^{-5}$

that F_{calc} is higher than F_U , so it is possible affirm, with the risk of error of 5% that differences among the columns are systematic. In other words it is no possible to deny that the focus offset has an effect on the roughness.

Table 5.44: ANOVA for column control factor

Variation cause	Degrees of freedom	Variance	Variance ratio	F_{MAX}
Examined factor	2	$9.98 * 10^{-5}$	3.94	3.28
Random errors	33	$2.53 * 10^{-5}$		
Total	35			

In order to identify systematic effects and the source of them a linear regression is carried out. The result of linear regression, obtained by Matlab, are shown in fig5.15, where the linear equation is 5.2

$$x = 0.00338 + 0.0001 * 10^{-3} * t \quad (5.2)$$

In equation 5.2 x (independent variable) is FO in mA, while y (dependent variable) is Ra in mm. The linear model describes experimental data with a coefficient $R^2=50.7\%$, it is higher than one obtained in the beam speed case.

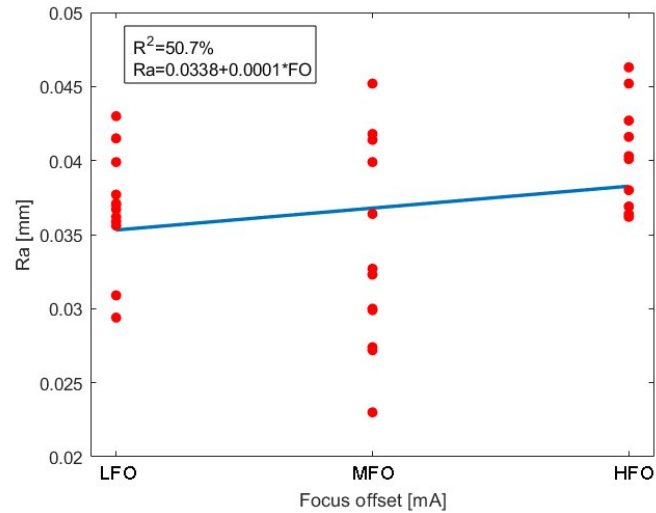


Figure 5.15: Linear regression

The data related to MFO (medium focus offset value) are scattered so they do not influence the linear regression model. The residuals, shown in Fig.5.16, are well distributed, that suggests the data are described efficiently by the linear model.

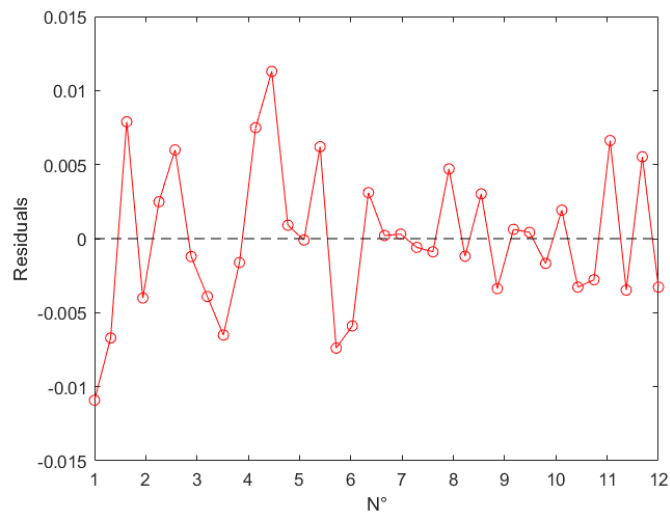


Figure 5.16: Residual from Linear regression model versus survey

The trend of linear regression plot suggests that the roughness decreases as the FO parameter increases, but in order to confirm this assumption other samples with intermediate FO will produce.

5.5 Line offset influence

The last section analyzed the effect of the line offset on the roughness.

The R_a data are reported in a table 5.45, converted from μm to mm, where columns represent the samples and differ in beam current .

Table 5.45: *Experimental data in millimeters*

Surface	Samples		
	3	4	5
1.sx	0.0418	0.0275	0.0377
1.c	0.0310	0.0308	0.0367
1.dx	0.0409	0.0322	0.0430
2.sx	0.0382	0.0343	0.0294
2.c	0.0274	0.0420	0.0309
2.dx	0.0328	0.0381	0.0399
3.sx	0.0198	0.0340	0.0370
3.c	0.0269	0.0363	0.0371
3.dx	0.0260	0.0318	0.0362
4.sx	0.0459	0.0426	0.0359
4.c	0.0661	0.0345	0.0415
4.dx	0.0647	0.0379	0.0956

To identify accidental error the roughness data are compared with the mean value and standard deviation, in Tab5.46. To sketch the box-plot, the table 5.47 shows the values of the first and third quartiles, the interquartile distance and outlines the extremes of the intervals, beyond which the roughness values are highly likely to error.

Table 5.46: *Comparison with mean value and standard deviation*

Data Number	36
Mean value	0.0368 mm
Standard deviation	0.0054 mm

Table 5.47: *Data for the detection of possible measurement errors and limits of acceptability experimental values*

	Sample 1	Sample 2	Sample 3
Quart 3	0.0429	0.0380	0.0382
Max	0.0661	0.0426	0.0430
Min	0.0198	0.0275	0.0294
Quart 1	0.0272	0.0321	0.0358
Median	0.0355	0.0344	0.0369
IQR	0.0156	0.0058	0.0024
Max IQR	0.0663	0.0467	0.0418
Min IQR	0.0038	0.0234	0.0323

The boxes may overlap this suggests that the samples are replicas, i.e. the variation of the beam current does not affect the roughness. The Chauvenet method does not confirm outliers.

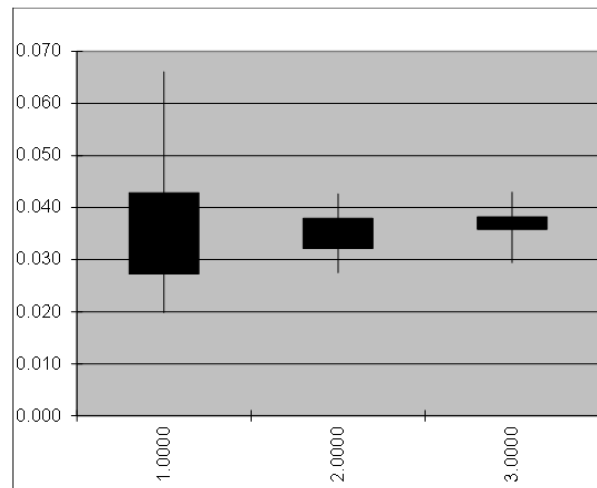


Figure 5.17: Boxplot

The χ^2 test requires the reorganization of the experimental data as shown in the table 5.48. The number of classes recommended are 6. Then it is possible to create the histogram of the relative frequency, shown in the figure 5.18. The penultimate class is not populated due to scattering data also distribution of the relative frequency shows an asymmetrical trend due to the EBM process.

The experimental χ^2 , value at the bottom right of the table 5.16 falls within the theoretical range, obtained from the distribution of χ^2 for a level of confidence equal to 95% and with a number of degrees of freedom equal to 6. Therefore nothing can be said about the hypothesis that the experimental data follow a normal distribution.

Table 5.48: Data for the detection of possible measurement errors and limits of acceptability experimental values

Class	From [mm]	To [mm]	Mean value [mm]	f_a	f_r	Frequency Density [mm^{-1}]	Normal Distribution [mm^{-1}]
1	0.00088	0.01285	0.00686	0	0.000	0.0	0.17
2	0.01285	0.02482	0.01884	1	0.028	2.3	6.01
3	0.02482	0.03680	0.03081	19	0.528	44.1	35.58
4	0.03680	0.04877	0.04278	14	0.389	32.5	35.58
5	0.04877	0.06074	0.05475	0	0.000	0.0	6.01
6	0.06074	0.07271	0.06673	2	0.056	4.6	0.17
7	0.07271	0.08468	0.07870	0	0.000	0.0	0.00

The experimental χ^2 is compared with the theoretical limits of χ^2 , obtained from the distribution of χ^2 for a level of confidence equal to 95% and with a number of degrees of freedom equal to 3. The limits of χ^2 ideal are given by:

- Lower boundary of $\chi^2 = 0.48$
- Upper boundary of $\chi^2 = 11.14$

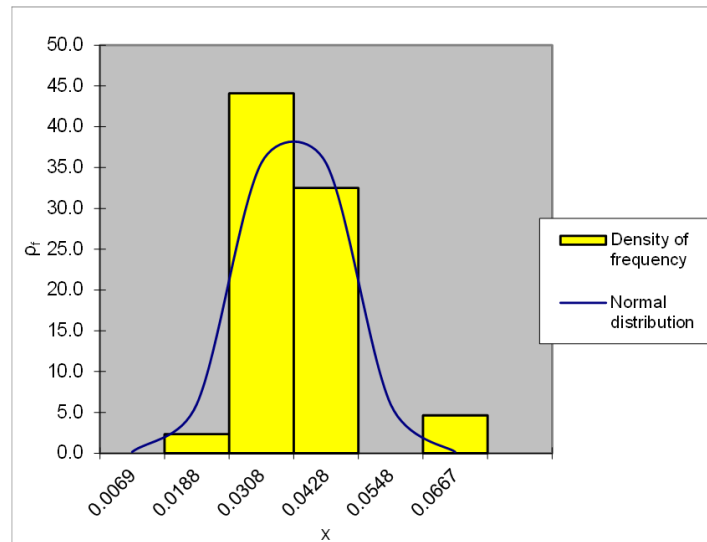


Figure 5.18: Histogram of relative frequency

Table 5.49: Data for Evaluation of Experimental χ^2

From	To	f_{rt}	f_{at}	f_a	$\frac{(f_a - f_{at})^2}{f_{at}}$
[mm]	[mm]				
0.00088	0.01285	0.0038	0.1	0	0.14
0.01285	0.02482	0.0874	3.1	1	1.46
0.02482	0.03680	0.4088	14.7	19	1.25
0.03680	0.04877	0.4088	14.7	14	0.03
0.04877	0.06074	0.0874	3.1	0	3.15
0.06074	0.07271	0.0038	0.1	2	25.39
0.07271	0.08468	0.0000	0.0	0	0.00
				Experimental χ^2	31.42

From the comparison of the experimental χ^2 , whose value is displayed at the bottom of Table 5.49, with the theoretical limits, it can be seen that this exceeds the limits identified, so the null hypothesis of normal distribution of the experimental data can be refused.

The NPP test confirms this assertion, indeed the data are not distributed on the straight line, as shown in Fig. 5.19, so the hypothesis of the normal distribution can be denied.

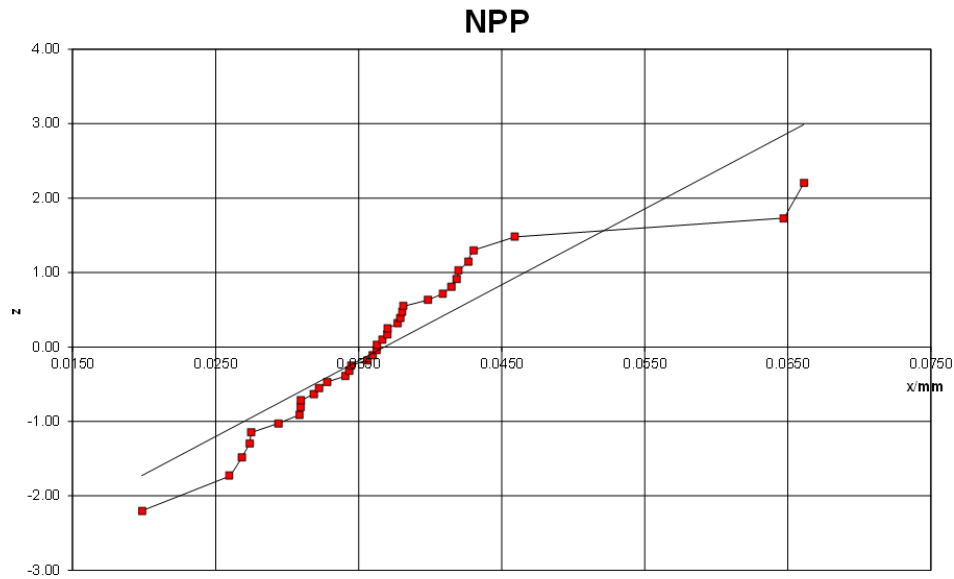


Figure 5.19: NPP

The null hypothesis to decline in this last case is the statement:

”The line offset has no influence on the superficial roughness”.

The mean values of R_a are calculated for each column, which corresponds to a specific sample. These values, shown in the table 5.50, are compared with the theoretical limits (tab 5.51 obtained from the cumulative normal distribution, for a confidence level in this case equal to 95%).

Table 5.50: Data for Test hypothesis on columns

Sample 1	Sample 2	Sample 3
0.0385	0.0352	0.0367

Table 5.51: Boundary for test hypothesis on columns

Number of samples	12
Average	0.0368
Average Standard deviation	0.0026
Confidence level	95%
Lower boundary	0.0317
Upper boundary	0.0419

The column averages fall in the limit values, it is not possible to decline or affirm the null hypothesis.

The values of the variance of each sample in tab.5.52 is compared with the data relating to the cumulative distribution in tab.5.53, calculated for a confidence level equal to 95%.

The results of this test are opposite to the previous ones, in this case the variance of each column is beyond the theoretical limit.

These conflicting results need comparison with a more rigorous test, the ANOVA test on the variability of the column effects.

Table 5.52: *Variance of columns*

Sample 1	Sample 2	Sample 3
$2.2 * 10^{-4}$	$2.0 * 10^{-5}$	$1.5 * 10^{-5}$

Table 5.53: *Boundary for test hypothesis on columns variance*

Number of samples	12
Expected variance	$8.4 * 10^{-5}$
Expected v	11
Confidence level	95%
Lower boundary of s^2	$2.9 * 10^{-5}$
Upper boundary s^2	$1.7 * 10^{-4}$

The variance values are shown in the table 5.54 and compared with the theoretical limits in table 5.55.

Table 5.54: *Data for ANOVA test*

Average	0.0385	0.0352	0.0367
Variance	$2.1598 * 10^{-4}$	$1.9976 * 10^{-5}$	$1.4720 * 10^{-5}$

Table 5.55: *ANOVA for column control factor*

Variation cause	Degrees of freedom	Variance	Variance ratio	F_{MAX}
Examined factor	2	$3.23 * 10^{-5}$	0.39	3.28
Random errors	33	$8.36 * 10^{-5}$		
Total	35			

This last test does not allow to negate the null hypothesis, so the variation of the variance in the second hypothesis test can be linked to systematic errors in the measurements that have to be correct.

5.6 Contour parameters

The last section analyzed the effect of contour parameters, i.e the multispot overlap (MO) and spot time (ST), on the roughness.

The R_a data are reported in a table 5.56 for ST data and 5.57 for MO data, converted from μm to mm.

Table 5.56: Experimental data ST in mm.

Surface	Samples		
	24	25	30
1.sx	0.0224	0.0306	0.0193
1.c	0.0217	0.0344	0.0240
1.dx	0.0212	0.0281	0.0238
2.sx	0.0310	0.0315	0.0278
2.c	0.0315	0.0351	0.0304
2.dx	0.0284	0.0332	0.0328
3.sx	0.0145	0.0230	0.0381
3.c	0.0237	0.0253	0.0355
3.dx	0.0215	0.0221	0.0346
4.sx	0.0326	0.0301	0.0360
4.c	0.0238	0.0324	0.0307
4.dx	0.0306	0.0304	0.0377

Table 5.57: Experimental data MO in mm.

Surface	Samples		
	32	30	31
1.sx	0.0193	0.0227	0.0232
1.c	0.0240	0.0281	0.0229
1.dx	0.0238	0.0245	0.0231
2.sx	0.0278	0.0303	0.0331
2.c	0.0304	0.033	0.0409
2.dx	0.0328	0.0364	0.0321
3.sx	0.0381	0.0269	0.0243
3.c	0.0355	0.0270	0.0238
3.dx	0.0346	0.0248	0.0266
4.sx	0.0360	0.0331	0.0375
4.c	0.0307	0.0293	0.0338
4.dx	0.0377	0.0317	0.0321

These data can be analyzed as seen for the data relating to the hatch parameters, in this case no accidental data emerge from the boxplot and the Chauvenet method and the distribution follows the linear model (the experimental χ^2 falls within the theoretical limits), for both parameters analyzed.

The ANOVA test allows to find the presumed effect of the parameters of MO and ST on the roughness. In order to apply it the null hypothesis respectively are:

”The multispot overlap has no influence on the superficial roughness”.

”The spot time has no influence on the superficial roughness”.

The data used for ANOVA test are in the table 5.58 and the results in Tab.5.59.

Table 5.58: Data for ANOVA test

MO	32	30	31
Average	0.0309	0.0290	0.0294
Variance	$3.6712 * 10^{-4}$	$1.7148 * 10^{-5}$	$3.9213 * 10^{-5}$
ST	24	25	30
Average	0.0252	0.0297	0.0309
Variance	$3.0517 * 10^{-5}$	$1.8227 * 10^{-5}$	$3.6712 * 10^{-5}$

Table 5.59: ANOVA for column control factor for contour parameters

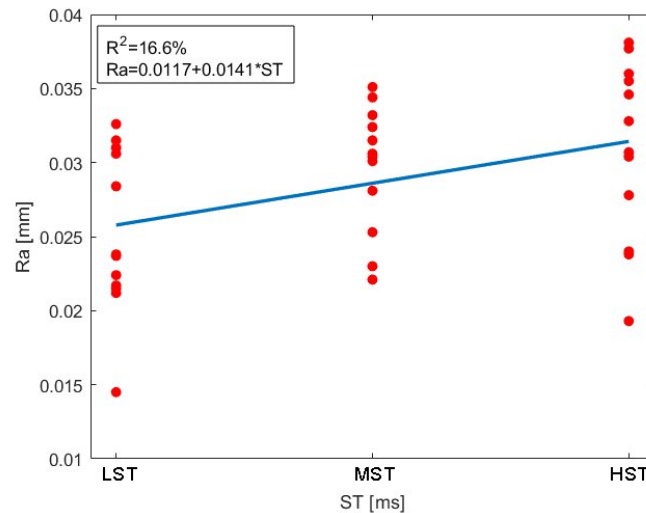
MO				
Variation cause	Degrees of freedom	Variance	Variance ratio	F_{MAX}
Examined factor	2	$1.13 * 10^{-5}$	0.36	3.28
Random errors	33	$3.10 * 10^{-5}$		
Total	35			
ST				
Variation cause	Degrees of freedom	Variance	Variance ratio	F_{MAX}
Examined factor	2	$1.05 * 10^{-4}$	3.70	3.28
Random errors	33	$2.85 * 10^{-5}$		
Total	35			

The ANOVA analysis results show that spot time has an effect on the roughness, indeed nothing is possible to say about the multispot overlap parameter.

In order to represent the experimental data globally, the linear model is initially chosen, described by equation 4.13. For this purpose, the parameters a and t are identified, in particular the independent variable t represents the spot time parameter, while the dependent variable x represents the roughness measurement Ra. Equation 4.13, in this case, can therefore be expressed as 5.3:

$$x = 0.0117 + 0.0141 * ST \quad (5.3)$$

The image 5.20 shows R^2 is 16.6%, the linear model does not describe the experimental data efficiently.

**Figure 5.20:** Linear regression

The residual plot 5.21 shows a grouping of the data into negative values with positive peaks, which further demonstrates that the linear model is not suitable for describing the distribution of data.

It is not possible to find a model that fits the data better, as the roughness values are dispersed.

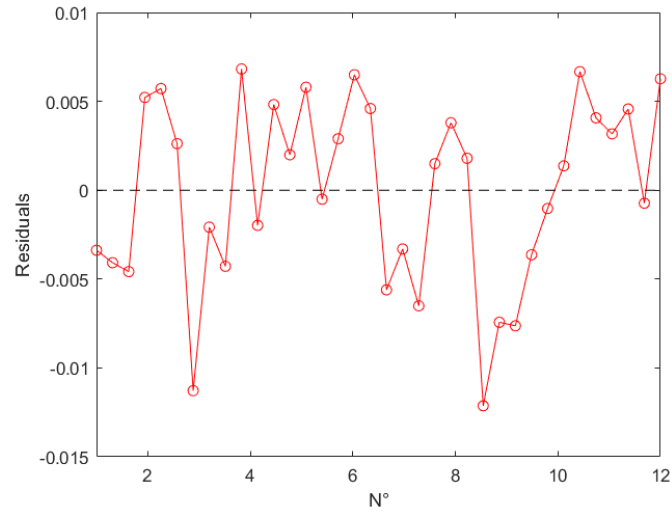


Figure 5.21: Residual from Linear regression model versus survey

In conclusion the mean roughness profile of the specimen 24, 25 and 30 are shown in the figure 5.22, in order to choose the best value of spot time. Therefore there is no one roughness profile better than another one.

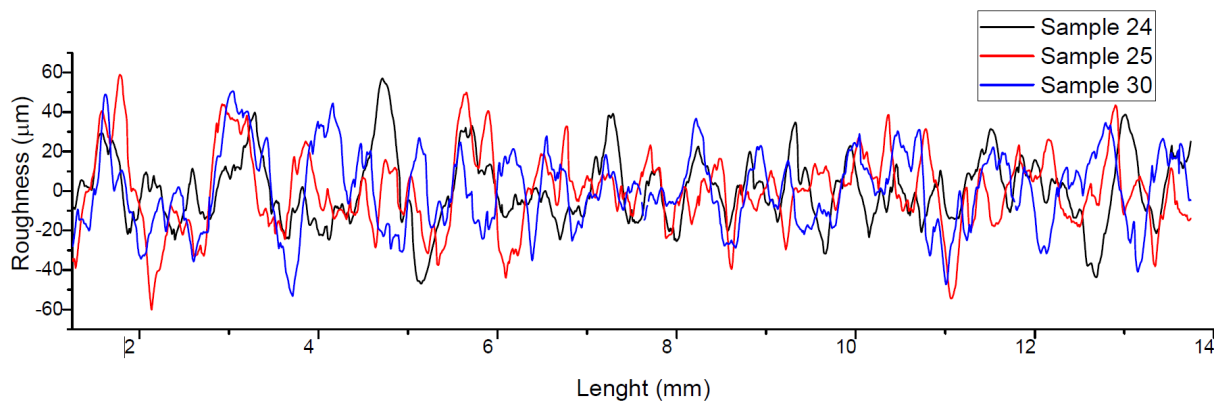


Figure 5.22: Mean roughness profile of the sample 24, 25 and 30.

Chapter 6

Results

6.1 Powder characterization

The SEM analysis by BSD detector allow to prove the real chemical composition compared to the one provided by powder company. The BSD electrons are those ones that have undergone few collisions with the material atoms, the numbers of electrons depend on the atomic number of the detect material. As the BDS electrons arisen from the larger part of the volume interaction detailed information about the morphology are detect. However, the resolution is lower compared to the second electrons one. The BSD analysis on six different points allows to calculate an average chemical composition. The results are shown in the table 6.1.

Table 6.1: Average chemical composition of the Ti-6242 powder.

Element symbol	Atomic concentration [%]	Weight concentration [%]
Ti	85.12	85.53
Al	10.43	5.92
Zr	2.07	3.99
Sn	1.04	2.27
Mo	0.90	2.03
Si	0.44	0.26

As reported in the table above there is no contamination of interstitial atoms. The figure 6.1 displays the powder morphology with different magnification (a) 320X, (b) 760X and (c) 1000X . It is possible to see, especially in the highest magnification image the presence of aggregates, that could decrease the powder flowability.

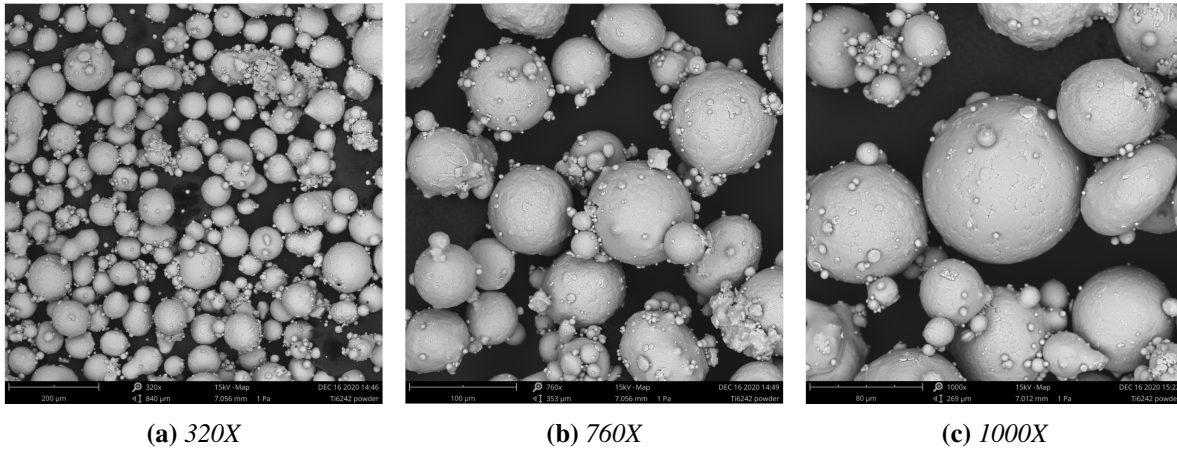


Figure 6.1: *FOV: 838 (a) 353 (b), 269 (c) μm , Mode: 15kV - Map, Detector: BSD Full*

The line scan mode allows to identify the chemical composition across a chosen line, as done in the figure 6.2a. This mode shows that a lack of titanium in a certain point leads to a micron pores, as shown by the purple line (titanium content) in the figure 6.2b.

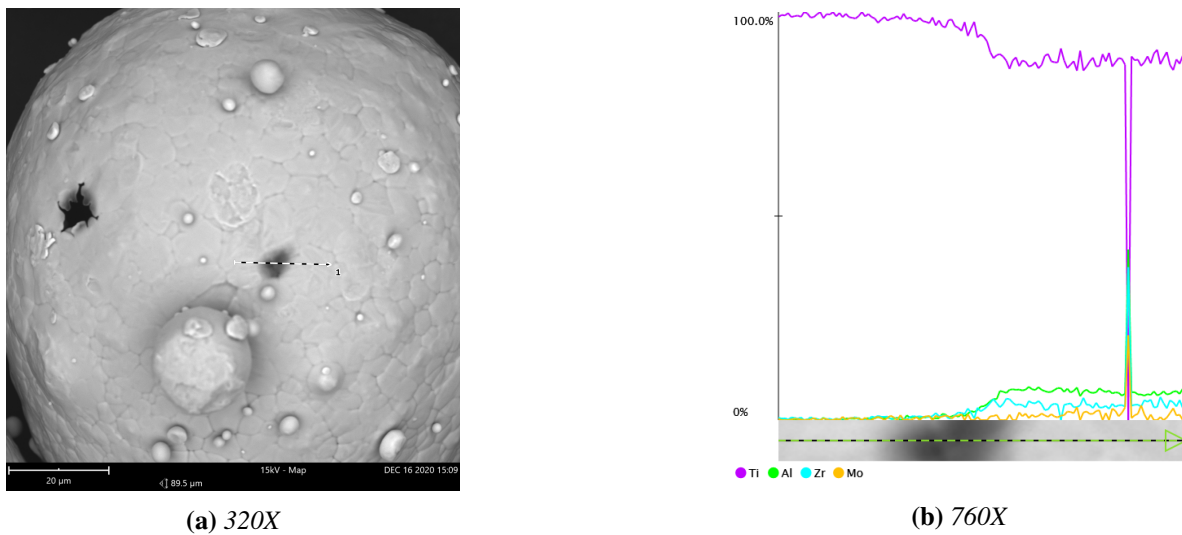


Figure 6.2: *(a) FOV: 89.5 μm , Mode: 15kV - Map, Detector: BSD Full, (b) combined line scan*

6.2 Density and porosity

The results of density analysis are contained in the Tab.A.1 in the Appendix. The plot in Fig.6.5 displays the density and porosity trend.

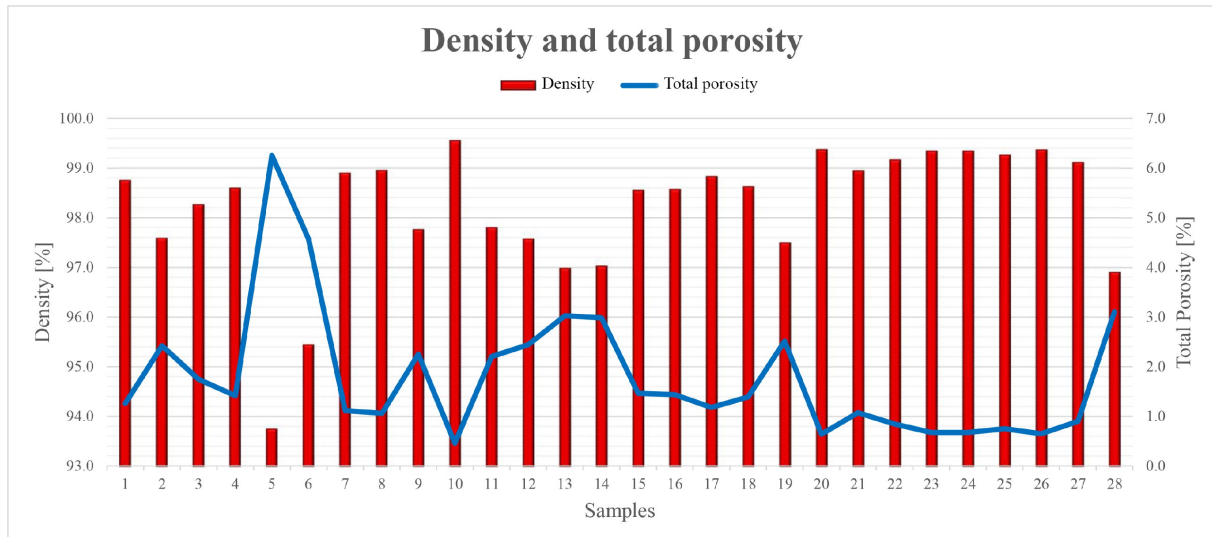


Figure 6.3: *Density and porosity results*

As shown in the plot the lowest density value is 93.7% (for the sample 5) and highest is 99.5% (for the sample 10); the maximum porosity value reached is the same as that found for the samples produced by SLM with the optimized parameters [1] but lower than the value reached by the samples with the addition of boron [18] [19].

The results of the image analysis 6.2 confirm the assumption that the worst samples are 5 and 6 while the best sample appears to be sample number 27 (highlighted in yellow). The image analysis suggests that the use of the contour mode effectively allows to close the open porosities, with the same hatch parameters (of sample 1). However, the image analysis is misleading because it is based on the percentage of porosity found on a section, on an average of 12 images per samples.

In order to verify the Archimede results, the porosity and distribution of pores of specimens 5 and 10 were analyzed by a computed tomography machine. The tomography image 6.4 (a) shows that the sample 5 has high open porosities due to some cracks originated from the contour. On the other hand the sample 10, scanned in 6.4 (b), is very dense, it has some millimeter porosities only on the surface.

Therefore from a first reading of the data analysis, the hatch parameters of the sample 10 and the contour parameters of the sample 27 are optimal for high density and, consequently, low porosity.

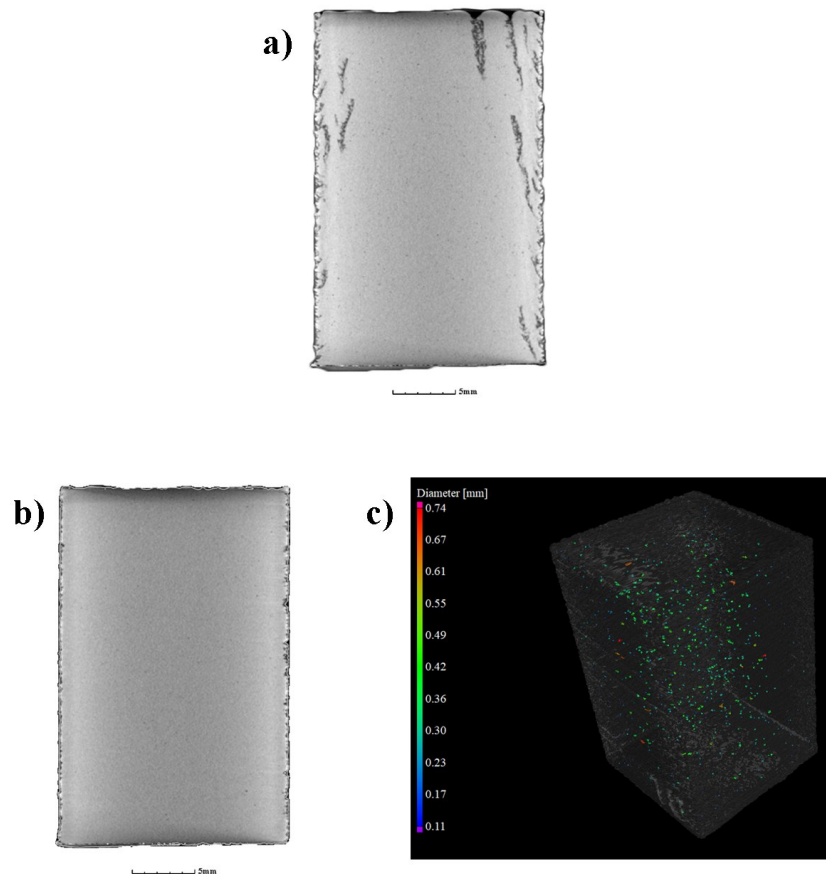


Figure 6.4: The tomography images of the sample 5 (a) and of the sample 10 (b), while the picture (c) is the result scanning of the latter one.

However, by comparing the density between the sample 10 and its replica, a variation of 0.9% is observed. In the light of this, the second sample chosen (in descending order of relative density), is the sample 26, which is a replica of sample 8. The samples differ by 0.3% in relative density, so they can actually be considered replicas. The sample 31 has the highest density (and the lowest open porosity) among the samples with contour mode.

In conclusion, the best parameters in order to maximize the density are the hatch ones of the sample 8 and the contour ones of the sample 31.

Table 6.2: Results porosity percentage from image analysis

Image	Sample 1	Sample 6	Sample 10	Sample 13	Sample 19	Sample 27	Sample 36
1	1.258	0.316	0.405	0.505	0.414	0.03	0.389
2	1.226	0.313	0.194	0.523	0.996	0.015	0.777
3	0.457	0.394	0.253	0.87	0.241	0.015	1.143
4	0.104	0.738	1.905	0.308	0.629	0.035	0.277
5	1.258	0.801	1.178	0.548	0.623	0.277	1.437
6	0.865	0.686	0.779	0.44	0.388	0.504	0.731
7	0.852	0.577	0.588	0.398	0.372	0.631	0.522
8	0.592	1.075	0.148	0.403	0.567	0.233	0.398
9	0.721	1.245	0.724	0.684	0.115	0.508	0.499
10	0.425	0.717	0.61	0.203	1.368	0.005	0.244
11	0.195	0.799	0.694	1.558	0.419	0.21	0.658
12	0.459	0.871	0.209	1.851	1.274	0.416	0.678
Average	0.701	0.711	0.641	0.691	0.617	0.240	0.646

6.3 Parameters effects

The table 6.3 summarizes the results of the previous chapter. As seen the data are too scattered, so the distribution does not follow the normal one. In order to verify that the found parameters are optimal for Ti-6242 it is necessary to produce more replicas, i.e more samples with the same set of parameters. Additional data revealed allow a normal distribution and better efficiency in using linear regression.

The most rigorous hypothesis test is the ANOVA, which results lead to define which parameters can have an effect on the roughness values. In this case the beam speed, the beam diameter, the focus offset and the spot time seem to have an effect on the roughness. As mentioned in the previous paragraph, it is not possible to directly set beam diameter in the EBM machine because it depends on the focus offset and on the beam current so linear regression model cannot find an equation that linearly links the diameter to the R_a . In addition it was not possible to obtain a model that would effectively link the beam speed and spot time parameters to the roughness due to the high dispersion of the data. A low R^2 value may relate to simultaneous effects which will more in-depth investigated in future research.

The focus offset is the only parameter whose effect is effectively described by the linear model, with an R^2 greater than 50%.

The equation 5.2 obtained by regression model shows that the roughness decreases as the focus offset value increases. In order to confirm this statement it is necessary to produce samples with intermediate focus offset values and to ensure that the roughness values follow the trend resulting from the regression model.

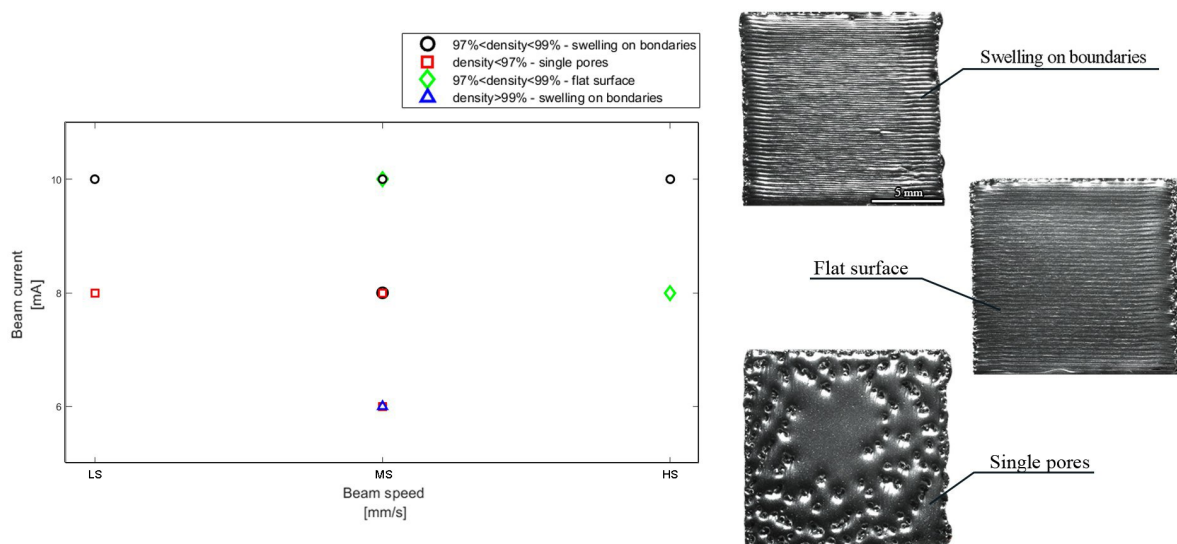
Table 6.3: Results statistic analysis

Parameter	Experimental χ^2	Test average hypothesis	Test variance hypothesis	ANOVA
Beam speed	Outside	Outside	Outside	$F_{calc} > F_U$
Beam diameter	Outside	Outside	Inside	$F_{calc} > F_U$
Beam current	Outside	Inside	Outside	$F_{calc} < F_U$
Focus offset	Inner	Outside	Inside	$F_{calc} > F_U$
Line offset	Outside	Inside	Outside	$F_{calc} < F_U$
Multispot overlap	Inside	Outside	Inside	$F_{calc} < F_U$
Spot time	Inside	Outside	Inside	$F_{calc} > F_U$

The purpose of the graph in figure 6.5 is to identify the window of optimal parameters to obtain samples with high density, e.g greater than 97%, with the best finishing of the top.

Due to the low number of replicates for each sample set there are not enough data to sketch out a statistical analysis on the parameters that would influence the top finish. However, the data of top roughness are contained in the table A.2 for further information.

For the set of parameters chosen, it is possible to divide the upper surfaces into three categories: single pores, swelling on boundaries and the flat surface, represented on the right of the graph in figure.

**Figure 6.5:** Density and porosity results

As the beam speed increases from the lower level to the highest one as the top surface changes from a single pore surface (with density less than 97%) to a flat surface (characterized by higher density), as shown above the graph on the left.

In order to test the chosen parameters a second job was product, including not only specimens but also a final component, i.e an impeller. The Archimede analysis records a geometric density of 99.93%.

Furthermore, the tomography analysis on the impeller confirms the Archimede results. The figure 6.6 (a)

analyzes the section characterized by the biggest detected porosity (identified as "Defect") with a size of 0.92 mm. The porosity distribution is described by cumulative histogram, shown in 6.6 (b), where the majority of the detected pores has a size less than 0.3 mm. The last image (6.6 (c)) allows to verify the dimensional accuracy compared to the CAD file; the "hot" colors identify a material surplus while the "cold" ones a material deficiency. The impeller is almost green that corresponds to a dimensional accuracy of ± 0.20 mm while the crown shows a small orange areas. The number "2" was added during the production, so it was not included in CAD project.

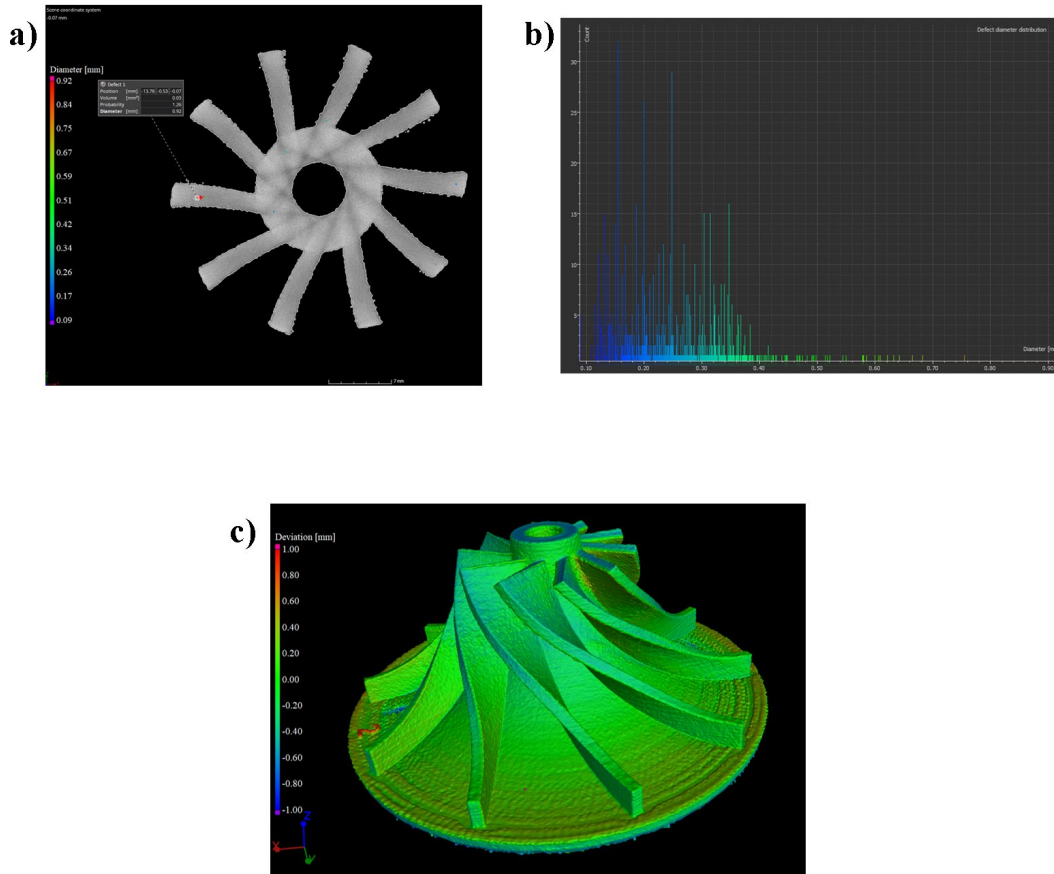


Figure 6.6: Impeller scanning by tomography analysis: (a) section with the biggest pore, (b) cumulative histogram of porosity distribution, (c) dimensional accuracy.

This result allows to conclude the parameters window identified (summarized in the table 6.4) are optimal for the production of a dense Ti-6242 components.

Table 6.4: Optimized Parameters

	FO [mA]	Beam Speed [mm/s]	LO[mm]	Ref Current [mA]
Hatch	MFO	HS	MLO	IBC
Contour				
Spots	Spot time [ms]	Multispot overlap	Max current [mA]	FO [mA]
LSP	HST	HMO	HMC	CFO

Chapter 7

Conclusion

Test results confirm that EBM technique can be successfully applied to process Ti-6242 alloy components, without any issues related to oxide formation and contamination.

The statistical and inferential analysis show that the variation on the beam speed, beam diameter, focus offset and spot time cannot be denied has an effect on the roughness. However, the scattered data do not allow to find a relation that could link these parameters to the roughness; in the case of focus offset, the linear model effectively describes effects on roughness but it is necessary to produce samples with intermediate focus offset value to verify that the found trend follows the detected roughness data.

On top finishing side it is possible to divide the top surface into three classes: single pores, swelling on boundaries and the flat surface (desired one). The highest quality specimens with relative density in excess of 99% and flat surfaces are obtained with the highest beam speed.

The results of the Archimede analysis prove that the optimal parameters window are those used for the sample 8 (hatch parameters) and sample 31 (contour parameters).

An impeller was produced in a second job by setting the found parameters. The Archimede density results reached very high value, even though the surface roughness of the impeller would be checked. The tomography scanning confirmed a density of 99.93%, with a dimensional accuracy of ± 0.2 mm.

This thesis work is only the beginning of a research aimed for identifying the optimal parameters to produce final components, taking into consideration amendments required by the design and field of application. Furthermore, the microstructural response has not been studied but it is important to characterize the mechanical properties and the performance of the component in operation consequently.

Chapter 8

List of symbols, tables and figures

• EBM	Electron Beam Melting;
• SLM	Selective Laser Melting;
• Ti-6242	Ti-6Al-2Sn-4Zr-2Mo alloy;
• Ti-64	Ti-6Al-4V alloy;
• α-case	oxide layer;
• HCP	Hexagonal Close Packed crystal structure;
• BCC	Body Centered Cubic crystal structure;
• α	HCP phase of Ti, stable at low temperature;
• β	BCC phase of Ti, stable at high temperature;
• T_{β}	transition temperature from α to β
• α_2	Ti ₃ Al intermetallic;
• γ	TiAl phase;
• TMP	thermomechanical processing;
• TiO₂	oxide layer;
• AM	Additive Manufacturing;
• CAD	3D Computer Aided Design;
• PBF	Powder Bed Fusion;
• FO	Focus Offset;
• LO	Line Offset;
• MO	Multispot Overlap;
• ST	Spot Time;

• SF	Speed Function index;
• DOE	Design Of Experiment;
• SEM	Scanning electron microscopy;
• BSD	Back Scattered Detection;
• f_{a_j}	absolute frequency of the j-th class;
• f_{e_j}	relative frequency of the j-th class;
• ρ_f	density frequency;
• IQR	interquartile range;
• NPP	Normal Probability Plot;
• ANOVA	ANalysis Of VAriance;
• χ^2	random variable;
• FOV	Field Of View;

List of Tables

3.1	Main process parameters for samples without contour: Focus offset(FO), beam speed, speed function index (SF), line offset, beam current.	19
3.2	Main process parameters for samples with contour	19
3.3	Technical data Arcam EBM A2X.	20
3.4	Average weight from Archimede density analysis.	21
4.1	Data organization [23]	28
4.2	ANOVA scheme for one factor	30
5.1	Experimental roughness data in millimeters for BS parameter analysis.	32
5.2	Comparison with mean value and standard deviation for BS data.	33
5.3	BS data for the detection of possible measurement errors and limits of acceptability experimental values.	33
5.4	BS data for the detection of possible measurement errors and limits of acceptability experimental values.	34
5.5	BS data for Evaluation of Experimental χ^2	35
5.6	BS data for Test hypothesis on columns.	35
5.7	Boundaries for test hypothesis on columns of BS data.	36
5.8	Variance of columns for BS samples.	36
5.9	Boundaries for test hypothesis on columns variance for BS samples.	36
5.10	BS data for ANOVA test.	36
5.11	ANOVA for column control factor, for BS specimens.	36
5.12	Experimental roughness data in millimeters for diameter parameter analysis.	39
5.13	Comparison with mean value and standard deviation for diameter parameter analysis.	39
5.14	Data of diameter analysis for the detection of possible measurement errors and limits of acceptability experimental values	39
5.15	Data of diameter effect analysis for the detection of possible measurement errors and limits of acceptability experimental values	40
5.16	Data for Evaluation of Experimental χ^2	41
5.17	Data for Test hypothesis on columns	42
5.18	Boundary for test hypothesis on columns	42
5.19	Variance of columns	43
5.20	Boundary for test hypothesis on columns variance	43
5.21	Data for ANOVA test	43

5.22	ANOVA for column control factor	43
5.23	Experimental data of samples 1-6-7 in millimeters	44
5.24	Comparison with mean value and standard deviation	44
5.25	Data for the detection of possible measurement errors and limits of acceptability experimental values	44
5.26	Data for the detection of possible measurement errors and limits of acceptability experimental values	45
5.27	Data for Evaluation of Experimental χ^2	46
5.28	Data for Test hypothesis on columns	47
5.29	Boundary for test hypothesis on columns	47
5.30	Variance of columns	47
5.31	Boundary for test hypothesis on columns variance	48
5.32	Data for ANOVA test	48
5.33	ANOVA for column control factor	48
5.34	Experimental data in millimeters	49
5.35	Comparison with mean value and standard deviation	49
5.36	Data for the detection of possible measurement errors and limits of acceptability experimental values	49
5.37	Data for the detection of possible measurement errors and limits of acceptability experimental values	50
5.38	Data for Evaluation of Experimental χ^2	51
5.39	Data for Test hypothesis on columns	52
5.40	Boundary for test hypothesis on columns	52
5.41	Variance of columns	53
5.42	Boundary for test hypothesis on columns variance	53
5.43	Data for ANOVA test	53
5.44	ANOVA for column control factor	53
5.45	Experimental data in millimeters	55
5.46	Comparison with mean value and standard deviation	55
5.47	Data for the detection of possible measurement errors and limits of acceptability experimental values	55
5.48	Data for the detection of possible measurement errors and limits of acceptability experimental values	56
5.49	Data for Evaluation of Experimental χ^2	57
5.50	Data for Test hypothesis on columns	58
5.51	Boundary for test hypothesis on columns	58
5.52	Variance of columns	59
5.53	Boundary for test hypothesis on columns variance	59
5.54	Data for ANOVA test	59
5.55	ANOVA for column control factor	59
5.56	Experimental data ST in mm.	60
5.57	Experimental data MO in mm.	60
5.58	Data for ANOVA test	60

5.59	ANOVA for column control factor for contour parameters	61
6.1	Average chemical composition of the Ti-6242 powder.	63
6.2	Results porosity percentage from image analysis	67
6.3	Results statistic analysis	68
6.4	Optimized Parameters	69
A.1	Results of density analysis	80

List of Figures

2.1	Crystal structure of hcp α and bcc β [2]	2
2.2	Diffusivity of elements in Ti. Note that some elements such as Mo and Sn, Zr and Nb (not shown here) are slow diffusers in Ti. [4]	3
2.3	On the left there is the thermodynamic Ti-Al diagram, on the right a schematic graph to show the compositional difference between α' and α'' . Note that α' forms when the β stabilizers are in low concentration. β_c in the figure stands for the critical concentration of β stabilizers to fully retain β phase at the condition of quenching. β_s stands for the concentration that is required to fully stabilize the β phase at room temperature. M_s and M_f mean the start and finish of the martensite phase transformation.[5]	4
2.4	Classification of terminal titanium alloys.[3]	4
2.5	Titanium alloys application. [7]	5
2.6	Microstructural evolution of pure titanium from $T_{melting}$ to below $T_{\beta-trasus}$ [6].	6
2.7	Widmanstätten microstructure of Ti-64 [6].	6
2.8	(a) Bimodal microstructure and (b) equiaxed microstructure of Ti-64 after TMP process [6].	7
2.9	Schematic of an EBM apparatus. [11]	9
2.10	Differences between EBM and SLM.[13]	11
2.11	Scanning strategy in EBM process: unidirectional raster (a), multi-directional raster (b), zigzag (with offset of the contour (d) and spiatl scanning (e)).	12
2.12	Jump mode (a), sub-division mode (b), split mode (c).	13
2.13	Table of EBM parameters.	14
2.14	SEM image of EBM specimen.[18]	14
2.15	Table of SLM parameters [1].	15
2.16	Profile showing the evolution of surface roughness with scanning speeds [1].	15
2.17	Polished cross-section micrographs of SLMed-Ti-6242 at various scanning speeds of 600–1200 mm/s [1].	16
4.1	Difference between real and nominal shape [24]	23
4.2	Typical profile graph [24]	23
4.3	Average parameters R_a and R_q [24]	24
4.4	Peak parameters R_z [24].	24
4.5	Vertical box	26
5.1	Boxplot	33

5.2	Histogram of relative frequency for BS parameter.	34
5.3	NPP for the BS parameter.	35
5.4	Linear regression for BS samples.	37
5.5	Residual from Linear regression (BS) model versus survey	38
5.6	Boxplot of diameter's effect analysis.	40
5.7	Histogram of relative frequency for diameter effect analysis.	41
5.8	NPP	42
5.9	Boxplot	45
5.10	Histogram of relative frequency	46
5.11	NPP	47
5.12	Boxplot	50
5.13	Histogram of relative frequency	51
5.14	NPP	52
5.15	Linear regression	54
5.16	Residual from Linear regression model versus survey	54
5.17	Boxplot	56
5.18	Histogram of relative frequency	57
5.19	NPP	58
5.20	Linear regression	61
5.21	Residual from Linear regression model versus survey	62
5.22	Mean roughness profile of the sample 24, 25 and 30.	62
6.1	FOV: 838 (a) 353 (b), 269 (c) μm , Mode: 15kV - Map, Detector: BSD Full	64
6.2	(a) FOV: 89.5 μm , Mode: 15kV - Map, Detector: BSD Full, (b) combined line scan	64
6.3	Density and porosity results	65
6.4	The tomography images of the sample 5 (a) and of the sample 10 (b), while the picture (c) is the result scanning of the latter one.	66
6.5	Density and porosity results	68
6.6	Impeller scanning by tomography analysis: (a) section with the biggest pore, (b) cumulative histogram of porosity distribution, (c) dimensional accuracy.	69

Bibliography

- [1] Haiyang Fan and Shoufeng Yang. Effects of direct aging on near-alpha ti-6al-2sn-4zr-2mo (ti-6242) titanium alloy fabricated by selective laser melting (slm). *Materials Science and Engineering: A*, page 139533, 2020.
- [2] Christoph Leyens and Manfred Peters. *Titanium and titanium alloys: fundamentals and applications*. John Wiley & Sons, 2003.
- [3] FH Froes. *Titanium: physical metallurgy, processing, and applications*. ASM international, 2015.
- [4] Ming Yan. Microstructural characterization of as-sintered titanium and titanium alloys. In *Titanium powder metallurgy*, pages 555–578. Elsevier, 2015.
- [5] Alessandro Morri. Trattamenti termici delle leghe di titanio $\alpha+\beta$, correlazioni fra microstruttura e comportamento meccanico. *la metallurgia italiana*, 2008.
- [6] Raghuveer Gaddam. *Microstructure and mechanical properties of Ti-6Al-2Sn-4Zr-2Mo and Ti-6Al-4V: influence of H, O and B*. PhD thesis, Luleå tekniska universitet, 2013.
- [7] M.Rosso. LEGHE DI TITANIO, MAGNESIO E ZINCO. Technical Report Lezione 16, Politecnico di TorinoTorino, Italy, 2018.
- [8] A Chamanfar, T Pasang, A Ventura, and WZ Misiolek. Mechanical properties and microstructure of laser welded ti-6al-2sn-4zr-2mo (ti6242) titanium alloy. *Materials Science and Engineering: A*, 663:213–224, 2016.
- [9] SL Semiatin. *Metallurgical and Materials Transactions A*, pages 1–33, 2020.
- [10] Raghuveer Gaddam, Birhan Sefer, Robert Pederson, and Marta-Lena Antti. Study of alpha-case depth in ti-6al-2sn-4zr-2mo and ti-6al-4v. In *IOP Conference Series: Materials Science and Engineering*, volume 48, page 012002. IOP Publishing, 2013.
- [11] B. Stucker I. Gibson, D. W. Rosen. *Additive manufacturing technologies: Rapid prototyping to direct digital manufacturing*. Springer, 2010.
- [12] Irene Nardone. *Caratterizzazione e ottimizzazione dei trattamenti termici sulla lega di Ti-6Al-4V prodotto per Electron Beam Melting (EBM): Characterization and optimization of heat treatments of Ti-6Al-4V alloy fabricated by Electron Beam Melting (EBM)*. PhD thesis, Politecnico di Torino, 2019.

- [13] Filippo Montecchio. Progettazione e sviluppo di dissipatori di calore mediante tecnologia di "additive manufacturing". 2018.
- [14] U Prisco, A Astarita, A El Hassanin, and S Franchitti. Influence of processing parameters on microstructure and roughness of electron beam melted ti-6al-4v titanium alloy. *Materials and Manufacturing Processes*, 34(15):1753–1760, 2019.
- [15] Sneha P Narra, Ross Cunningham, Jack Beuth, and Anthony D Rollett. Location specific solidification microstructure control in electron beam melting of ti-6al-4v. *Additive Manufacturing*, 19:160–166, 2018.
- [16] Shunyu Liu and Yung C Shin. Additive manufacturing of ti6al4v alloy: A review. *Materials & Design*, 164:107552, 2019.
- [17] YS Lee, Michael M Kirka, Ralph Barton Dinwiddie, Narendran Raghavan, J Turner, Ryan R Dehoff, and Sudarsanam Suresh Babu. Role of scan strategies on thermal gradient and solidification rate in electron beam powder bed fusion. *Additive Manufacturing*, 22:516–527, 2018.
- [18] Tadashi Fujieda, Yujie Cui, Kenta Aoyagi, Yuichiro Koizumi, and Akihiko Chiba. Electron beam melting of boron-modified ti-6al-2sn-4zr-2mo-0.1 si alloy with superior tensile strength and oxidation resistance at elevated temperatures. *Materialia*, 4:367–372, 2018.
- [19] Yujie Cui, Kenta Aoyagi, Yuichiro Koizumi, Tadashi Fujieda, and Akihiko Chiba. Enhanced oxidation resistance of a titanium-based alloy by the addition of boron and the application of electron beam melting. *Additive Manufacturing*, 31:100971, 2020.
- [20] Manuela Galati, Giovanni Rizza, Silvio Defanti, and Lucia Denti. Surface roughness prediction model for electron beam melting (ebm) processing ti6al4v. *Precision Engineering*, 69:19–28, 2021.
- [22] Tomasz Kurzynowski, Marcin Madeja, Robert Dzedzic, and Karol Kobiela. The effect of ebm process parameters on porosity and microstructure of ti-5al-5mo-5v-1cr-1fe alloy. *Scanning*, 2019, 2019.
- [23] Giulio Barbato, Gianfranco Genta, and Alessandro Germak. *Misurare per Decidere. Misure e Statistica di Base*. Società Editrice Esculapio, 2020.
- [24] David J Whitehouse. *Handbook of surface and nanometrology*. CRC press, 2010.
- [25] Tadashi Fujieda, Yujie Cui, Kenta Aoyagi, Yuichiro Koizumi, and Akihiko Chiba. Electron beam melting of boron-modified ti-6al-2sn-4zr-2mo-0.1 si alloy with superior tensile strength and oxidation resistance at elevated temperatures. *Materialia*, 4:367–372, 2018.
- [26] Sneha P Narra, Ross Cunningham, Jack Beuth, and Anthony D Rollett. Location specific solidification microstructure control in electron beam melting of ti-6al-4v. *Additive Manufacturing*, 19:160–166, 2018.
- [27] Manuela Galati and Paolo Minetola. Analysis of density, roughness, and accuracy of the atomic diffusion additive manufacturing (adam) process for metal parts. *Materials*, 12(24):4122, 2019.

Appendix A

Appendix

A.1 Density results

Table A.1: *Results of density analysis*

#	Open porosity (%)	Closed Porosity (%)	Relative Archimedes density (%)	Relative Geometrical density (%)	Error Geometrical density	Error porosity
1	0.3	1.0	99.0	98.7	0.012	0.355
2	0.8	1.6	98.4	97.6	0.012	0.351
3	0.9	0.9	99.1	98.3	0.012	0.353
4	0.7	0.7	99.3	98.6	0.012	0.351
5	2.6	3.7	96.2	93.7	0.012	0.346
6	1.0	3.5	96.4	95.4	0.012	0.347
7	0.6	0.5	99.5	98.9	0.013	0.360
8	0.4	0.6	99.4	98.9	0.012	0.347
9	0.6	1.6	98.4	97.9	0.0122	0.354
10	0.1	0.3	99.7	99.5	0.012	0.358
11	1.0	1.2	98.8	97.8	0.012	0.360
12	0.9	1.5	98.5	97.6	0.012	0.352
13	1.4	1.7	98.3	97.0	0.013	0.362
14	0.8	2.2	97.8	97.0	0.013	0.363
19	0.7	0.8	99.2	98.5	0.013	0.360
20	0.6	0.8	99.2	98.6	0.013	0.363
21	0.8	0.4	99.6	98.8	0.013	0.360
22	0.5	0.9	99.1	98.6	0.013	0.359
23	0.9	1.6	98.4	97.5	0.013	0.363
24	0.3	0.4	99.6	99.4	0.012	0.347
25	0.5	0.6	99.4	98.9	0.012	0.347
26	0.3	0.5	99.5	99.2	0.012	0.347
27	0.3	0.4	99.6	99.3	0.012	0.346
29	0.2	0.5	99.5	99.3	0.012	0.347
30	0.3	0.4	99.6	99.3	0.012	0.348
31	0.3	0.4	99.6	99.4	0.012	0.348
32	0.5	0.4	99.6	99.1	0.012	0.347
36	1.1	2.0	98.0	96.9	0.013	0.357

A.2 Top surface roughness

Samples	R_a		
1 and 19	TOP	sx	9.802
		center	5.974
		dx	7.77
	1	sx	41.824
		center	30.975
		dx	40.903
	2	sx	38.164
		center	27.377
		dx	32.826
	3	sx	19.833
		center	26.851
		dx	26.016
	4	sx	45.931
		center	66.109
		dx	64.745
2	TOP	sx	8.929
		center	8.29
		dx	8.562
	1	sx	27.484
		center	30.848
		dx	32.23
	2	sx	34.338
		center	42.038
		dx	38.067
	3	sx	34.022
		center	36.272
		dx	31.849
	4	sx	42.624
		center	34.515
		dx	37.924

Samples	R_a		
3	TOP	sx	8.693
		center	8.218
		dx	9.456
	1	sx	37.671
		center	36.714
		dx	42.958
	2	sx	29.404
		center	39.917
		dx	39.869
	3	sx	37.025
		center	37.089
		dx	36.235
	4	sx	35.932
		center	41.4745
		dx	35.577
4	TOP	sx	15.562
		center	12.964
		dx	15.193
	1	sx	22.966
		center	27.198
		dx	41.802
	2	sx	29.919
		center	36.449
		dx	39.898
	3	sx	32.683
		center	30.041
		dx	27.361
	4	sx	32.293
		center	41.385
		dx	45.187

Samples	R_a		
5	TOP	sx	50.54
		center	16.46
		dx	29.234
	1	sx	42.68
		center	36.266
		dx	40.32
	2	sx	40.081
		center	38.024
		dx	41.62
	3	sx	36.438
		center	36.915
		dx	46.287
	4	sx	36.18
		center	45.217
		dx	36.364
6	TOP	sx	31.652
		center	11.102
		dx	24.567
	1	sx	35.624
		center	20.121
		dx	33.678
	2	sx	37.263
		center	43.432
		dx	56.206
	3	sx	31.975
		center	37.173
		dx	36.465
	4	sx	43.098
		center	37.335
		dx	41.135
8 and 26	TOP	sx	5.911
		center	6.722
		dx	6.378
	1	sx	23.121
		center	34.897
		dx	20.042
	2	sx	14.867
		center	29.395
		dx	30.964
	3	sx	26.0763
		center	23.209
		dx	23.209
	4	sx	27.18
		center	26.319
		dx	25.402

Samples	R_a		
9	TOP	sx	9.576
		center	8.367
		dx	9.016
	1	sx	34.5
		center	31.842
		dx	29.478
	2	sx	27.568
		center	35.135
		dx	28.48
	3	sx	27.136
		center	35.712
		dx	26.376
	4	sx	34.865
		center	37.115
		dx	42.329
10 and 22	TOP	sx	22.605
		center	21.097
		dx	19.272
	1	sx	36.347
		center	34.27
		dx	41.969
	2	sx	39.747
		center	33.785
		dx	37.264
	3	sx	25.759
		center	26.514
		dx	38.98
	4	sx	30.57
		center	35.857
		dx	37.42
11 and 23	TOP	sx	3.866
		center	2.938
		dx	2.81
	1	sx	36.006
		center	36.171
		dx	39.649
	2	sx	42.11
		center	47.71
		dx	43.224
	3	sx	39.222
		center	32.768
		dx	36.119
	4	sx	42.759
		center	39.051
		dx	38.015

Samples	R_a		
12	TOP	sx	8.575
		center	8.249
		dx	7.331
	1	sx	36.184
		center	35.67
		dx	34,763
	2	sx	38.3
		center	38.257
		dx	44.61
	3	sx	39.438
		center	30.58
		dx	32.596
	4	sx	37.232
		center	37.466
		dx	35.377
13 and 36	TOP	sx	2.827
		center	2.717
		dx	3.236
	1	sx	35.055
		center	36.089
		dx	37.348
	2	sx	55.819
		center	56.533
		dx	57.491
	3	sx	51.837
		center	59.077
		dx	60.458
	4	sx	44.321
		center	40.782
		dx	43.218
14 and 20	TOP	sx	4.563
		center	2.944
		dx	3.437
	1	sx	34.515
		center	35.93
		dx	35.939
	2	sx	43.552
		center	38.583
		dx	39.994
	3	sx	44.847
		center	44.359
		dx	50.291
	4	sx	41.966
		center	44.111
		dx	41.133